

Processing and properties of alumina reinforced mullite ceramics

Dissertation

zur Erlangung des akademischen Grades

**Doktoringenieur
(Dr.-Ing.)**

Von M.Sc.Valetine Kubong Atanga

Geb. am 27.08.1976 in Alatening, Kamerun

Genehmigt durch die Fakultät Für Maschinenbau
der Otto-von-Guericke-Universität Magdeburg

Gutachter: Prof. Dr. rer. nat. Michael Scheffler
Prof. Dr.-Ing. habil. Christos G. Aneziris

Promotionskolloquium am 18-09-2013

Ehrenerklärung

„Ich versichere hiermit, dass ich die vorliegende Arbeit ohne unzulässige Hilfe Dritter und ohne Benutzung anderer als der angegebenen Hilfsmittel angefertigt habe. Die Hilfe eines kommerziellen Promotionsberaters habe ich nicht in Anspruch genommen. Dritte haben von mir weder unmittelbar noch mittelbar geldwerte Leistungen für Arbeiten erhalten, die im Zusammenhang mit dem Inhalt der vorgelegten Dissertation stehen. Verwendete fremde und eigene Quellen sind als solche kenntlich gemacht.

Ich habe insbesondere nicht wissentlich:

- Ergebnisse erfunden oder widersprüchliche Ergebnisse verschwiegen,
- statistische Verfahren absichtlich missbraucht, um Daten in ungerechtfertigter Weise zu interpretieren,
- fremde Ergebnisse oder Veröffentlichungen plagiiert,
- fremde Forschungsergebnisse verzerrt wiedergegeben

Mir ist bekannt, dass Verstöße gegen das Urheberrecht Unterlassungs- und Schadensersatzansprüche des Urhebers sowie eine strafrechtliche Ahndung durch die Strafverfolgungsbehörden begründen kann.

Ich erkläre mich damit einverstanden, dass die Dissertation ggf. mit Mitteln der elektronischen Datenverarbeitung auf Plagiate überprüft werden kann.

Die Arbeit wurde bisher weder im Inland noch im Ausland in gleicher oder ähnlicher Form als Dissertation eingereicht und ist als Ganzes auch noch nicht veröffentlicht.“

Magdeburg, 02.07.2013

Declaration of Honor

„I hereby declare that I produced this thesis without prohibited external assistance and that none other than the listed references and tools have been used. I did not make use of any commercial consultant concerning graduation. A third party did not receive any nonmonetary perquisites neither directly nor indirectly for activities which are connected with the contents of the presented thesis.

All sources of information are clearly marked, including my own publications.

In particular I have not consciously:

- Fabricated data or rejected undesired results
- Misused statistical methods with the aim of drawing other conclusions than those warranted by the available data
- Plagiarized data or publications
- Presented the results of other researchers in a distorted way

I do know that violations of copyright may lead to injunction and damage claims of the author and also to prosecution by the law enforcement authorities. I hereby agree that the thesis may need to be reviewed with an electronic data processing for plagiarism.

This work has not yet been submitted as a doctoral thesis in the same or a similar form in Germany or in any other country. It has not yet been published as a whole.”

Magdeburg, 02.07.2013

ACKNOWLEDGEMENT

The author acknowledges with deep appreciation the assistance and support of Prof. Dr. Michael Scheffler (Institute of Materials and Joining Technology, Otto von Guericke University Magdeburg). Special thanks go to the staff of the Institute of Materials and Joining Technology and Institute of Chemistry at Otto von Guericke University, for their dedicated, friendly, and professional help which remains an indelible source of motivation. I would like to acknowledge the support given by Dr. Peter Veit (Institute for Experimental Physics for carrying out TEM investigations), Dr. Janan Al-Karawi (Institute of Fluid Dynamics and Thermodynamics for carrying out thermal conductivity measurements at Otto von Guericke University Magdeburg), Dr. Viola Wilker, Christaine Ohl and Mathias Kappa, Brandenburg Technical University Cottbus, and Dr. Sarama Bhattacharjee, Institute of Minerals and Material Technology, for numerous discussions and encouragement.

DEDICATION

I dedicate this work to the following:

My family and friends, especially to my late dad, Chi Michael Atanga

Abstract

In this work an alumina-core/mullite-shell like composite material was manufactured based on alumina powder and two different types of silica precursors, and their thermo shock behaviour was investigated. In one set of experiments a silica surplus and in a second series of experiments a silica deficit was used. This allowed to compare the differences of the reaction pathways, of the phase amount formed during sintering and of the material properties as a function of their composition and type of silica source.

The microstructure was characterised by means of solid state characterization and porosity analysis, and the flexural strength of the samples as fired at 1600 °C was measured from room temperature to 1000 °C. A glassy phase was identified to influence the mechanical and thermal properties of the material.

From thermophysical data the critical temperature difference for expected failure and the thermal shock resistance to fracture initiation by thermal stresses were computed and compared to experimental data generated by a hard thermo shock from 1200 °C to room temperature. The crack formation and the crack growth behaviour were imaged with microcomputer tomography, and it was found that the sample series with higher porosity may tolerate a higher thermal induced stress level compared to the samples having a lower porosity.

Kurzfassung

Ziel der vorliegenden Arbeit war die Herstellung einer Aluminiumoxid-Kern/Mullit-Schale artigen Verbundkeramik aus α -Aluminiumoxid und zwei unterschiedlichen SiO_2 -Quellen und die Ermittlung ihres Thermoschockverhaltens. Dabei wurden die SiO_2 -Quellen in Bezug zur Mullitzusammensetzung im Überschuss oder im Unterschuss eingesetzt, was einen Vergleich der Reaktionswege und der sich bildenden Phasen sowie der resultierenden Eigenschaften erlaubte.

Die Charakterisierung der Mikrostruktur erfolgte mit Methoden der Festkörpercharakterisierung; die Bruchfestigkeit wurde im Temperaturbereich von Raumtemperatur bis 1000 °C der bei 1600 °C gesinterten Proben ermittelt.

Aus thermophysikalischen Daten wurden die kritische Temperaturdifferenz und der erste Thermoschockparameter R_s berechnet und mit experimentellen Daten, die im Abschreckversuch von 1200 °C auf Raumtemperatur ermittelt wurden, miteinander verglichen. Dabei wurden die Rissbildung und der Rissfortschritt mittels Mikrocomputertomographie über 20 Thermoschockzyklen visualisiert. Es wurde gefunden, dass die Probenserie mit höherer Porosität bei ausreichend hoher mechanischer Festigkeit dem Thermoschock besser widersteht als die Probenserie mit niedrigerer Porosität.

List of Abbreviations and Symbols

Abbreviations

μ -CT	Micro-computer tomography
AAS	Atomic absorption spectrometer
AIP	Aluminium isopropoxide
Al_2O_3	Aluminium oxide
AlO_4	Aluminium tetrahedral
AlO_6	Aluminium octahedral
ANN	Aluminium nitrate nonahydrate
ASAP	Accelerated surface area and porosimetry
CCD	Charge coupled device
CS	Colloidal silica
CS-23	23 mol.-% SiO_2 :77 mol.-% Al_2O_3
CS-40	40 mol.-% SiO_2 :60 mol.-% Al_2O_3
CT3000SG	Alumina
CTAn	Computer tomography analyzer
CTE	Coefficient of thermal expansion
CVD	Chemical vapour deposition
DSC	Differential scanning calorimetry
DTA	Differential thermal analysis
EDX	Energy dispersive x-ray spectroscopy
Exp't	Experiment
FTIR	Fourier transform infrared spectroscopy
He Py	Helium pycnometry
MAM	Mono-functional methacrylamide
MBAM	Difunctional monomers methylene bisacrylamide
Mwt	Molecular weight
NMR	Nuclear magnetic resonance spectroscopy
PTFE	Polytetrafluoroethylene
ROI	Region of interest
RSC	Cristobalite-alumina
RSQ	Quartz-alumina

RSS	Silica-glass-alumina
RT	Room temperature
SEM	Scanning electron microscopy
SSA	Specific surface area
TEM	Transmission electron microscopy
Temp.	Temperature
TEOS	Tetraethyl orthosilicate
TEOS-23	23 mol.-% SiO ₂ :77 mol.-% Al ₂ O ₃
TEOS-77	77 mol.-% SiO ₂ :23 mol.-% Al ₂ O ₃
TGA	Thermogravimetric analysis
TVS	Transient viscous sintering
VOI	Volume of interest
W _{dry}	Dry weight of sample
W _{sat}	Saturated weight of sample
W _{sup}	Suspended weight of sample in liquid
XRD	X-ray diffraction

Symbols

ΔT	Change in temperature or critical temperature difference for expected failure
ε	Dielectric constant
\varnothing	Diameter
σ_o	Threshold stress
ΔL	Change in length
b	Specimen width
C _p	Heat capacity
d	Specimen thickness or diagonal of indentation
dp	Pore diameter
D _{th}	Thermal diffusivity
E	Young's modulus
f	Deflection
F	Force or cumulative density function
hkl	Miller indices
HV	Vickers hardness

i	Specimen number
L	Support span or length
L_0	Length of sample at ambient temperature
m	Weibull modulus
M	Tangent of the straight line of the load deflection beam
n	Total number of specimen or order of reflection
P	Force
P_f	Failure probability
R	Universal gas constant
R_s	Thermal shock resistance of material to fracture initiation by thermal stresses
α	Linear thermal expansion coefficient
γ	Shear rate
η	Viscosity
θ	Angle
λ	Thermal conductivity or wavelength
ρ	Density
ρ_B	Bulk density
ρ_{liq}	Density of immersion liquid
ρ_s	Skeletal density
σ_i	Flexural strength
ν	Poisson's ratio

Table of Contents

1 INTRODUCTION AND OBJECTIVES	1
2 LITERATURE REVIEW	3
2.1 THE ALUMINA-SILICA PHASE DIAGRAM	3
2.2 THE MOLECULAR STRUCTURE OF ALUMINA.....	5
2.3 SILICA AND ITS MOLECULAR STRUCTURE	7
2.4 THE MOLECULAR STRUCTURE OF MULLITE.....	9
2.5 MULLITE SYNTHESIS, PROCESSING AND FORMATION MECHANISMS	11
2.5.1 Solid-state processed mullite.....	12
2.5.2 Fused-mullite (liquid-state-processed mullite)	13
2.5.3 Mullite from chemical routes.....	17
2.5.4 Hydrothermally produced mullite	28
2.5.5 Gel-casting methods for the mullite synthesis	29
2.6 PROPERTIES AND APPLICATIONS OF MULLITE	29
2.7 MULLITE COMPOSITE MATERIALS	35
3 EXPERIMENTAL	39
3.1 STARTING MATERIALS	39
3.2 MATERIAL PROCESSING	42
3.2.1 Mixing of the starting materials.....	42
3.2.2 Rheological characterization of the suspensions.....	43
3.2.3 Shaping of molds and casting of suspensions.....	44
3.2.4 Thermal treatment of green samples	45
3.3 MICROSTRUCTURE AND PROPERTY ANALYSIS	45
3.3.1 XRD, SEM and TEM analysis.....	45
3.3.2 Porosity analysis.....	47
3.3.3 Thermal analysis of as processed samples	48
3.3.4 Specific surface area	49
3.3.5 Thermal analysis of sintered samples	49
3.4 MATERIAL PROPERTIES.....	50
3.4.1 Mechanical characterization	50
3.4.2 Thermal shock characterization	52

4 RESULTS AND DISCUSSION	54
4.1 RHEOLOGICAL BEHAVIOUR, SAMPLE SHAPE AND SHRINKAGE	54
4.1.1 Rheological behaviour	54
4.1.2 Green sample shaping and stability after heat treatment	55
4.2 THERMAL ANALYSIS OF THE AS PROCESSED PARTS	59
4.3 MICROSTRUCTURE AND POROSITY OF SINTERED SAMPLES	61
4.3.1 SEM and XRD analysis	61
4.3.2 Porosity analysis	67
4.3.3 TEM analysis	72
4.4 MATERIAL PROPERTIES.....	76
4.4.1 Mechanical properties.....	76
4.4.2 Thermal properties.....	82
4.5 THERMO-SHOCK BEHAVIOUR.....	85
5 SUMMARY AND OUTLOOK.....	91
WORKS CITED.....	94
APPENDICES	113

List of Figures

FIGURE 2.1: SILICA-ALUMINA BINARY PHASE DIAGRAM EXTRACTED FROM	4
FIGURE 2.2: THERMAL TRANSFORMATION OF ALUMINIUM HYDROXIDES	5
FIGURE 2.3: (LEFT) CORUNDUM STRUCTURE IN ALPHA- Al_2O_3 AND (RIGHT) OCTAHEDRAL COORDINATION OF ALPHA-ALUMINA	6
FIGURE 2.4: CRYSTAL STRUCTURE OF β -CRISTOBALITE (HIGH TEMPERATURE CRYSTALLINE FORM OF SILICA)	9
FIGURE 2.5: PROJECTION OF CRYSTAL STRUCTURE OF MULLITE ALONG THE C-AXIS (001)	10
FIGURE 2.6: REACTION SINTERING MECHANISM: (LEFT) QUARTZ-ALUMINA, (MIDDLE) SILICA-GLASS- ALUMINA AND (RIGHT) CRISTOBALITE-ALUMINA.....	14
FIGURE 2.7: (LEFT) GLASS PHASE REACTIONS: QUARTZ-ALUMINA (BOTTOM), SILICA GLASS-ALUMINA (MIDDLE), CRISTOBALITE-ALUMINA (TOP) AND (RIGHT) DENSIFICATION OF ALUMINA AND SILICA	15
FIGURE 2.8: HYDROLYSIS REACTIONS BETWEEN THE SILICON ALKOXIDE AND WATER WITH AN ACID CATALYST (A), BASE CATALYST (B), AND (C) CROSS LINKING REACTIONS BETWEEN SILANOLS AND ALUMINIUM HYDROXIDE AT THE HYDROPHILIC SURFACE WITH THE FORMATION OF $\equiv Si-O-Al=$ BONDS. OR = ETHOXY OR METHOXY GROUPS	20
FIGURE 2.9: SCHEMATIC MODELS FOR MULLITE STARTING MATERIALS PREPARED BY: (A) SOL MIXING (B) HYDROLYSIS OF ALKOXIDES (C) MIXING OF CLAY MINERALS AND ALUMINA (D) COMPOSITE PARTICLES (E) SPRAY PYROLYSIS (F) CO-PRECIPITATION.....	23
FIGURE 2.10: CONCEPT OF THE COMPOSITE PARTICLES FORMATION AND THE SINTERING MECHANISM OF MULLITE COMPOSITES	25
FIGURE 3.1: PROCESSING SCHEME	43
FIGURE 3.2: TEFLON MOLDS FOR SLIP CASTING OF THE $SiO_2-Al_2O_3$ SOL-GEL SYSTEMS.....	44
FIGURE 3.3: INDENTATION ON A SURFACE OF THE TEOS-23 SAMPLE.....	51
FIGURE 4.1: VARIATION OF VISCOSITY VERSUS SHEAR RATE.....	54
FIGURE 4.2: TEOS-23 GREEN SAMPLES HEAT-TREATED TO 700 °C WITH A HOLDING TIME OF 3 H; DISK (\varnothing : 42 MM, H: 4 MM); BLOCK CYLINDER (L: 30 MM, \varnothing : 20 MM), HOLLOW CYLINDER (L: 20 MM, INNER \varnothing : 10 MM, OUTER \varnothing : 16 MM), RECTANGULAR PLATES (72 MM X 32 MM X 4 MM), RECTANGULAR BARS (72 MM X 4 MM X 3 MM) WHERE \varnothing : DIAMETER, H: THICKNESS, L: LENGTH.....	56
FIGURE 4.3: CS-23 GREEN SAMPLES HEAT-TREATED TO 700 °C WITH A HOLDING TIME OF 3 H; DISK (\varnothing : 42 MM, H: 4 MM), CYLINDER (L: 18 MM, \varnothing : 14 MM)	56

FIGURE 4.4: TEOS-23 CERAMIC PARTS SINTERED AT 1600 °C WITH A HOLDING TIME OF 12 H; DISK (Ø: 40 MM, H: 2 MM); CYLINDER (L: 15 MM, INNER Ø: 8 MM, OUTER Ø: 12 MM), RECTANGULAR PLATES (70 MM X 30 MM X 2 MM)	57
FIGURE 4.5: CS-23 CERAMIC PARTS (1600 °C, 12 H); DISK (Ø: 40 MM, H: 2 MM), CYLINDRICAL BARS (L= 25, H = 5.5 MM), RECTANGULAR BARS (25 MM X 2.5 MM X 2.5 MM)	58
FIGURE 4.6: SHRINKAGE OF GREEN SAMPLES	59
FIGURE 4.7: THERMAL ANALYSIS OF GREEN SAMPLES HEAT TREATED TO 1550 °C IN AIR AT 5 K MIN ⁻¹	60
FIGURE 4.8: TEOS-23 (LEFT) AND CS-23 (RIGHT) SEM IMAGES OF SAMPLES SINTERED FROM 1200 °C TO 1600 °C, AT 5 K MIN ⁻¹ WITH HOLDING TIME OF 12 H AT PEAK TEMPERATURE	62
FIGURE 4.9: TEOS-77 (LEFT) AND CS-40 (RIGHT) SEM IMAGES OF SAMPLES SINTERED FROM 1200 °C TO 1600 °C, AT 5 K MIN ⁻¹ WITH HOLDING TIME OF 12 H AT PEAK TEMPERATURE	63
FIGURE 4.10: XRD PATTERNS OF THE CS-40 SAMPLES SINTERED AT DIFFERENT TEMPERATURES WITH HOLDING TIMES OF 12 H.....	64
FIGURE 4.11: SEMI QUANTITATIVE RIETVELD ANALYSIS OF SAMPLES AFTER SINTERING IN A TEMPERATURE RANGE FROM 1100 °C TO 1600 °C WITH HOLDING TIMES OF 12 H.....	65
FIGURE 4.12: XRD PHASE ANALYSIS OF SAMPLES SINTERED AT DIFFERENT TEMPERATURES WITH HOLDING TIMES OF 3 H AT PEAK TEMPERATURE.....	66
FIGURE 4.13: BULK DENSITY (ρ_B), SKELETAL DENSITY (ρ_S) AND POROSITY OF TEOS-23 AND CS-23 SAMPLES SINTERED IN THE TEMPERATURE RANGE FROM 1200 °C TO 1600 °C FOR 12 H	67
FIGURE 4.14: BULK DENSITY (ρ_B), SKELETAL DENSITY (ρ_S) AND POROSITY OF TEOS-77 AND CS-60 SAMPLES SINTERED IN THE TEMPERATURE RANGE FROM 1200 °C TO 1600 °C WITH A HOLDING TIME AT PEAK TEMPERATURE OF 12 H.....	68
FIGURE 4.15: μ -CT 3D RECONSTRUCTION OF A “VOLUME OF INTEREST” FROM ALUMINA-MULLITE PARTS OF TEOS-23 (LEFT) AND CS-23 (RIGHT) SAMPLES SINTERED AT 1600 °C FOR 12 H.....	70
FIGURE 4.16: TYPICAL INTRUSION AND EXTRUSION CURVES OF THE AS SYNTHESIZED ALUMINA-MULLITE COMPOSITES, SAMPLES ARE SINTERED AT 1600 °C FOR 12 H.....	71
FIGURE 4.17: TEM IMAGES AND MARKS OF EDX SPOT ANALYSIS FROM THE TEOS-23 DERIVED SAMPLE	73

FIGURE 4.18: TEM IMAGE AND MARKS OF EDX SPOT ANALYSIS FOR TEOS-77 DERIVED MULLITE SAMPLE SINTERED AT 1600 °C FOR 12 H HOLDING TIME	75
FIGURE 4.19: TEM IMAGES AND EDX SPOT ANALYSIS OF CS SAMPLES SINTERED AT 1600 °C FOR 12 H HOLDING TIME, (II) EDX-SPECTRUM OF POSITION G WITH HIGH AL MOL.-%	75
FIGURE 4.20: VICKERS-HARDNESS AS A FUNCTION OF SINTERING TEMPERATURE; SAMPLES SINTERED AT 5 K MIN ⁻¹ WITH HOLDING TIMES OF 12 H AT PEAK TEMPERATURE	77
FIGURE 4.21: FLEXURAL STRENGTH OF THE SAMPLES TEOS-23 AND CS-23 AFTER FIRING AT 1600 °C FOR 3H AND FOR 12 H.....	78
FIGURE 4.22: WEIBULL PLOT FOR TEOS-23 AND CS-23 ALUMINA-MULLITE SAMPLES SINTERED AT 1600 °C WITH 12 H HOLDING TIMES	79
FIGURE 4.23: WEIBULL DISTRIBUTION PLOT WITH PROBABILITY OF FAILURE FOR TEOS-23 AND CS-23 SAMPLES SINTERED AT 1600 °C FOR 12 H HOLDING TIMES.....	80
FIGURE 4.24: FLEXURAL STRENGTH AT 25 °C, 500 °C AND 1000 °C OF TEOS-23 AND CS-23 SAMPLES SINTERED AT A TEMPERATURE OF 1600 °C FOR 12 H.....	81
FIGURE 4.25: THERMAL BEHAVIOUR OF HEAT TREATED TEOS-23 ALUMINA-MULLITE CERAMIC SAMPLES AFTER SINTERING AT 1600 °C FOR 12 H, λ : THERMAL CONDUCTIVITY, C_p : HEAT CAPACITY AND D_{TH} : THERMAL DIFFUSIVITY	82
FIGURE 4.26: THE THERMAL BEHAVIOUR OF HEAT TREATED CS-23 ALUMINA-MULLITE CERAMIC SAMPLES AFTER SINTERING AT 1600 °C WITH HOLDING TIME OF 12 H. λ : THERMAL CONDUCTIVITY, C_p : HEAT CAPACITY AND D_{TH} : THERMAL DIFFUSIVITY.....	83
FIGURE 4.27: LINEAR COEFFICIENT OF THERMAL EXPANSION OF TEOS-23 AND CS-23 SAMPLES SINTERED AT 1600 °C FOR 3 H AND 12 H	84
FIGURE 4.28: μ -CT SLICES OF THE ALUMINA-MULLITE CERAMIC SAMPLES AFTER SINTERING AT 1600 °C FOR 12 H; (TOP: TEOS-23; BOTTOM: CS-23 SAMPLE) THERMALLY SHOCKED FROM 1000 °C TO 1200 °C AND QUENCHED WITH WATER. IMAGES OF SAMPLE BEFORE (A, D) AFTER 5 TH (B, E) AND 20 TH (C, F) THERMAL CYCLE	88
FIGURE 4.29: PICTURES OF TEOS-23 AND CS-23 SAMPLES WITH DIFFERENT DIMENSIONS THERMALLY SHOCKED	89

List of Tables

TABLE 2.1: MECHANICAL AND THERMAL PROPERTIES OF ALUMINA	7
TABLE 2.2: SILICA AND SOME PROPERTIES	8
TABLE 2.3: MULLITE MANUFACTURED BY SOL-GEL METHODS	22
TABLE 2.4: PROPERTIES OF SOL-GEL MULLITES DERIVED FROM DIFFERENT STARTING MATERIALS	30
TABLE 2.5: MULLITE MECHANICAL PROPERTIES (AT ROOM TEMPERATURE).....	31
TABLE 2.6: THERMAL PROPERTIES OF MULLITE	32
TABLE 2.7: FRACTURE TOUGHNESS FOR ALUMINA-MULLITE PREPARED FROM INFILTRATION TECHNIQUE	38
TABLE 3.1: MOLAR RATIO OF PRECURSORS AND RATIO OF $\text{SiO}_2:\text{Al}_2\text{O}_3$ DERIVED FOR THE TEOS ROUTE	39
TABLE 3.2: AAS ANALYSIS OF Na^+ IONS IN CS.....	41
TABLE 3.3: MOLAR RATIO OF PRECURSORS AND RATIO OF $\text{SiO}_2:\text{Al}_2\text{O}_3$ DERIVED FOR THE CS ROUTE	41
TABLE 4.1: DIMENSION OF SAMPLES AND CHARACTERIZATION METHODS	58
TABLE 4.2: SHRINKAGE AND MASS CHANGE OF THE COMPACTS SINTERED TO $1550\text{ }^\circ\text{C}$ AT 5 K MIN^{-1} ..	59
TABLE 4.3: SPECIFIC SURFACE AREA (SSA), PORE SIZE DIAMETER AND INTRUDED VOLUME OF MULLITE-ALUMINA SAMPLES	72
TABLE 4.4: MECHANICAL PROPERTIES OF THE SAMPLES TEOS-23 AND CS-23, BOTH SINTERED AT $1600\text{ }^\circ\text{C}$ FOR 12 H.....	78
TABLE 4.5: EVALUATED PARAMETERS	86
TABLE 4.6: DENSITY OF THE CS-23 SAMPLE HEAT TREATED AT $1600\text{ }^\circ\text{C}$ FOR 12 H AND QUENCHED IN WATER FOLLOWING 20 CYCLES.....	87
TABLE 4.7: DENSITY OF THE TEOS-23 SAMPLE HEAT TREATED AT $1600\text{ }^\circ\text{C}$ FOR 12 H AND QUENCHED IN WATER FOLLOWING 20 CYCLES.....	87

1 Introduction and objectives

Mullite is a binary oxide ceramic material composed of alumina and silica. It occurs rarely as a natural mineral, and it was first discovered from a natural deposit at the west coast of Scotland on the Island of Mull. The composition of mullite varies from an alumina-silica molar ratio of $3\text{Al}_2\text{O}_3 \cdot 2\text{SiO}_2$ over $3\text{Al}_2\text{O}_3 \cdot \text{SiO}_2$ to $2\text{Al}_2\text{O}_3 \cdot \text{SiO}_2$. Technical mullite possesses good mechanical properties, even at high temperatures and good thermal shock behaviour [1, 2].

The technical interest in mullite ceramics originate from its properties such as low thermal conductivity, good creep resistance, good chemical and thermal stability, and good mechanical strength in harsh environments. An important feature is its very good resistance to temperature change owing to its low thermal expansion coefficient and its good thermal shock resistance [3]. This makes mullite ceramics interesting candidates for different applications under thermal and mechanical load: Mullite ceramics are candidate materials for structural, electronic and optical applications, serving as engine components, catalyst supports, thermal insulation parts, gas filter supports, heat exchangers, multilayer packaging for electronic devices and window material in the mid-infrared range. Mullite has been fabricated into transparent, translucent and opaque bulk forms [4]. Despite these advantages, mullite ceramics have some limitations due to their brittleness and their high fabrication temperatures [5].

The starting material and the processing of mullite is related to its microstructure and the resultant properties, and new processing techniques are developed to manufacture mullite with suitable microstructure and mechanical and thermal properties. Mullite produced from natural and synthetic raw materials present some differences in its chemical purity and material properties. An apparent disadvantage of using natural minerals is associated with its level of impurities (especially alkali ions such as sodium). These impurities are critical since they lead to a decreased in mechanical properties, and they reduce the melting temperature of mullite ceramics. For instance, the reaction of mullite with alkalis generates carnegieite ($\text{Na}_2\text{O} \cdot \text{Al}_2\text{O}_3 \cdot 2\text{SiO}_2$) acting as a reactive glass phase at high temperatures which affects the material properties [6].

Innovative processing of mullite is focused on synthetic raw materials such as colloidal or molecular precursors. These precursors offer possibilities of the phase formation control and the

mullitization temperature. Mullite ceramics processed by synthetic routes have advantages over powder routes due to their lower processing temperatures and more homogeneous material properties, due to a mixing of Al and Si ions on a molecular level [7].

Plain mullite ceramic materials possess low fracture toughness due to a missing reinforcement phase, and material failure often occurs when heating or cooling rates are too high; as a consequence materials were developed with reinforcement phases [8]. One of these reinforcement phases is alumina. This is due to its high value in flexural strength, fracture toughness, melting temperature, hardness, its good corrosion behaviour and wear resistance compared to mullite. A few reports [9, 10, 11] on alumina–mullite composites have demonstrated better mechanical properties compared to plain mullite; among them one report deals with a core-shell material generated by infiltration processing an improved fracture toughness [12]. However, a correlation between the microstructure, the thermal properties and the thermal shock behaviour of the core-shell alumina-mullite composites produced with the sol-gel process was not shown yet.

The objective of this thesis is to manufacture ceramic parts with an alumina-core/mullite-shell like microstructure and to show correlations between the microstructure, the mechanical, the thermal properties and the thermal shock behaviour of these ceramic materials. As a processing route a sol-gel method was chosen. Two different silica precursors were investigated in this study: A model route consisting of tetraethyl orthosilicate plus alumina powder, and a technical relevant system consisting of dealkalined colloidal silica plus alumina powder.

The samples series were sintered and characterized with respect to their microstructure, porosity and thermal properties. The thermo-mechanical properties were measured. From these properties the thermo shock parameters were calculated and compared. The influence of thermal cycling on the microstructure was monitored with micro-computer tomography (μ -CT).

2 Literature review

2.1 The alumina-silica phase diagram

The fabrication and application of mullite ceramics is based on the alumina-silica phase diagram, and can be controlled by starting materials and processing conditions. Although different mullitization processes have been reported, there is still some uncertainty regarding its melting behaviour and the shape of mullite phase boundaries. Most research points out towards incongruent melting of mullite compared to congruent melting behaviour. Figure 2.1 shows the alumina-silica phase diagram [13].

Mullite solid solution series with molar ratios of $3\text{Al}_2\text{O}_3 \cdot 2\text{SiO}_2$ (60 mol.-% Al_2O_3 , 40 mol.-% SiO_2), $3\text{Al}_2\text{O}_3 \cdot \text{SiO}_2$ (75 mol.-% Al_2O_3 , 25 mol.-% SiO_2) and $2\text{Al}_2\text{O}_3 \cdot \text{SiO}_2$ (67 mol.-% Al_2O_3 , 33 mol.-% SiO_2) have been reported according to different authors [14, 15]. In [16] a $9\text{Al}_2\text{O}_3 : 1\text{SiO}_2$ (90 mol.-% Al_2O_3 , 10 mol.-% SiO_2) molar ratio from sol-gel derived mullite being used in wide spread applications as refractory materials due to a high alumina content is reported. Mullite with the composition $3\text{Al}_2\text{O}_3 \cdot 2\text{SiO}_2$ is identified to be the only stable and crystalline phase of the binary system Al_2O_3 - SiO_2 under atmospheric pressure. Its crystallization behaviour during mullitization is influenced by the nature of starting materials, processing methods, sintering atmosphere and temperature. These factors affect the phase content, the mechanisms of mullite formation and the crystallization patterns as shown by different authors with some differences regarding the solid solubility range of mullite and the exact composition related to the phase diagram [1]. The interactions in a binary system may produce binary eutectic systems, intermediate compounds, solid solution series and different polymorphs as represented in Figure 2.1 [3].

Bowen and Greig [2] used mixtures of synthetic α - Al_2O_3 and silica, and reported an incongruently melting of mullite at 1828 °C with no solid solution range. Toropov and Galakhov [17] reported a congruent melting behaviour of mullite at approximately 1900 °C. Mullite was prepared from a mixture of Aluminium oxide gel and quartz. Thus, Figure 2.1 represents the revised alumina-silica phase diagram of Aramaki and Roy [13]. They prepared quenched samples of dry mixtures of reagent-grade α - Al_2O_3 and powder SiO_2 glass. They reported a congruent melting point for mullite at 1850 °C. They also observed a silica-mullite eutectic temperature of 1587 °C, and 1828 °C for mullite-alumina.

Davis and Pask [18] determined a solid solution range of 71 wt.-% to 74 wt.-% of mullite to 1750 °C. They used semi-infinite diffusion couples of sapphire and fused silica. Other authors described different behaviours [19, 20, 21], until Klug et al. [22] used aluminium oxide hydroxide [AlO(OH)] and tetraethoxysilane (TEOS) to generate homogeneous aluminium silicate powders with a sol-gel processing technique. They reported incongruent melting for mullite at 1890 °C and shifting of both boundaries of mullite solid solution series to higher alumina content at temperatures above 1600 °C. A mullite composition of 67 mol.-% Al₂O₃ and 33 mol.-% SiO₂ was observed at a eutectic temperature of 1587 °C which is partially within the temperature range reported by others [23, 24].

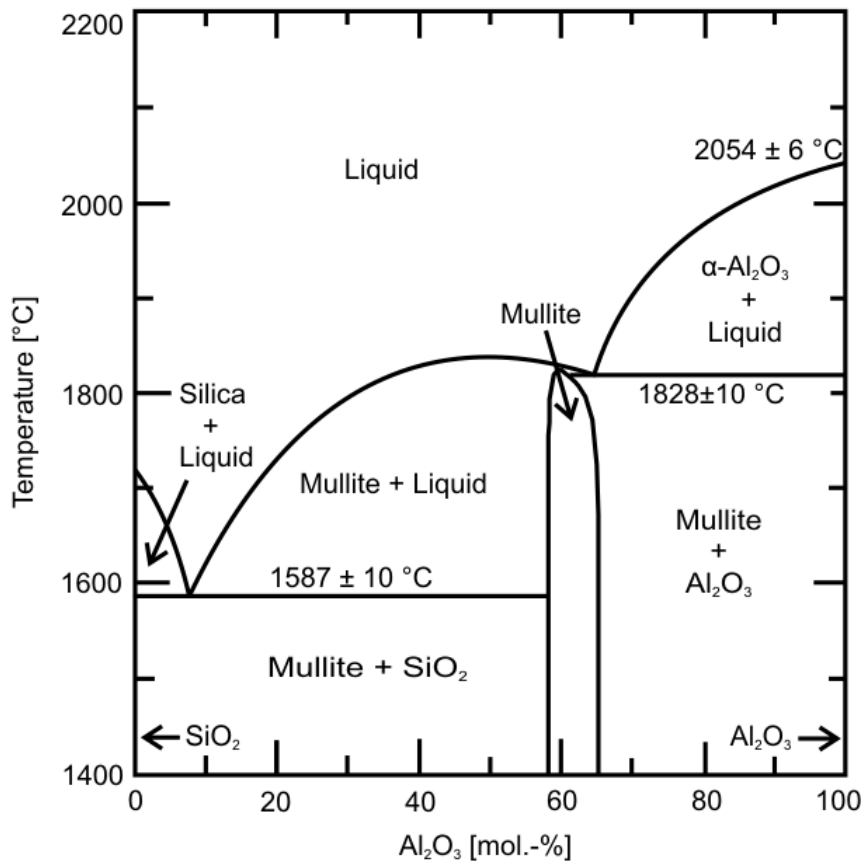


Figure 2.1: Silica-alumina binary phase diagram extracted from [13].

Review papers by Pask et al [25, 26] and Klug [22] summarized the observations of the different authors based on classifying stable and meta-stable reaction products in accordance to the different patterns. They observed that mullite under equilibrium conditions melts incongruently in the presence of α-Al₂O₃ while in the absence of α-Al₂O₃ mullite shows non-equilibrium congruent

melting. Kleebe et al. [27] prepared 3/2-mullite from amorphous silica spheres and different Al_2O_3 powders. They reported that both stable and meta-stable mullite formation occur simultaneously. Despite these many efforts to explore mullite phase formation, controversy persists about its melting behaviour. It is still under debate if mullite melts congruently or incongruently [1].

2.2 The molecular structure of alumina

Alumina is amphoteric and is commonly produced by the Bayer process from bauxite. It does also occur in ruby and sapphire as form of the mineral corundum with some impurities [28, 29]. Alumina or aluminium oxide produced from bauxite includes; calcine alumina, low soda alumina, reactive alumina, tabular alumina, and fused alumina with different alumina purities and particle sizes. Structural differences are associated with the particle size, the surface area, the surface reactivity and its catalytic properties. Figure 2.2 represents the thermal transformation of aluminium hydroxides to different forms following thermal activation [30, 31].

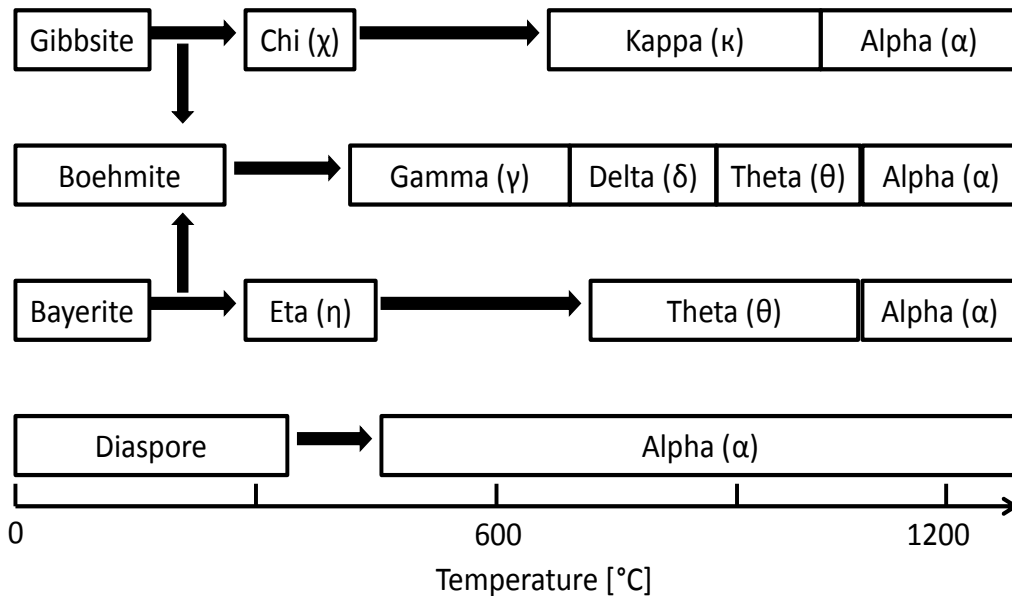


Figure 2.2: Thermal transformation of aluminium hydroxides [30]

Alumina (Al_2O_3) is reported to exist in several allotropic forms. The most thermodynamically stable phase is named alpha-alumina ($\alpha\text{-Al}_2\text{O}_3$) or corundum. Transitional alumina precursors processed at low temperature convert to $\alpha\text{-Al}_2\text{O}_3$ at higher temperatures as shown in Figure 2.2.

Metastable forms or transitional alumina types include: γ -alumina, κ -alumina, δ -alumina, σ -alumina, θ -alumina, β -alumina and χ -alumina (where: γ = gamma, κ = kappa, δ = delta, σ = sigma, θ = theta, β = beta, χ = chi,). These phases are formed during thermal decomposition of Aluminium hydroxides or Aluminium salts [32]. For example, gibbsite (γ -trihydrate; γ -Al(OH)₃), boehmite (γ -monohydrate; γ -AlOOH), bayerite (α -trihydrate; α -Al(OH)₃) and diasporite (α -monohydrate; α -AlOOH) upon heat treatment transformed at high temperatures to different crystalline forms [33, 34].

As mentioned, the most common crystalline phase of alumina is corundum. The crystal structure is described by a hexagonal unit cell shown in Figure 2.3 (left). This structure shows a compact hexagonal stacking of O²⁻ anions with two-thirds of the octahedral interstitial sites occupied by Al³⁺ cations [35]. Its structure is a trigonal lattice with space group R3c. Its unit cell dimensions are: a = 4.7587 Å, b = 4.7587 Å and c = 12.99 Å. The Al atoms are octahedrally coordinated with six oxygen atoms, see Figure 2.3 (right) [36].

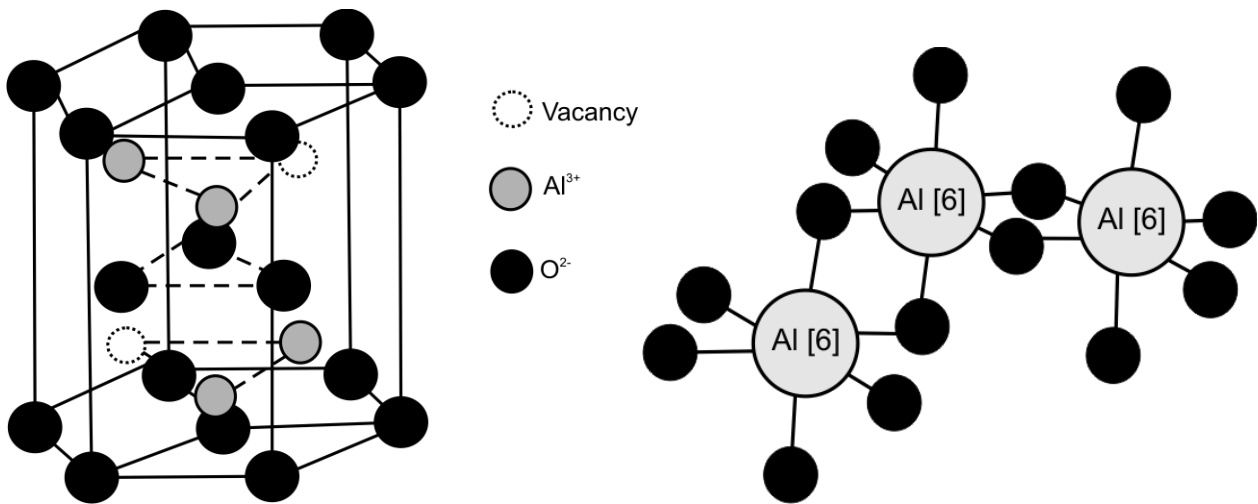


Figure 2.3: (left) Corundum structure in α -Al₂O₃ and (right) octahedral coordination of α -alumina [33]

Alumina's typical properties (see Table 2.1) include: high hardness, chemical inertness, high thermal stability, low coefficient of thermal expansion, good thermal conductivity, good wear and abrasion resistance, high corrosion resistance, a high melting temperature (2050 °C), and its commercial availability in different purity ranges and grain sizes, makes it attractive for a great variety of engineering applications [28]. The alumina's suitability to resist thermal fatigue is

related to its manifold component geometry and strength, and it is controlled by its thermal properties such as thermal conductivity and thermal expansion characteristics [37].

Typical engineering applications of alumina ceramics are outlined as follows:

- as a refractory material for lining of furnaces [38].
- as an abrasive material and cutting tools [37].
- as substrate material for electronic parts and packing materials for integrated circuits (e.g. silicon chips, electrical insulators and spark plugs) [29].
- alumina also has wide spread applications as a porous ceramic and catalyst support [39].

Table 2.1: Mechanical and thermal properties of alumina [37, 40]

Characteristics	Measured values
density, [g cm ⁻³]	3.95-4.10
melting point, [°C]	2072
microhardness, [GPa]	20
hardness, [GPa]	9
young's modulus, [GPa]	260-410
bending strength, [MPa]	150-600
fracture toughness, [MPa m ^{0.5}]	4-6
thermal conductivity from 25 °C to 1000 °C, [W m ⁻¹ K ⁻¹]	30-40
coefficient of thermal expansion from 20 °C to 1000 °C, *10 ⁻⁶ [K ⁻¹]	5.4-9.5

2.3 Silica and its molecular structure

Silica is a collective name for a compound made of silicon and oxygen with the chemical formula SiO₂. It occurs naturally, e. g. as sandstone, silica sand or quartz, and can be manufactured from different precursors in to several forms including fumed silica, fused silica, colloidal silica and silica gel [41]. For example, silica can be form from alkoxide as represented in Eqn. (2.1) [42]



Desired stable phases in mullite formation are found to occur only after phase transformations with significant nucleation and growth within heterogeneous amorphous materials. Mullite processed from amorphous silica precursors represents a more thermodynamically stable phase compared to crystalline silica materials. An improved mullite microstructure is controlled by the choice of the silica precursor, the alumina precursor and processing conditions and more details will be given in section 2.5.

Silica exists in a number of different crystalline forms or polymorphs with three major forms being quartz, tridymite and cristobalite, as listed in Table 2.2. At low temperatures and pressures the most stable form of silica is quartz. The α -form and the β -form indicate low and high temperature polymorphs of one another. The β -cristobalite is stable to approximately 1705 °C and melts at higher temperatures ≥ 1705 °C [43].

Table 2.2: Silica and some properties [44, 45]

Form	Crystal symmetry	Stable range	Density [g cm⁻³]
α -quartz	hexagonal	< 573 °C	2.65
β -quartz	hexagonal	573 °C - 870 °C	2.53
α -tridymite	monoclinic	metastable	2.36
β -tridymite	hexagonal	870 °C - 1470 °C	2.25
α -cristobalite	tetragonal	metstable	2.32
β -cristobalite	tetragonal	1470 °C - 1705 °C	2.20
Silica melt	-	≥ 1705 °C	-

The crystal structure of the high temperature thermodynamically stable crystalline silica form is shown in Figure 2.4. Each silicon atom is covalently bonded to four oxygen atoms tetrahedrally, and every oxygen atom is bonded to two silicon atoms [46]. The silica group represents different minerals with different structures, symmetries and physical properties but with the same composition. This is enabled by the changes in bond angles of the SiO₄ tetrahedron and Si-O bond lengths. Structural transformations following the increase in temperature cause the relative positions of the atoms in the crystal lattice to get shifted slightly. The Si-O-Si bond angles (the bond angle between the SiO₄ tetrahedra) change from 153° (β -quartz) via 180° (β -tridymite) to 151° (β -cristobalite). A shift is induced in the bond length of Si-O resulting in a contraction from

0.161 nm (α -quartz) to 0.158 nm (β -cristobalite). A corresponding decrease in density and an increase in hardness are discussed in [44].

Silica has a large number of industrial uses and it does provide the essential SiO_2 component of mullite and glass formulations. It has a high melting temperature used to produce moulds and cores for the production of metal castings in ferrous and non-ferrous industries [47]. Additionally, silica low thermal conductivity ($7 \text{ W m}^{-1} \text{ K}^{-1}$) and coefficient of thermal expansion ($5.5 \cdot 10^{-7} \text{ K}^{-1}$) produce stable cores and moulds compatible with pouring temperatures [48]. Silica is a component for formulations of ceramic products (e.g. tableware, sanitary ware, floor tile and wall tile). For example, in composite ceramic processing, silica is the skeletal structure upon which clay, alumina and other components are attached. Silica is used to regulate drying and shrinkage; it modifies the thermal expansion and improves the structural and mechanical properties [41].

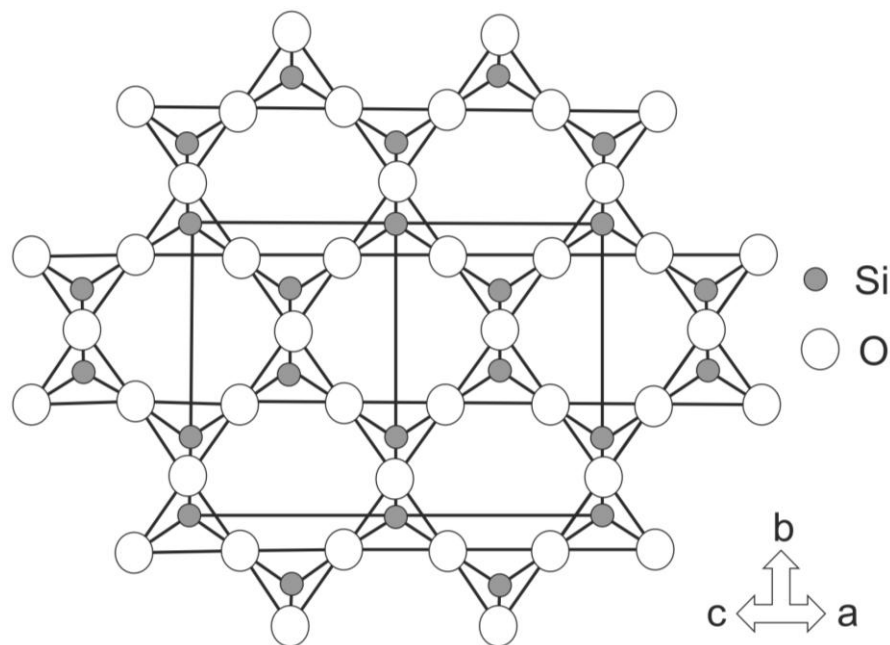


Figure 2.4: Crystal structure of β -cristobalite (high temperature crystalline form of silica) [44]

2.4 The molecular structure of mullite

Mullite is a ceramic material in the system silica-alumina. It is represented by the general formula $\text{Al}_4(\text{Al}_{2+2x}\text{Si}_{2-2x})\text{O}_{10-x}$, where x varies from 0.17-0.50 [49, 50]. Mullite with compositions

containing 55 mol.-% to 90 mol.-% Al_2O_3 has been manufactured based on different material types and processing techniques [3]. High temperature mullite ($3\text{Al}_2\text{O}_3 \cdot 2\text{SiO}_2$) has a density of approximately 3.1 g cm^{-3} and it is found to be the most thermodynamically stable crystalline form under high pressure and temperature [51]. Mullite material represents amorphous and crystalline structures including: Spinel, tetragonal and orthorhombic. The formation of a spinel or amorphous phase is an indication of precursor heterogeneity and it is controlled by the hydrolysis rate and sintering temperature. The tetragonal structure is metastable and is characterized by a single peak in x-ray diffraction patterns at 26° ($2\theta\text{-CuK}_\alpha$) while the orthorhombic structure is more stable and the crystal shows a doublet in the x-ray diffraction patterns at 26° ($2\theta\text{-CuK}_\alpha$) [52]. Figure 2.5 represents a projection of the mullite crystal structure parallel to the c-axis (001).

The crystal structure of mullite is orthorhombic with the space group Pbam and cell dimensions of $a = 0.755 \text{ nm}$, $b = 0.768 \text{ nm}$ and $c = 0.288 \text{ nm}$. The mullite structure consists of chains of edge-sharing AlO_6 -octahedra cross linked by $(\text{Si}, \text{Al})\text{O}_4$ tetrahedra with double chains which run parallel to the c-axis. Its structure is obtained by a substitution of Si^{4+} by Al^{3+} in the SiO_4 tetrahedra sites. To maintain the charge neutrality, vacancies are created to produce charge balance [49], see Eqn. (2.2).

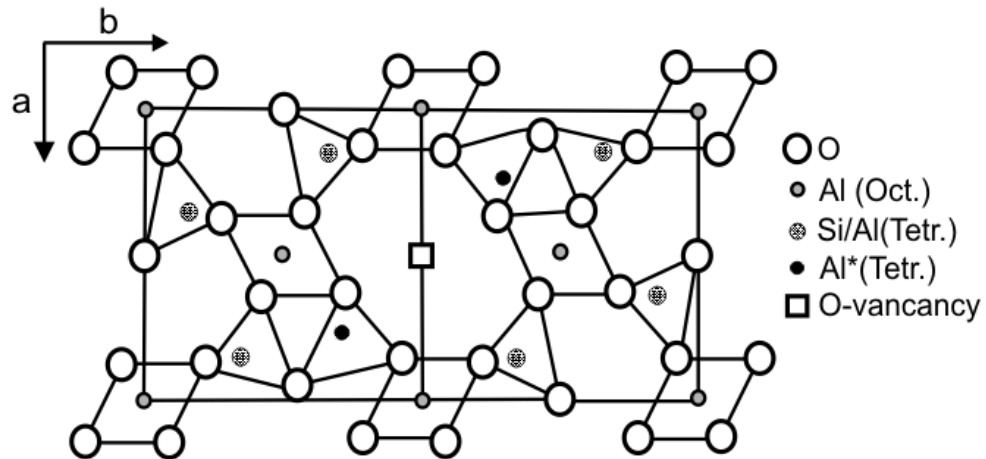


Figure 2.5: Projection of crystal structure of mullite along the c-axis (001) [53]



where \bullet : positive charge, $'$: negative charge, V_0 : oxygen vacancy

The Al/Si ratio determines the number of vacancies and for mullite with a composition of $3\text{Al}_2\text{O}_3 \cdot 2\text{SiO}_2$, there is on averages an oxygen vacancy for every four unit cells. Analysis with ^{29}Si and ^{27}Al nuclear magnetic resonance spectroscopy (NMR) provides information of the degree of order, as in mullite described in [15, 54]. X-ray diffraction studies made by Paulmann [55] showed that the ordering scheme of oxygen vacancies, tetrahedral Al and Si is very stable and persists up to the melting point of mullite. This order is reported to influence its thermal stability and has been observed to affect its material properties. In review papers by Schneider et al. [53] it is pointed out that the bonding system of mullite has a major influence on the changes observed in its properties. Mullite properties and applications are discussed in detailed in section 2.5.

2.5 Mullite synthesis, processing and formation mechanisms

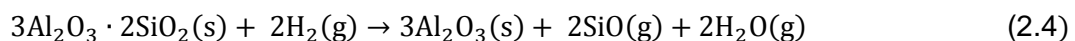
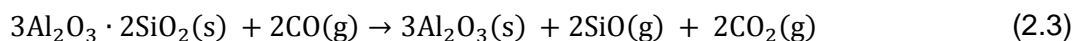
A variety of mullite ceramic processing routes based on different starting materials have been developed; these include: solid-state derived mullite; liquid state derived mullite; sol-gel derived mullite; hydrothermally produced mullite; gas-phase-derived mullite; a spray pyrolysis approach and processing with other miscellaneous methods might be applied [1]. Mullites synthesized by liquid and solid state methods are designated elsewhere as fused-mullite and sinter-mullite respectively, while the other methods are referenced as chemical mullite [3]. In the processing of the aforementioned mullite types, different starting materials have been used [56, 57]. Material homogeneity, which depends on how to mix, precipitate, hydrolyze, or react SiO_2 and Al_2O_3 precursors, and mullite properties depend on the precursor type, synthesis and processing method. Mullite formation mechanisms are controlled by the method of combining its reactants and different mullitization temperatures are reported [58]. Lower temperatures $<1500\text{ }^\circ\text{C}$ are reported for mullitization using sol-gel routes compared to higher temperatures $>1600\text{ }^\circ\text{C}$ for reaction sintering of powdered raw materials [18]. Mullites processing from conventional raw materials (i.e. clay minerals, aluminosilicates, clay/alumina and clay/bauxite) make use of relatively coarse particles, and the mixing is in the order of micrometers [59]. High temperatures are required for diffusion of the reacting species compared to colloidal sols or dispersions with comparatively smaller particle sizes in the nanometer range which provide shorter diffusion paths and higher mullitization rates at lower reaction temperatures [60]. Natural occurring minerals has considerable higher amount of impurities which are undesirable for technical

ceramic applications [6]. Sol-gel methods with wet mixing of aluminium and silicon bearing species are increasingly being used due to their potential to generate homogenous microstructures and lower mullitization temperatures [7, 61]. The processing of mullite from different starting precursors and methods possesses some differences in mullite crystallization and mullitization behaviour as described in the following sections.

2.5.1 Solid-state processed mullite

Mullite processing from powdered raw materials mixed and heat-treated includes clay minerals, admixtures of boehmite, diaspore and gibbsite with silica. Mullitization takes place by diffusion of aluminium, silicon and oxygen ions through solid-solid or transient liquid reactions controlled by the firing temperature, duration of firing, and composition of the raw materials. Intensive mullitization requires high temperature at up to 1700 °C [3]. Mullite powders produced by reaction of alumina and silica at higher temperatures >1650 °C, showed nucleation and growth processes at an interface region between the alumina and the silica phase. The growth rate is controlled by the diffusion of aluminium and silicon ions through the mullite layer formed [51].

Sacks and Pask [57] observed different factors influencing the sintering process of powders including starting powder characteristics, heating conditions and molar ratios of alumina and silica. They found out that an increase in grinding time of powder breaks agglomerates and produce free surface areas effective to achieve homogeneous compositions and improve the sintering characteristics. Another important factor is the sintering atmosphere, in which mullite was observed to decompose or enrich under reducing (carbon monoxide or hydrogen or helium gas) and oxidizing (oxygen) conditions, respectively [18]. At high temperatures (i.e. from 1650 °C to 1800 °C) in reducing conditions carbon dioxide or hydrogen react with mullite and subsequent formation of gaseous reaction products are created according to Eqn. (2.3) and Eqn. (2.4)



The loss of silica leaves a porous product of alumina on the surface layer and prolonged exposure decreases the material density and strength. This explains the poor resistance of mullite refractory bricks in reducing atmospheres [62, 63]. In Comparison, repeated heating of

mullite-corundum in oxidizing atmospheres (synthetic air) enhanced the sintering process, and mullite formation increases owing to the reaction of corundum with silica [64].

Mullite produced from solid state derived methods shows low strength and fracture toughness caused by defects from clay minerals [20]. Mullite materials such as bricks, crucibles and tubes have been produced with a decreased quality of the mullite ceramic due to high processing temperatures, defects and relatively large grain size of starting materials [65].

2.5.2 Fused-mullite (liquid-state-processed mullite)

Fused mullites are produced by melting of Al_2O_3 and SiO_2 powders or raw materials containing Al and Si precursors, in electric furnace above 2000 °C. Some examples of raw materials used include alumina from the Bayer process, quartz sand, and fused silica. Melts obtained from the mentioned aluminium silicates were poured into ingot molds and cooled to room temperature [1]. The crystallization temperature and cooling speed determined its chemical composition, and to some extent the starting materials as well. The impurity content depends on the initial raw materials, and very high melting temperatures are required [19]. Mullite produced with these methods shows a high density (3.3 g cm^{-3}), a low porosity (1%) and a small amount of glassy phase due to incomplete crystallization [23].

Fused-mullite with a composition of 76 mol.-% Al_2O_3 is reported richer in alumina compared to 60 mol.-% Al_2O_3 for solid state derived mullite. Fused-mullites with compositions in the range of 2/1-mullite are produced for commercial applications, with a low amount of glass compared to that produced by solid state reactions. The crystal sizes for sinter-mullites are controlled by the firing temperature, the duration of firing and the composition of the raw materials. In comparison, the crystal size of fused-mullite is a function of the cooling conditions of the reaction bath. Relatively large variations of the microstructure are reported for fused-mullites compared to sinter-mullite which have a homogeneous microstructure [3, 24]. The starting material characteristics and processing techniques present a large variation in microstructure and mechanism of liquid and solid state derived mullites [1, 66].

The reactions pathways of alumina and silica powders have been used to evaluate the mechanisms of powder route processing, described as reaction sintering of alumina and silica precursors. Several authors [18, 67] reported reaction sintering of mullite precursors. Johnson

and Pask [59] observed mullite crystal formation on $\alpha\text{-Al}_2\text{O}_3$ grains by diffusion of Al and Si ions. Following their observations, mullite formation mechanisms have been evaluated by a number of authors in those systems including quartz-alumina, silica-glass-alumina and cristobalite-alumina at different temperatures up to 1700 °C, see Figure 2.6 [69-75].

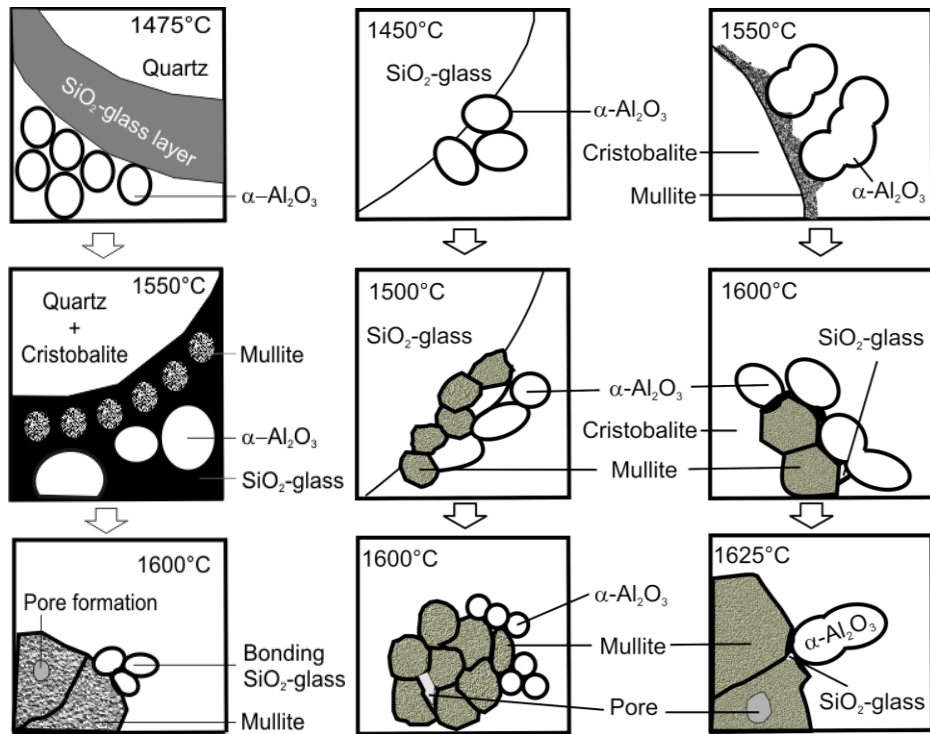


Figure 2.6: Reaction sintering mechanism: (left) quartz-alumina, (middle) silica-glass-alumina and (right) cristobalite-alumina

The authors observed that the reaction rate and the densification rate depend on the reactant type and to some extent on the particle size of the starting materials. They found that mullite formation is a multiple-step process identifying regions of mullite nucleation and mullitization described in terms of stages in [3]. Mullite nucleation occurs between 1450 °C and 1470 °C, followed by a region with a high reaction rates from 1470 °C to 1530 °C. The formation rate then decreases with increasing temperatures from 1530 °C to 1580 °C, due to almost complete crystallization of the silica glass phase to the less reactive cristobalite [68]. Diffusion barriers are formed at the contact areas of silica and alumina compounds, due to mullite formation at their interfaces. The mullitization rate increases again at temperatures >1650 °C. This is associated with a rapid liquid-phase controlled mullitization enabled by the melting of residual cristobalite

grains [69]. Significant differences in terms of densification, nucleation and mullitization are determined based on different material systems and processing strategies; the main ones are presented as follows.

In the quartz-alumina system (Figure 2.6 (left)), the reaction of peripheral quartz grains start melting at $<1100\text{ }^{\circ}\text{C}$, since the mother quartz material contains a small amount of impurities, a glass is formed which enables sintering at this low temperature [70]. Figure 2.7 (left) represents the variations in the silica compositions with increasing temperatures for the mentioned systems. The glass formation with simultaneous densification starting at lower temperatures is observed for quartz-alumina and silica glass-alumina systems compared to the cristobalite-alumina system with initial densification starting above $1400\text{ }^{\circ}\text{C}$, shown in Figure 2.7 (left). Initial mullite formation in the quartz-alumina system was observed at $1470\text{ }^{\circ}\text{C}$ compared to higher temperatures in the other systems due to the densification enabled by impurities at lower temperatures (i.e. alkali metals), see Figure 2.7 (bottom-left) [71].

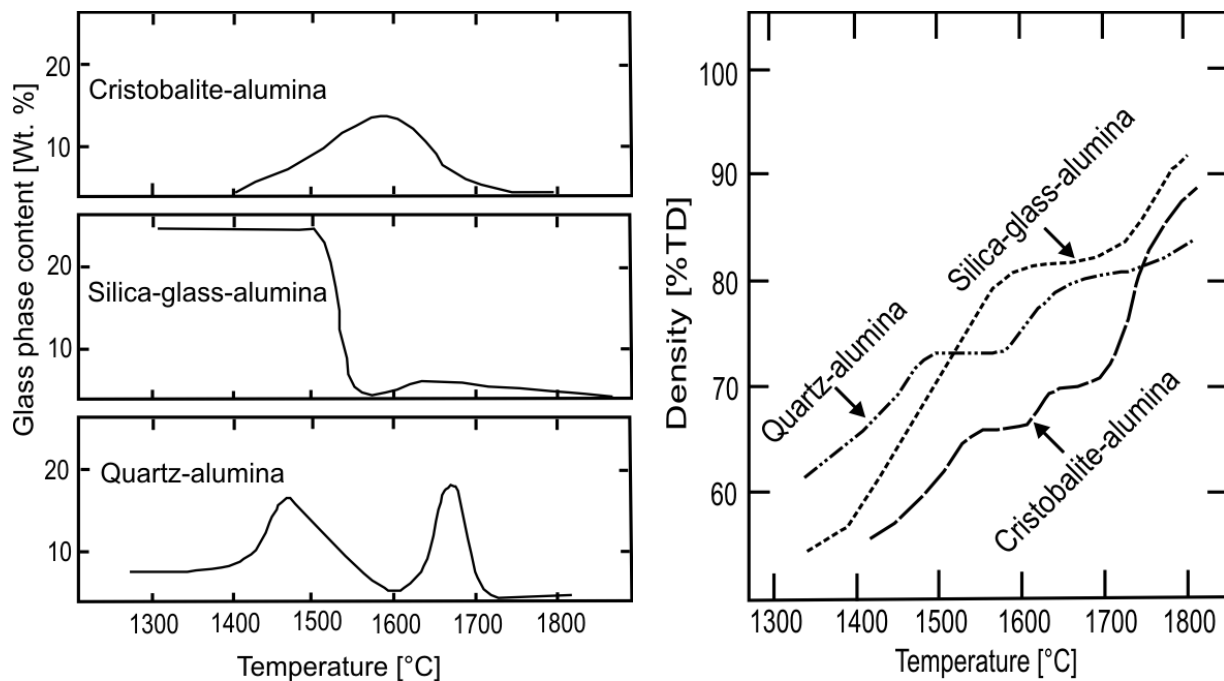


Figure 2.7: (Left) Glass phase reactions: Quartz-alumina (bottom), silica glass-alumina (middle), cristobalite-alumina (top) and (right) densification of alumina and silica [3]

In the silica glass-alumina system (Figure 2.6 (middle)), amorphous silica transformed to cristobalite and coexists from $1450\text{ }^{\circ}\text{C}$ to $1650\text{ }^{\circ}\text{C}$ with an amorphous silica-rich liquid phase

formed above 1550 °C. The mullite formation started above 1500 °C and slowed down from 1550 °C-1600 °C, and increased rapidly above 1600 °C according to the changes in the silica amount controlled by heat treatment (Figure 2.7 (middle-left)). At approximately 1450 °C, the fine alumina particles penetrate into the viscous silica particle surfaces represented in Figure 2.6 (middle). The mullite formation was observed at 1500 °C by the reaction of alumina with silica particles [71]. The alumina particles adhere strongly, and the surfaces of the silica particles became rounded with increasing temperatures. The silica glass starts to transform to cristobalite. The mullitization occurs by the reaction of cristobalite with corundum above 1500 °C. Newly formed mullite grains grow developing a ring-like mullite grain around the former silica glass particles. This creates barriers that increase the diffusion distances for Al and Si ions and reduces the mullitization rate. A temperature increase above 1600 °C enables rapid liquid-phase assisted sintering which caused melting of cristobalite and promotes further mullitization with pore evolution as observed in [71, 72].

For the cristobalite-alumina system in Figure 2.6 (right), the densification occurs at 1300 °C by the rearrangement of cristobalite and corundum particles under mullite formation similar to the silica-glass-alumina system as described previously. This system showed formation of contact points and the mullite formation with the formation of neck areas above 1500 °C. Alumina particles attached onto the cristobalite particle surfaces by the neck formation showing a low degree of shrinkage as compared to the silica-glass-alumina system. These particles form contact points allowing for diffusion of ions giving rise to the growth of the neck areas. At temperatures higher than 1600 °C, cristobalite melts. Above 1625 °C, cristobalite is converted into a silica-rich liquid phase which improves the densification by liquid-phase-assisted sintering. A secondary densification after mullitization is reported to occur in cristobalite-alumina systems but not in the silica-glass-alumina system [73].

Figure 2.7 (right) represents the densification curves for quartz-alumina, silica glass-alumina and cristobalite-alumina systems. The quartz-alumina system showed intense shrinkage from 1000 °C-1400 °C due to assisted liquid phase densification indicated by the high amount of glass formed in this region, Figure 2.7 (bottom-left). The shrinkage decreases to 1520 °C to approximately zero due to the mullite volume increase. Less shrinkage and densification occur in cristobalite-alumina systems prior to 1450 °C. An increase in temperature to 1520 °C and a higher shrinkage rate enabled by solid-state diffusion sintering reaction were observed. At

temperatures above 1650 °C, the densification rate increased through liquid-phase sintering enabled by the fusion of cristobalite grains, Figure 2.7 (top-left). The system silica glass-alumina shows higher densification rates at lower temperatures compared to cristobalite-alumina, Figure 2.7 (middle-left). The silica glass content drops in a temperature range from 1400 °C to 1520 °C followed by the transformation to cristobalite. A liquid-phase or semi viscous assisted sintering process characterized the quartz-alumina and silica-glass-alumina system at temperatures ≤ 1500 °C. Solid-state diffusion is the major sintering mechanism for the cristobalite-alumina system at this temperature. The mullite formation rate up to 1530 °C is higher in the silica glass-alumina system and the quartz-alumina system than in the cristobalite-alumina system due to intense the pre-mullite viscous flow densification with shorter diffusion paths for Al and Si ions. At higher temperatures (>1600 °C) liquid-state assisted mechanisms for the different systems with approximately 80 % (silica-glass-alumina) and 90 % (cristobalite-alumina) mullite formed at 1700 °C were observed. Above 1750 °C, all samples showed almost complete mullitization [74].

2.5.3 Mullite from chemical routes

Chemical synthetic routes are promising techniques when lower processing temperatures and a homogeneous microstructure is required. For the manufacturing of synthetic mullite, different routes such as sol-gel processing, co-precipitation, chemical vapour deposition, and processing with different precursor materials may be applied [3]. An overview of these routes and some mechanisms are reviewed as follows.

Sol-gel processing routes

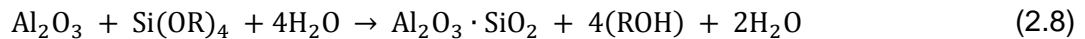
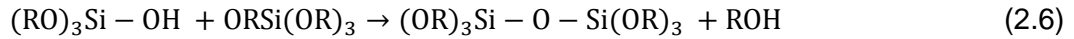
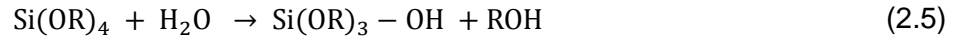
These methods deliver uniformity of starting materials and enable the control of the local phase distribution through atomic and nano-scale mixing of the reactants resulting in an improved microstructure and homogeneous material properties. Sol-gel processes make use of precursors to be mixed and brought out of solution either as a colloidal gel or polymerized macromolecular $\text{SiO}_2\text{-Al}_2\text{O}_3$ network while retaining the water. The water serves as transport medium and provides hydrolysis conditions, and can be desiccated off leaving behind a solid with some level of porosity [75, 76, 77]. Parts and forms of materials with controlled compositions and purities may be achieved more efficient as compared to powder processing routes [78, 79, 80]. Three types of precursor gels have been postulated for mullite crystallization by sol-gel processes:

- type I precursor (single-phase gel) in the as-prepared state is amorphous and transforms to mullite at temperatures at about 950 °C. It can be prepared from organosilicon and organoaluminium compounds. The diffusion is slow and the densification is difficult due to low processing temperatures [61].
- type II precursor (diphasic mullite precursors) in the as-prepared phase contains pseudo-boehmite and amorphous silica. Pseudo-boehmite transforms into the spinel phase at about >400 °C and to mullite >1250 °C, and it is derived from colloidal precursor suspensions [79, 81]. The structural transformation of type II mullite shows the development of a spinel-type transition alumina and mullite formation below 1200 °C and above 1250 °C, respectively [82].
- type III precursor is amorphous in the as-prepared state and is preceded by the formation of weak crystalline transient alumina as cubic Al-Si spinel or γ -Al₂O₃ at 980 °C, which then reacts with amorphous silica to form mullite at <1200 °C. It can be prepared from mixtures of TEOS and aluminium-sec-butylate [83].

The reaction kinetics for the mullite formation varies according to the different gel precursors and the methods employed. Mechanisms for mullite formation from the different gels have been studied using X-ray diffraction and differential thermal analysis (DTA). Mullite formation from a single gel is based on a nucleation-controlled growth mechanism with an initial mullite formation temperature of about 980 °C compared to mullite formation in diphasic precursors, which shows a diffusion-controlled growth mechanism with initial mullite formation temperatures of up to 1250 °C [61]. In sol-gel processes, the desired stable phases are obtained through a careful selection of materials and processing conditions, and they have been evaluated based on different starting materials. The effect of processing conditions (i.e water amount, catalyst type and solvent type) is reviewed in connection with some mechanisms, followed by an overview of the different sol-gel processes (i.e. solution-plus-solution, solution-plus-sol and sol-plus-sol processes).

In the processing of the mentioned precursors gels, results have been obtained regarding precursor hydrolysis, condensation, cross-linking, and crystallization behaviour, which are linked to the precipitation of the sol species as aggregated particles, precipitation of un-aggregated particles, and formation of a homogeneous gel [84]. The difference in the reactivity of the metal alkoxides with water makes it difficult to control the homogeneity and composition of the resultant mullite due to phase segregation effects. In Eqn. (2.5) to (2.8) and Figure 2.8, the

overall reactions for hydrolysis (Eqn. (2.5)), condensations (Eqn. (2.6) to (2.7)) and reaction mechanisms (Figure 2.8) of metal alkoxides in sol-gel systems for mullite synthesis are presented, which shows the formation of silica glass (Eqn. (2.7)) and mullite (Figure 2.8).



R: alkyl groups, Eqn. 2.5: hydrolysis, Eqn. 2.6 to 2.7: condensation

In the processing, water is used as a hydrolysis medium and acids (e.g. hydrochloric acid) or bases (e.g. ammonia) are added as catalysts for hydrolysis of the alkoxides, and the process is carried out at room temperature. It requires moderate temperature to age the gel, and to remove the water and solvents [85].

The reaction mechanisms for acid catalysts or base catalysts are schematically shown in Figure 2.8. Under acidic conditions hydrolysis is predominant over condensation reactions. The formation of protonated silanol species are favoured, but inhibits some nucleophiles. This results in a high solubility of metal inorganic salts or alkoxides precursors in such gels. A short ageing time and slow evaporation of the solvent is observed with dense materials achieved and some small pores under acidic conditions [3].

In basic conditions hydroxyl ions (OH^-) and deprotonated silanol groups are better nucleophiles than water and silanol species in acidic conditions. There is a fast attack on the silicon atom, hydrolysis and condensation occur simultaneously. Large amount of water is used, with low solubility of metal inorganic salts or alkoxides precursors. A long ageing time and rapid solvent evaporation is observed with particular gels with high porosity. The polymerization behaviour of metal alkoxides or inorganic salts in basic solution represents a growth in size and a decrease in the number of particles, while in acidic solutions particles aggregate in three dimensional networks and form gels [41].

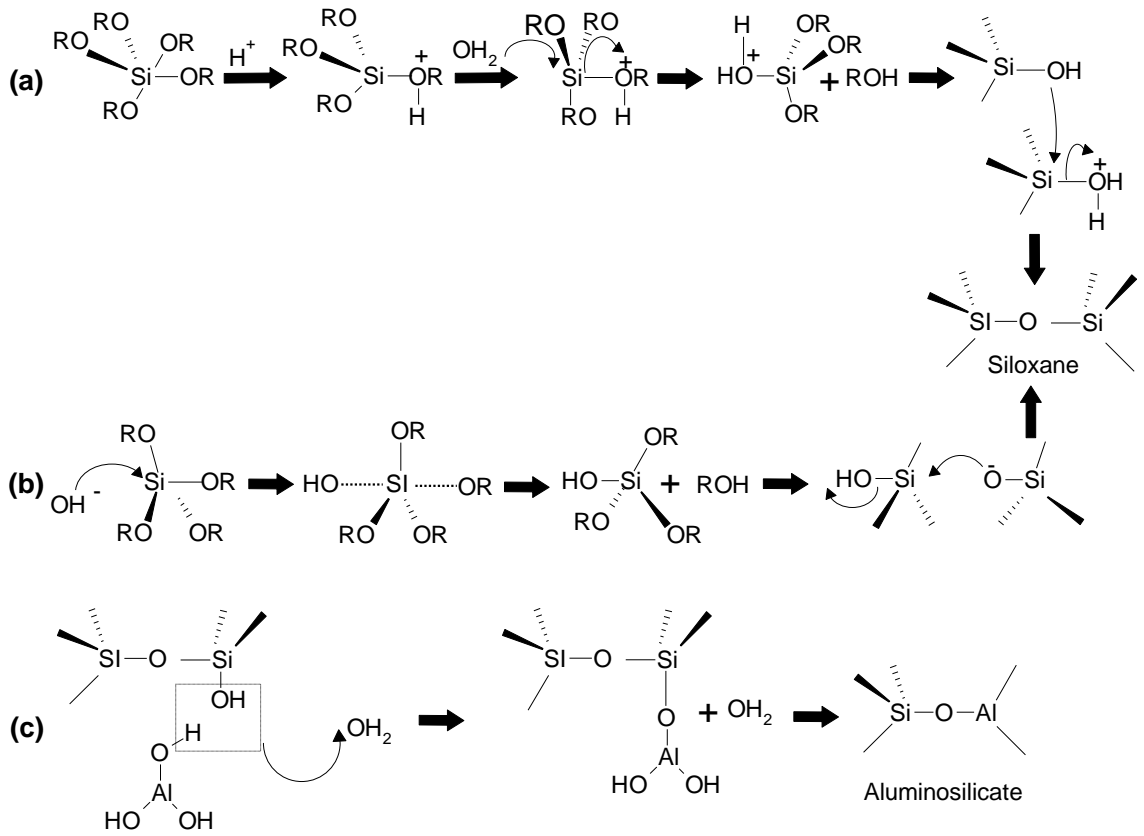


Figure 2.8: Hydrolysis reactions between the silicon alkoxide and water with an acid catalyst (a), base catalyst (b), and (c) cross linking reactions between silanols and Aluminium hydroxide at the hydrophilic surface with the formation of $\equiv Si-O-Al=$ bonds. OR = ethoxy or methoxy groups [86]

Steric hindrance affected by bulky alkoxide groups of silicon and aluminium reduces the reaction rate and lead to chemical in-homogeneities at an atomic level, and the mullite crystallization starts at higher temperatures [7, 87]. According to Eqn. (2.6), $Si(OR)_3(OH)$ in the presence of a basic catalyst (e.g. ammonia) is more susceptible to attacks by the hydroxyl radical than those of $Si(OR)_4$ due to a reduced electron density. Hence Si-O-Si bonds are easily formed during ageing with functional groups with reduced steric hindering as described in Eqn. (2.7). The OH groups at the hydrophilic surface of the silanol and aluminium hydroxide under influenced of heat undergoes condensation with elimination of water under the formation of $\equiv Si-O-Al=$ bonds, schematically shown in Figure 2.8. For example, delayed or accelerated polymerization of silica affects the structural arrangement of SiO_4 -tetrahedra within the mullite structure differently [88].

Polymeric gels or gels with less bulky alkoxy groups showed short-rate diffusion through the mixed precursors with crystallization of the spinel-type phase and mullite occurs at 980 °C. Colloidal gels containing bulky alkoxy groups require long-diffusion. Mullitization does not occur from mixtures of amorphous silica and transitional alumina until temperatures are more than 1250 °C [8]. On the other hand, if an acidic catalyst is used, the Si(OR)_4 species are much more susceptible to the attack by the OH^- ions [1].

Paulick et al. [89] evaluated the role of the pH value, the reaction time and the temperature for mullite gels using aluminium isopropoxide and TEOS precursors. They reported that intimate gel mixing occurs at low pH values where the hydrolysis predominates over condensation [85]. The effect of the pH value on mullite synthesized from single gels and diphasic gels were reported by Chakraborty [90] and Lee et al. [85]. The former authors showed that when the pH value was between 4 and 4.5, mullite crystallization was observed at 980 °C and is shifted to higher temperatures in diphasic gels with $\text{pH} \leq 1$ or ~ 14 . This happens because the silica sol loses its stability rapidly due to the diminution of the negative charge of the sol by the Al^{3+} ion. In the later case, samples prepared from aluminium nitrate nonahydrate and colloidal silica sols showed that when the pH value was less than 2, granular mullite was found at a temperature of 1200 °C compared to temperatures higher than 1200 °C for a pH value greater than 8 [7].

Fourier transform infrared spectroscopy (FTIR) studies of gels prepared from boehmite and TEOS in the temperature range from 400 °C to 1000 °C showed the presence of nanostructured alumina, silica and alumina-silica agglomeration in the amorphous state. The presence of tetra-coordinated and octa-coordinated aluminium were also found below 1000 °C. This indicates the formation of transitional spinal phases, which were characterized by DTA and XRD methods [91, 92]. Samples sintered in the range from 1200 °C to 1300 °C have shown an increased intensity for $\equiv\text{Si-O-Si}\equiv$ (see Figure 2.8 (a, b)) and $\equiv\text{Si-O-Al}\equiv$ (see Figure 2.8 (c)) bands [93]. Different starting materials have been used with the addition of acidic catalysts or base catalysts and solvents for sol-gel mullite processing, as reviewed in [94].

Starting materials of mixtures of sols, salts and admixtures of sols and salts have been used to evaluate the mechanism of the formation of sol-gel-derived mullites. The reactivity of the different sol-gel starting materials such as aluminium nitrate nonahydrate, aluminium isopropoxide and boehmite and silica alkoxides such as tetraethylorthosilicate and

tetramethylorthosilicate in the presence or absence of solvents (e.g. methanol, 1-propanol, 1-butanol and ethylene glycol), catalysts (e.g. hydrochloric acid, ammonia solution) and water are listed in Table 2.3. A review of the different sol-gel processes is discussed below, classified into solution-plus-solution, solution-plus-sol and sol-plus-sol processes [1]. The schematic model for the different sol-gel mechanisms proposed for the nucleation and growth of mullite is represented in Figure 2.9, and it has been used to classify the mixing behaviour of the aforementioned sol-gel processes.

Table 2.3: Mullite manufactured by sol-gel methods

Reactants	Temp. [°C]	Formed phases
silica sols + alumina sols + HCl	1200	spinel → mullite ^x [95]
aluminium salt + silica sol	1000	spinel → mullite (above 1200 °C) [96]
monosilicic solution + Al(OH) ₃ sol	980	tetragonal-like mullite (980 °C) [96]
TEOS + Al(OC ₄ H ₉) ₃ + alcohol + water	1200	spinel → orthorhombic mullite [97]
TEOS + ANN + ethanol	980	tetragonal mullite [98]
TEOS + ANN + water + NH ₃	1300	tetragonal mullite + spinel (1200 °C) → tetragonal mullite [97]
TEOS + ANN + water + urea	1300	tetragonal mullite (980 °C) → orthorhombic mullite [99]
TEOS + AIP + ethanol + water	1200	spinel + orthorhombic mullite (1000 °C) → orthorhombic mullite [52]
TEOS + boehmite + water	1250	spinel → orthorhombic mullite [100]
TEOS + AlCl ₃ ·6H ₂ O + water + alcohol + NH ₃	1350	δ-alumina → (δ,θ)- alumina → mullite + (δ,θ)- alumina (1250 °C) → mullite [101]
colloidal silica + ANN + water	1200	θ- alumina → mullite ^x + cristobalite [85]
colloidal silica + Al ₂ (SO ₄) ₃ + Urea	1000	spinel → mullite ^x (1400 °C) [102]
silicic acid + ANN + urea	1300	tetragonal mullite (980 °C) → orthorhombic mullite [99]

AIP: aluminium isopropoxide (Al(OC₃H₇)₃), ANN: aluminium nitrate nonahydrate (Al(NO₃)₃·9H₂O),

X: mullite type not specified

Mullite processed from mixtures of salts is termed solution-plus-solution [1], see Figure 2.9 (a). Ewell et al. [103] added sodium silicate drop wise to aluminium sulphate followed by the addition of sodium hydroxide for precipitation. The mullite formation was observed by thermal analysis possessing an exothermic peak at 980 °C. Ossaka [104] used sodium silicate and potassium aluminium sulfate $[KAl(SO_4)_2 \cdot 12H_2O]$, and reported crystallized pseudo-tetragonal mullite at 1250 °C after 5 h, found with x-ray diffraction analysis (XRD). Other preparation techniques were carried out with chlorides for both components and an ammonia solution was used to precipitate the components in order to avoid alkali ions included in the mullitization process.

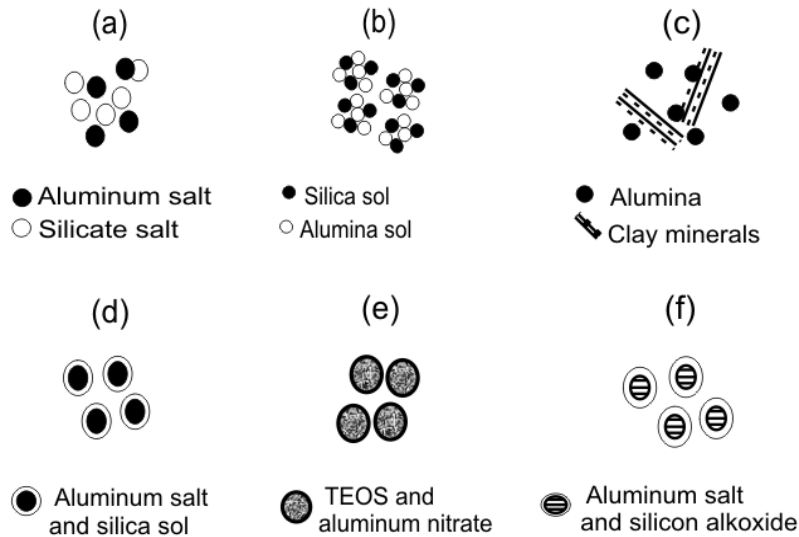
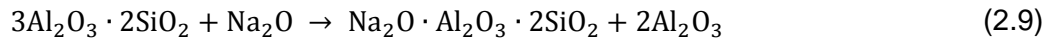


Figure 2.9: Schematic models for mullite starting materials prepared by: (a) Sol mixing (b) hydrolysis of alkoxides (c) mixing of clay minerals and alumina (d) composite particles (e) spray pyrolysis (f) co-precipitation

The sodium oxide as an impurity reacts with mullite above 1200 °C as shown in Eqn. (2.9) and Eqn. (2.10) generating carnegieite ($N_2O \cdot Al_2O_3 \cdot 2SiO_2$) and alumina or may react with cristobalite with the formation of a sodium silicate glass phase [1, 20]. This might improve impermeability of the refractory layers at temperatures below 1200 °C against further infiltration or create internal stresses and expansion at higher temperatures leading to damage of the refractory layer [105].

The use of silicon chlorides had some disadvantages due to its instability and difficulty to control the stoichiometry.

Mazdiyasi et al. [106] used aluminium tris-isopropoxide ($\text{Al}(\text{OC}_3\text{H}_7)_3$) and silicon tetrakis-isopropoxide ($\text{Si}(\text{OC}_3\text{H}_7)_4$) and reported a mullite precursor with extensive mullite formation in the temperature range from 1200 °C to 1700 °C. Aluminium silicate powders were prepared from benzene solutions of aluminium isopropoxide and tetramethyloxysilane (TMOS) with water or aqueous ammonia solutions. Powders prepared with water transform to type I mullite precursors above 980 °C while powders prepared with aqueous ammonia solution transform to type III mullite precursors below 1200 °C [1].

Ismail et al. [107] mixed alumina and silica sols at pH 5-6 where heteroflocculation occurs. They presented a schematic model shown in Figure 2.9, with variations in mixing behaviour with different starting materials. Mullitization started at 1200 °C to 1300 °C. A good chemical homogeneity was reported and it was attributed to molecular mixing of silicon and aluminium alkoxide precursors [95].

Okada et al. [83] dissolved TEOS and aluminium nitrate in ethanol followed by addition of ammonium hydroxide. At neutral pH value alumina nuclei were formed as the inner core with a surrounding silicon-rich shell; see Figure 2.9 (e). They reported a γ -alumina phase at 980 °C and extensive mullitization upon heat treatment at 1115 °C for 24 h.

Mizukami et al. [108] evaluated the effects of ligands and solvents on mullitization using TEOS and aluminium dibutoxide ethylacetoacetate. They observed mullitization in the presence of different ligands and solvents to be improved with intense mixing. A low mullitization temperature is possible with high reactivity to form $\equiv\text{Si}-\text{O}-\text{Al}=\text{}$ bonds when organic ligands were used as starting materials. Nogami et al [109] used TEOS and aluminium isopropoxide, and they reported the importance of water for the formation of $\equiv\text{Si}-\text{O}-\text{Al}=\text{}$ double alkoxide complexes. Monophasic gels synthesized by Voll et al. [92] from TEOS, aluminium sec-butoxide and isopropanol, was studied with FT-IR method. They observed that the water molecules in the pores adhered to the precursor surface and leave by evaporation with organic material at above 400 °C. A high degree of dehydration of the precursor network and the recombination of OH groups to water molecules occur between 600 °C and 700 °C. Part of the recombined water is

entrapped in closed pores. Microfracturing of the precursor due to high vapour pressure enables the evaporation process through the micropores. Above 900 °C, the precursor becomes nearly free of water [7].

Mixtures of sols and salts were reported, termed solution-plus-sol processes for mullite synthesis [110]. Mullite was observed to form composite particles, see Figure 2.9 (d). The precipitation of salt components occurs on the sol particles forming heterogeneous nucleation sites. Mullite synthesized with these methods showed the formation of layered particles [111]. Yoldas [93] observed the formation of $\equiv\text{Si-O-Al}\equiv$ bonds followed by polymerization of aluminium butoxide dispersed in TEOS, mullite was found above 1300 °C. Hoffman et al. [21] used boehmite sol dispersed in alcohol solution of TEOS, reported mullite formation at about 1350 °C. In other studies similar mullitization patterns were found in the temperature range between 1000 °C to 1500 °C [78]. This method allows the processing of mullite matrix composite particles. The mechanism was described as a transient viscous sintering (TVS) mechanism of composite particles. It is shown schematically in Figure 2.10, α -alumina (0.2 μm) particles are coated with SiO_2 layers suspended in ethanol solution containing TEOS. TEOS was hydrolyzed by adding ammoniated water and the silica components precipitates to form composites [111].

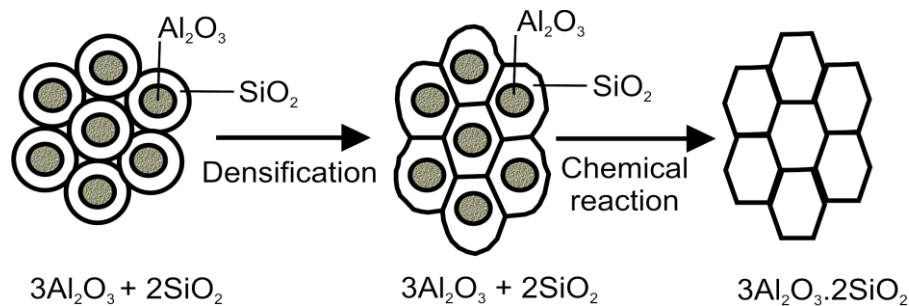


Figure 2.10: Concept of the composite particles formation and the sintering mechanism of mullite composites [111]

They reported viscous amorphous silica layers in the temperature range from 1100 °C to 1300 °C prior to cristobalite formation. Mullitization was observed due to the rearrangement of particles similar to the reaction mechanism for reaction sintering of silica glass and alumina [71]. Extensive mullitization occurred at 1500 °C [111]. The samples remained fully dense after mullitization with a fine-grained microstructure. A slow reaction occurred since an average distance of 0.1 μm was necessary for the diffusion of silicon atoms into α - Al_2O_3 for mullite

formation. Compacted mullite precursors with transiently densified α - Al_2O_3 particles and SiO_2 glass increases the mullite nuclei concentration and showed an increased mullite formation rate [112]. Bartsch et al. [113] produced dense mullite ceramics with processing temperatures as low as 1300 °C using silica coated γ - Al_2O_3 nano-composite particles. This method was also used for processing of mullite-SiC and mullite- ZrO_2 - Al_2O_3 composites [102, 114].

Mullite was also prepared from mixtures of sols described elsewhere as “Sol-plus-sol process”, see Figure 2.9 (b). Starting materials of mixtures of sols with particle sizes from ten to several nanometers were used [1]. Alumina or silica sols were obtained by the dispersion of corresponding precursor materials containing Al and Si ions as main constituents. An adequate pH range of 2 or 9-10 was shown to be appropriate for intimate mixing of alumina and silica sols, where high sol stability was achieved. An increasing pH value in the range of 6 to 7 is reported where hetero-flocculation of alumina and silica particles occurs with diffusion of silica into the alumina structure, studied by XRD measurements [115]. Schneider et al. [94] reported a retarded mullitization with large silica-rich areas at pH values greater than 10. Sols made of γ -alumina and silica were mixed and gelled by solvent evaporation; mullitization occurred at 1450 °C. Other authors found the mullitization temperature to increase up to 1550 °C with sols mixed and heat-treated without gelation, the increased in temperature was linked to segregation of the two components with prolonged mullitization [57, 116].

Diphasic gel precursors of mullite were manufactured by mixing silica and boehmite sols and dispersing in ethanol. DTA analysis revealed a peak at 1250 °C while XRD data indicated the presences of boehmite in the as-prepared gel with mullitization at 1300 °C [21]. Mullitization was also described for diphasic gels in the temperature range from 1200 °C to 1350 °C [1]. For sols, the starting material has a significant influence on the mullitization behaviour. Polymeric precursors transformed to mullite from the amorphous state at about 980 °C, and colloidal gels transform at higher temperatures as shown by DTA, XRD, ^{29}Si and ^{27}Al MAS NMR spectroscopic investigations [78, 88].

Doping of starting materials is a suitable method to reduce the activation energy for the mullitization in mullite precursors by the intensification of the nucleation process. Doping results in the reduction of the viscosity of amorphous silica, promotes higher diffusion rates, accelerates the nucleation and the crystal growth of mullite [70, 52]. Tkalcec et al. [117] used a multi-

component silicate glass and they reported mullitization at 800 °C. The activation energies were below 500 kJ mol⁻¹. For example manganese-doped mullites were synthesized from metal organic materials by a modified sol-gel technique at temperatures ≥ 700 °C [52].

Mullite formation in diphasic gels was reported to possess an activation energy of 1070 kJ mol⁻¹ [118]. The activation energy is significantly higher than in monophasic gels [119]. A diffusion rate-limiting model for mullite formation which occurs either by interface-controlled diffusion or by short-range-diffusion based on molar ratios of precursors was derived. It was later supported by Li and Thomson [61], who found mullitization at approximately 1213 °C to be nucleation rate controlled and becomes diffusion rate controlled above 1400 °C. Sundaresan and Aksay [60] re-examined the aforementioned processes and suggested a dissolution and precipitation mechanism instead of an interface and diffusion controlled process as derived by the aforementioned authors. In their observations, the Al₂O₃ dissolves in the silica phase and mullite nuclei formation occurs when the amorphous aluminosilicate phase exceeds a critical concentration. Mullite nucleation within non-crystalline silica indicates the dissolution of Al₂O₃ as a rate controlled step in the mullite formation. They predicted a dissolution rate controlled process below 1350 °C and a diffusion rate controlled process above 1650 °C with sapphire and silica reactants [51, 73]. Other studies reported nucleation and growth of mullite within siliceous phases. The mullite formation mechanisms at higher temperatures are dominated by chemical diffusion within the mullite grains. The reactions during the primary phase of the mullite formation are controlled by the dissolution of alumina into the siliceous phase followed by a second stage of chemical diffusion controlled by the amount of the alumina phase [61, 120].

Spray pyrolysis

Spray pyrolysis methods with atomization of precursor solutions into droplets driven through a furnace were used for mullite synthesis. Spraying droplets of solutions containing aluminium and silicon species, into a hot chamber includes the evaporation of solvents, the thermal decomposition and the polymerization of the precursors. Rapid reaction processes suppress demixing effects. Homogeneous mullite precursor powders prepared by spray drying from aqueous solution of aluminium nitrate and TEOS transform directly to mullite at 1000 °C. This method is suitable for the preparation of multi-component ceramics; it makes use of spherical shaped mullite powders ranging from submicron to micrometer size, see Figure 2.9 (e). This method makes use of expensive atomizers and ultrasonicators for droplet formation. Other preparation

methods are reported in [1], until Baranwal et al. [121] used flame pyrolysis and observed crystalline mullite to be found at ~900 °C.

Chemical vapour deposition (CVD) method for mullite synthesis

Chemical vapour deposition methods make use of a vapour-phase for mullite formation. It produces mullite powders with little agglomeration, submicrometer-sized primary particles, and regular particle sizes. Silicon chlorides and aluminium chlorides are evaporated and transported to a mixing zone, and sprayed into a heated zone. Nitrogen is the carrier gas. The reactants are heated by a hydrogen-oxygen combustion flame and the temperature is approximately 1900 °C. The temperature gradually decreases through the reaction zone and drops down to approximately 900 °C at the exit. Powders obtained show spherical shape with a particle size of about 40 nm to 70 nm. Mullitization occurred extensively at 1000 °C but complete mullitization requires temperatures to 1500 °C. DTA revealed double exothermic peaks at 1000 °C attributed to meta-stable liquid immiscibility in the $\text{Al}_2\text{O}_3\text{-SiO}_2$ system during cooling [122]. The use of a counter flow diffusion flame burner was exploited, in which fuel (hydrogen and nitrogen), chlorides, and the oxidants flows (oxygen and nitrogen) were mixed and sprayed to the combustion flame. Amorphous spherical powders from 20 nm to 30 nm in size were obtained using a low temperature flame compared to 40 nm to 70 nm in size obtained for high temperature flame [123]. This technique was also used for the deposition of mullite coatings on silicon nitride and silicon carbide substrates. The deposited films were amorphous and crystallized to mullite by sintering at 1100 °C for 2 h [124].

2.5.4 Hydrothermally produced mullite

Mullite sols may also be produced by reactions in an aqueous solution with simultaneous application of heat and pressure. This method provides control of the particle size and morphology by varying the synthesis conditions. Nanostructured powders possess better chemical homogeneity due to a different nucleation and particle growth, and they have a better sinterability at lower temperatures [125]. Somiya et al. [56] produced mullite precursor powders from aluminium isopropoxide and TEOS. The precursors were dissolved in benzene and refluxed for 5 h at 80 °C, followed by hydrolysis and condensation under hydrothermal conditions. The obtained mixtures were washed to remove alcohol and benzene followed by another hydrothermal treatment at 600 °C under a pressure of 20 MPa. The precursors were

calcined and no viable mullite powders were observed. Suzuki et al. [126] examined the phase changes of powders from mixtures of alkoxides or sols hydrothermally treated. They found a spinel phase after firing hydrothermally treated mixtures at 600 °C. Mullitization was observed after firing at 1300 °C for 1 h.

2.5.5 Gel-casting methods for the mullite synthesis

Gel casting of mullite ceramics allows the combination of ceramic processing with polymeric compounds. This involves the dispersion of ceramic precursors into monomeric solutions and casting of the suspension into different forms. This method forms green bodies with improved mechanical strength, allows pore network formation, machinability, by combination with other techniques and to some extent sacrificial template addition [127]. Mullite was manufactured from SiO₂ coated alumina particles with mono-functional methacrylamide (MAM) and difunctional monomers methylene bisacrylamide (MBAM). Mullitization occurred at 1550 °C [128].

According to the sol-gel processing mechanisms, the above reactants are converted to a sol either by adjusting the pH values which causes flocculation or to evaporate the solvent and concentrate the sol to transform it into a gel. Heat application led to the transformation from the amorphous state via a spinel-phase to crystalline mullite. Polymeric gels were observed to transform above 980 °C to mullite while the mullitization temperatures of colloidal gels change to about 1200 °C and is accomplished in the temperature range from 1350 °C to 1500 °C. The reduction of the particle size and intimate mixing in the sol-gel system reduced the mullitization temperatures, and different microstructures and properties were reported [1, 3].

2.6 Properties and applications of mullite

The applications of mullite ceramics are influenced by different factors such as grain boundaries, glass phase amount, grain size, density and porosity [5, 8]. Recent studies discussed in [53] have developed the relationship between mullite properties and the aforementioned factors. The mechanical (Table 2.5) and thermal (Table 2.6) properties of mullite are controlled by the mentioned factors. These properties vary according to the different gel precursor types used for sol-gel mullite processing as listed in Table 2.3, generating dense and porous mullite types. Dense and compact mullite materials possess high flexural strength. Porous mullite shows a

reasonably strength combined with low thermal expansion suitable for thermal shock stability [3, 129, 130].

A complete densification of gels leads to mullite with a homogeneous microstructure, which improved the optical and the mechanical properties. It has been shown that an earlier formation of mullite retards the densification process. Complete densification prior to mullitization might be the best method to achieved mullite with no segregated phases. Monophasic gels crystallized at lowered temperatures compared to diphasic gels. The densification is more difficult in monophasic gels, and segregated phases may form which influence the optical and the mechanical properties of processed mullite ceramics [82, 131, 132]. Though, mullite crystallized from completely densified gels is required for excellent mechanical properties, but mullite ceramics with some porosity have outstanding properties for high temperature catalysis and separation applications. Porosity in mullite leads to a reduction of the thermal expansion coefficient [133, 134]. Mullite properties derived from different gel precursors containing TEOS as a silica source and different alumina precursors were evaluated see Table 2.4. Mullite prepared from aluminium nitrate nonahydrate had a higher strength, higher Vickers hardness and lower fracture toughness compared to the other compositions [135].

Table 2.4: Properties of sol-gel mullites derived from different starting materials [135]

Property	TEOS + ANN	TEOS + γ -Al ₃ O ₃	TEOS + boehmite
grain distribution	bimodal	monomodal	monomodal
average grain size [μm]	5-7	0.6	1.3
HV [GPa]	13.5 \pm 0.2	12.5 \pm 0.2	12.9 \pm 0.2
K _{ic} [MPa m ^{0.5}]	1.7 \pm 0.1	1.9 \pm 0.2	1.9 \pm 0.2
σ [MPa]	261	204	246
Weibull parameter [m]	13.6	12.1	4.4

where HV: Vickers hardness, K_{ic},: fracture toughness, σ : flexural strength

Mullite material properties with respect to other investigations are reported, see Table 2.5. The variations in the properties are linked to the starting materials and synthesis method discussed in [1, 3]. Additionally, higher values of the listed properties in Table 2.5 were obtained from dense mullite (approximately 95 % dense) while lower values are obtained from porous mullite [5].

Kanzaki et al. [136] published a flexural strength of 360 MPa from spray pyrolysis-derived alkoxides at room temperature. Others reported at same temperature a higher flexural strength being in the range of 400 MPa to 500 MPa, starting from commercial high purity sol-gel mullite materials [137, 138].

A tendency of increasing strength and fracture toughness with the decrease of porosity was observed. Flexural strength for mullite ceramics were reported to decrease from 500 MPa to 100 MPa corresponding to an increase in porosity from 1 % to 15 %. The fracture toughness was observed to decrease from 3 MPa m^{0.5} to 1 MPa m^{0.5} in the given porosity range, and details are given in [139, 140, 141]

The alumina content in mullite ceramics is reported to influence the mechanical properties. Strength values vary according to different mol.-% of alumina. The flexural strength changes from 150 MPa to 250 MPa at 46 mol.-% alumina, increases from 350 MPa to 450 MPa between 54 mol.-% alumina and 61 mol.-% alumina, and slightly decreases from 250 MPa to 350 MPa at 67 mol.-% alumina [142, 143].

Table 2.5: Mullite mechanical properties (at room temperature)

Properties	Measured values	Ref.
density, [g cm ⁻³]	3.16-3.22	[1]
microhardness, [GPa]	5-10	[144]
fracture toughness, [MPa m ^{0.5}]	2.8-3.0	[3]
Young's Modulus, [GPa]	25-250	[40]
poisson's ratio, ν	0.20	[40]
flexural strength, [MPa]	150-360	[1]

Kumazawa et al. [145] used 55 mol.-% and 60 mol.-% alumina and they observed a flexural strength maximum at high temperatures in the range of 1200 °C to 1300 °C. Mullite was processed by liquid-phase sintering and owing to its high silica content, the high temperature strength increase is explained by stress relaxation and/or crack healing caused by softening of the glass phase at the grain boundaries. Others reported no distinct maximum with hot-pressed mullite ceramics containing 60 mol.-%, 61 mol.-%, and 65 mol.-% of Al₂O₃, but a slight decrease in strength between 1200 °C and 1300 °C. These materials were observed to constitute of

equiaxed mullite grains with a small content of a glass phase located at triple points of mullite grains, but not at the grain boundaries as compared to the latter systems [138].

Mullite ceramics are also found to have differences in its thermal properties, see Table 2.6. Their thermal conductivity values range from $5 \text{ W m}^{-1} \text{ K}^{-1}$ to $7 \text{ W m}^{-1} \text{ K}^{-1}$ at room temperature for different materials and synthetic routes [146, 147]. These values and also these differences are comparatively small which made mullite ceramics useful for thermal insulation applications [148]. In comparison: α -alumina possesses a thermal conductivity of $40 \text{ W m}^{-1} \text{ K}^{-1}$ and silica of $7 \text{ W m}^{-1} \text{ K}^{-1}$ [149]. A high thermal conductivity for α -alumina is associated to its crystallographic arrangement [134]. The thermal conductivity (see, Table 2.6) values for mullite are almost independent on a temperature of up to $800 \text{ }^\circ\text{C}$, and rapidly decrease from $6 \text{ W m}^{-1} \text{ K}^{-1}$ to $3.9 \text{ W m}^{-1} \text{ K}^{-1}$, when the temperature reaches $1000 \text{ }^\circ\text{C}$ [148].

The linear thermal expansion coefficient of mullite ranges from $4.5 \cdot 10^{-6} \text{ K}^{-1}$ to $6 \cdot 10^{-6} \text{ K}^{-1}$ within the temperature range from $20 \text{ }^\circ\text{C}$ to $1000 \text{ }^\circ\text{C}$ [150]. Mullite has a relatively low value compared to α -alumina (i.e. $5.4 \cdot 10^{-6} \text{ K}^{-1}$ to $9.5 \cdot 10^{-6} \text{ K}^{-1}$) [37, 149]. Thermal expansion data of mullite give information on its shape stability and temperature induced strain. The differences in thermal expansion are attributed to the influence of grain boundary phases, pores, and thermal stress, details are given in [53]; for more details see Appendix 1. Thus, mullite ceramics possess low thermal expansion coefficients, a low thermal conductivity [146], low creep resistance [151], good chemical and thermal stability [25], and a good mechanical strength [136]. Another important property of mullite ceramics is their very good resistance to fast temperature changes, due to their low thermal expansion coefficient [152, 153].

Table 2.6: Thermal properties of mullite

Properties	Temp. [$^\circ\text{C}$]	Values	Ref.
thermal conductivity (λ), [$\text{W m}^{-1} \text{ K}^{-1}$]	20-1400	6-3	[53]
	100-1400	6.1-3.9	[154]
thermal expansion coefficient (α), $\cdot 10^{-6}$, [K^{-1}]	300-1400	3.1-7.5	[149]
	20-1000	4-6	[40]
heat capacity (C_p), [$\text{J g}^{-1} \text{ K}^{-1}$]	25-1000	0.76-1.26	[40]

Mullite is used in steel manufacturing as furnace lining material (e.g. mullite based bricks are used in lining the upper parts of melting furnaces, hot blast stoves, continuous casting furnaces, torpedo ladles, etc), due to its low thermal conductivity and coefficient of thermal expansion [146]. Recent research reported an $\text{Al}_2\text{O}_3\text{:SiO}_2$ molar ratio of 9:1 from sol-gel derived mullite being used as refractory material due to its high alumina content [16]. Mullite shows enhanced spalling resistance and stability under load at high temperature, while alumina has a good influence on the corrosion resistance and mechanical properties [155]. The steel industry is the largest consumer of the aforementioned mullite-based refractories [156]. Data on the chemical corrosion resistance of mullite ceramics against solutions, melts, slag and gases is given in Appendix 2 [1]. Mullite presents a good stability in the presence of molten salts and slags similar to $\alpha\text{-Al}_2\text{O}_3$. But its resistance against molten metal is low. However, its corrosion resistance in gases and its gas impermeability is excellent. This makes mullite suitable for lining upper parts of furnaces [157, 158].

Mullite coatings are applied as barriers to separate materials from harsh environment at elevated temperatures. Mullite coatings are deposited on different substrates including: SiC, Si_3N_4 , mullite and Al_2O_3 [159]. This improves the resistance to corrosion, heat and wear of components. For example: Mullite coatings are used in protecting silicon-based ceramics and as composites in hot areas in gas turbines and heat exchangers. This is connected to its corrosion resistance, creep resistance, high temperature strength, good fracture toughness, and its low CTE which matches silicon-based ceramics. Mullite coatings have shown to be most promising for SiC substrates because their thermal expansion coefficients are similar [160]. Mullite coatings are also used as hard and abrasion resistance coatings for spacecraft applications as shields of re-entry space vehicles [161]. Different techniques are explored to deposit these coatings, including: Chemical vapour deposition (CVD), plasma and flame spraying, and physical vapour deposition (PVD) [1].

Mullite is used as material for heat exchangers due to its high temperature stability, especially due to its thermal shock resistance, good oxidation resistance, good corrosion resistance, and suitable thermo-mechanical properties. However, in terms of thermal conductivity it is not an optimal material. Since high thermal shock resistance is an inherent property, mullite ceramics with low thermal expansion coefficients are used. Heat exchange efficiencies are observed to increase with increasing temperature, and they are used in technical systems to save exhaust

energy and serve in heat recovery systems. Spherical particles of mullite between 0.5 mm to 2 mm are used for heat regenerating processes at temperatures between 1300 °C and 1400 °C, which extend the working temperatures of heat regenerating systems [1, 162].

Another application is in particle filtration and catalyst support in exhaust gas in cleaning systems, as exhaust port liners for diesel engines, as gas filter supports for combustion furnaces such as in incinerator and electric power generation plants; and as filters in breweries or wastewater disposal plants [163]. Mullite-cordierite honeycombs are used instead of pure cordierite in diesel particulate traps due to a low corrosion resistance of cordierite. Mullite honeycombs for diesel particulate traps and semi-closed-cell mullite foams were made using corrugation method and replication processes, respectively [164]. However, some reports predict that mullites used in exhaust gas systems in diesel vehicle filters are stable in the presence of CaO, ZnO and V₂O₅, but it is attack by Na₂O and PbO [165].

More applications may be found as substrate material with high density for electronic device packaging. The mullite's thermal expansion is close to that of silicon and mullite has a relatively low dielectric constant; both properties are crucial to minimized stress generated mismatches in silicon chips, in packaging materials, and to reduce the signal delay time of the electronic circuits [166, 167].

Mullite and mullite-glass ceramics are used in optical applications, mainly as window material for the mid-infrared wavelength range from 3 μm to 5 μm and in the visible range, under harsh conditions, high temperatures and mechanically stressful environments. The addition of Cr³⁺ ions showed luminescence behaviour in mullite glass ceramics [168]. These properties are attributed to the optically translucent character in the visible spectral range, its defect structure, and its low dielectric constant ($\epsilon = 7.0$ MHz) [169, 170].

Mullite components have been applied for brake linings and ceramic guides. Cermets containing mullite are also used for aircraft and rapid transit railway brake linings, generating high friction resistance. Brake linings were manufactured from a composite containing copper-tin or copper-iron alloy as matrices with mullite as dispersion phase, for an enhancement of the friction resistance. Mullite containing cermets showed good long term heat resistance and are suitable for applications as clutch facings for automobiles [171].

Mullite fibers are used as thermal and heat insulating materials for kiln furnaces, as heat resistant fillers, as substrates for catalysts, as heat resistant packaging for car engines, as fillers and reinforcing materials for composites, due to its low thermal conductivity, good heat resistance and insulating properties. The reinforcement of mullite matrices with continuous chopped fibers, whiskers, platelets and particles generate mullite composites with an increase in mechanical properties [114, 172].

Metal-reinforced mullite matrix composites designated as Me/mullite (e.g. aluminium/mullite, Molybdenum/mullite,) are used as innovative materials for metal filters, catalyst supports, radiant burners and sensors. Molybdenum/mullite composites with small differences in their thermal expansion coefficients (molybdenum; $\alpha \approx 5.8 * 10^{-6} \text{ K}^{-1}$; mullite; $\alpha \approx 5.5 * 10^{-6} \text{ K}^{-1}$) are used as insulator elements and thermal barrier coatings. These combinations hindered crack growth and reduces stress intensity at crack tips by bridging of the ductile metal grains [173, 174].

Despite the mentioned advantages, plain mullite presents some limitations due to its low fracture toughness, which do not fulfil some of the needs for the applications reported above. It was found that some of the aforementioned properties constitute mullite with some additional components linked to its limitations. Its ability to sustain continuous thermal, chemical and mechanical activities reduces as it is exposed to continuous residual stresses [8, 155, 156]. Different approaches are focus on the manufacturing of reinforced mullite. A short review is given in the following section dealing with mullite composites.

2.7 Mullite composite materials

In the aforementioned sections, plain mullite used for diverse applications, however, exhibits comparatively low mechanical stability, especially under cyclic and permanent mechanical load. In order to improve the mechanical stability, a composite materials concept has been developed [179-188]. One of the concepts makes use of reinforcement phases such as Al_2O_3 , SiC, Si_3N_4 and ZrO_2 [175]. This is achieved by shielding crack tips and/or generating new phases with mechanisms for reducing failure which develops during rapid thermal changes. Such composites form a continuous ceramic matrix with included reinforcement particles of different sizes and some residual porosity. The addition of alumina to mullite generates a mullite-alumina matrix with an improved corrosion resistance and enhanced mechanical properties [176]. This is

enabled by the material properties of alumina (see, Table 2.1) and mullite (see Table 2.6). A combination of the alumina and the mullite properties is reported to enhance strength, spalling resistance, stability and thermal shock resistance of refractory materials [177, 178]. The use of α - Al_2O_3 has a positive influence on corrosion resistance and mechanical properties [179, 180]. A high load of fine alumina particles into mullite results in a reduction in shrinkage of approximately 10 % [181]. The addition of polycrystalline coarse-grained spherical alumina particles caused an increase in fracture toughness. These authors suggest that extra toughening arise from elastic bridging ligaments in the matrix that appears to be triggered by the alumina grains [140, 176, 182].

Medvedovski et al. [180] produced corundum-mullite from the system Al_2O_3 - SiO_2 with additions of earth-alkali silicates or borosilicates as sintering aids. They reported a crystalline phase of alumino-silicate and alumino-borosilicate uniformly bonded by a glassy phase. Different properties were obtained: strength (300 MPa to 350 MPa), thermal shock temperature difference (ΔT : 181 K to 215 K), thermal shock sensitivity of the material parameters (R_s : 1.40 kW m^{-1} to 1.56 kW m^{-1}) and a coefficient of thermal expansion with a value of $5.5 \cdot 10^{-6} \text{ K}^{-1}$ [181, 183]. Corundum-mullite was also manufactured by in-situ decomposition of pore formers. Mixtures of milled $\text{Al}(\text{OH})_3$ and micro-silica were compacted and heat treated to 1600 °C for 3 h, and corundum-mullite composites containing 42.3 % porosity were obtained [140, 179].

The role of alumina and mullite particles to improve the material properties of slip-cast alumina-mullite composites were investigated in [143]. A porosity of 19 % (75 mol.-% alumina + 20 mol.-% mullite + 5 mol.-% clay) and 26 % (55 mol.-% alumina + 40 mol.-% mullite + 5 mol.-% clay) were reported. Flexural strength values of ~17 MPa were obtained for a porosity of 19 % and ~10 MPa for 26 % porosity. The strength values were found to decrease with increasing porosity. The samples showed a critical thermal shock temperature difference of $115.2 \text{ K} \pm 15.7 \text{ K}$ compared to $105.2 \text{ K} \pm 14.0 \text{ K}$ for the later sample. The addition of fine alumina particles showed an improvement in flexural strength and the Young's modulus with an increase in the quenching temperature. This indicated a better thermal shock resistance [141, 184, 185].

Tang et al. [186] described a heterogeneous nucleation process using a core (Aluminium hydroxide)-shell (silica) approach in an ethanol solution containing ammonia. Mullite particle (0.67 μm) formation occurred at 1500 °C after 2 h. Wang et al. [187] reported a silica coating

layer on ultrafine α -alumina particles with the sol-gel method. They observed a thin and less dense surface of an amorphous silica layer of ~ 20 nm by means of transition electron microscopy [188].

In ongoing investigations the material properties were further improved by introducing residual stresses during fabrication. This was realized by the introduction of a secondary phase such as mullite at the surface of alumina component by infiltration processes [9-12]. In this approach, the alumina particles are immersed into mixtures containing silica precursors, and upon sintering silica is formed which reacts with the outer regions of the alumina particles to form mullite at the surface of the alumina grains. Upon cooling the unmodified alumina core contracts more than the outer surface shell. Formed mullite on the surface gains its stability from created pores. Pores provided stability during thermal expansion and contraction of the alumina- mullite core-shell composite [189].

Marple et al [9, 12] reported core-shell alumina-mullite formation prepared with infiltration technique and they presented some microstructural and mechanical properties. Alumina-mullite composites were prepared from porous alumina bodies and TEOS infiltrated through the open porosity. The mixture was fired to a dense material consisting of mullite in the surface parts and alumina in the inner parts. These composites showed enhancement of the fracture toughness to approximately $7 \text{ MPa m}^{0.5}$ in alumina-mullite core-shell composites compared to $4 \text{ MPa m}^{0.5}$ in plain mullite [12]. The mullite phase generates compressive stress on the surface of alumina with a decrease in elastic modulus as compared to alumina. The fracture toughness of alumina-mullite composites produced from hydrolyzed ethyl silicate sol which was infiltrated as SiO_2 source into porous alumina sample is also reported. The fracture toughness was measured to be increased from $3.9 \text{ MPa m}^{0.5}$ to $\sim 5.8 \text{ MPa m}^{0.5}$ as the amount of alumina increased, shown in Table 2.7 [10].

Taktak et al [11] used the same technique with cylindrical alumina compacts which were manufactured by uniaxial pressing at 150 MPa. The microstructure and coefficient of friction as a function of applied load for the different alumina-mullite composites was investigated. None of these authors investigated the relationship between the microstructure, the thermal properties and thermal shock behaviour of the core-shell alumina-mullite composites.

Table 2.7: Fracture Toughness for alumina-mullite prepared from infiltration technique [10]

Sample	Phases detected by XRD	Mullite [vol.-%]	Fracture toughness [MPa.m^{-0.5}]
A	alumina	0	3.9±0.1
B	alumina + mullite	5.78±0.326	4.3±0.1
C	alumina + mullite	8.32±0.46	4.8±0.5
D	alumina + mullite	10.83±0.3.7	5.8±0.2

As a consequence of the work discussed above, alumina might be a good component to improve the material properties of mullite. It was stated, that the alumina's mechanical and thermal properties might improve the mullite properties when used as a reinforcement phase. A few studies were carried out on core-shell alumina-mullite composites prepared with infiltration methods. Comparing the microstructure, mechanical and frictional properties of the core-shell alumina-mullite in the aforementioned sections, little results exist with some evidence for core-shell formation in mullite ceramics.

It is the intension of this study to evaluate the microstructure, mechanical, thermal properties, and the thermal shock behaviour of alumina-mullite ceramic materials processed from a non-balanced SiO₂:Al₂O₃ sol-gel method.

3 Experimental

3.1 Starting materials

Two different silica precursor sources were investigated. A model route consisting of tetraethyl orthosilicate plus alumina, and a technical relevant system made of colloidal silica plus alumina powder were processed and compared. The silica precursor of the model route was practically free of alkali ions. The sodium ion concentration in the colloidal silica was initially high. It was reduced by ion exchange.

a) The model system: tetraethyl orthosilicate route (TEOS)

In the TEOS route the different samples were manufactured using tetraethyl orthosilicate (TEOS, 99 %, ABCR GmbH & Co.KG, Karlsruhe, Germany) as the silica source, ethanol (C₂H₅OH, Carl Roth GmbH & Co.KG, Karlsruhe, Germany) as solvent, alumina particles (CT3000SG, 99.8 %, Almatis GmbH, Frankfurt, Germany) as an alumina source and distilled water. Typical characteristics of CT3000SG are given in Appendix 3 and Appendix 4. Acetic acid (CH₃COOH, Carl Roth GmbH & Co.KG, Karlsruhe, Germany) was used as a gelation catalyst for the promotion of the hydrolysis and the condensation of TEOS. The sol-gel process was carried out as described in [7, 87].

Sample compositions containing silica-to-alumina molar ratios of 1:3.4 (23 mol.-% SiO₂:77 mol.-% Al₂O₃) and 3.4:1 (77 mol.-% SiO₂:23 mol.-% Al₂O₃) were calculated as shown in Table 3.1 and details are given in Appendix 5 and Appendix 6.

Table 3.1: Molar ratio of precursors and ratio of SiO₂:Al₂O₃ derived for the TEOS route

TEOS	Ethanol	Water	SiO ₂ :Al ₂ O ₃	Sample composition	Denoted as
0.1	0.1	0.2	1:3.4	23 mol.-% SiO ₂ :77 mol.-% Al ₂ O ₃	TEOS-23
0.3	0.4	0.6	3.4:1	77 mol.-% SiO ₂ :23 mol.-% Al ₂ O ₃	TEOS-77

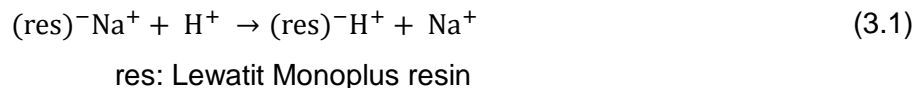
The derived ratios correspond to a deficit of silica (23 mol.-% SiO₂:77 mol.-% Al₂O₃) and a surplus of silica (77 mol.-% SiO₂:23 mol.-% Al₂O₃), respectively, in the case of complete reactions (see, Figure 2.1). The calculated SiO₂:Al₂O₃ molar ratios for the TEOS route are denoted as TEOS-23 for the former sample and TEOS-77 for the latter sample. The 23 and 77

represent the amount of silica in mol.-%, and the balance is the derived mole percent of alumina shown in Table 3.1.

b) The technical relevant system: colloidal silica (CS)

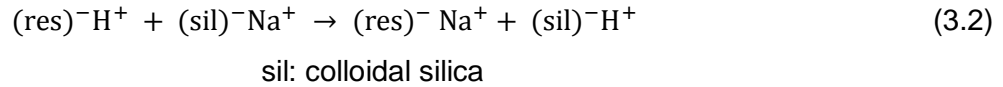
The colloidal silica (Köstrosol 3550, CS, Chemiewerk Bad Köstritz GmbH, Bad Köstritz, Germany) used in these experiments contains 50 wt.-% silica with an alkali ion content of 0.25 wt.-% sodium ions. Other characteristics of the CS are given in Appendix 7. Sodium ions in mullite materials are reported to reduce the melting temperature. In addition, impurities have the tendency to segregate to grain boundaries in sintered materials and form secondary phases with varying properties. In order to avoid the incorporation of sodium ions into the mixture and thus into the ceramic material, the silica sol was ion exchanged to remove the sodium ions [70]. The ion exchanged was carried out using Lewatit Mono Plus S 108 resin (Kurt Obermeier GmbH & Co.KG, Bad Berleburg, Germany). The Na⁺ ion concentration of the exchanged sol was measured with an atomic absorption spectrometer (AAS, Aurora Biomed Inc. Vancouver, Canada) [190].

Lewatit Mono Plus is a macro-porous styrene-divinylbenzene copolymer, and its properties are listed in Appendix 8. It was supplied in the sodium form with beads of a uniform size, and needed to be transformed into the acidic form prior to the exchange process with CS. For the ion exchange and activation of the exchanged resin, 200 ml of 7 vol.-% HCL solution was poured into a glass beaker containing 150 g of the Lewatit Monoplus resin. The mixture was stirred and allowed for a contact time of 3 h. The Lewatit Monoplus resin ion exchange is described in Eqn. (3.1). Subsequently after the prolong exchange of the lewatit resin, the silica sol was ion exchanged with lewatit resin to reduce its content of sodium ions.



For the exchange of Na⁺ ions from the CS, 150 g of the obtained activated lewatit resin was transferred into 600 ml polypropylene beaker followed by addition of 100 ml of CS. The mixture was continuously stirred for 3 h to achieve the ion exchange according to Eqn. (3.2). The mixture was then filtered using a Buchner funnel and an Erlenmeyer flask attached to a vacuum pump.

The mixture of the CS and resin was poured into the Buchner funnel. The CS was sucked into the flask under differential pressure created by a vacuum pump.



The colloidal silica was dried at 105 °C for 15 hours and fired in a Carbolite high temperature furnace (Carbolite GmbH, Ubstadt-Weiher, Germany) at a heating rate of 10 K min⁻¹ to 1000 °C. From the as-fired CS, approximately 0.052 g of CS was ground and mixed with 0.25 g of lithium borate (LiBO₂) [191]. The mixture was ignited in a muffle furnace (Thermoconcept GmbH & Co.KG, Bremen, Germany) for 30 minutes at 900 °C, with air. The sample obtained at 900 °C was dissolved into a glass beaker containing 20 ml of concentrated nitric acid solution. The mixture was stirred magnetically for 1 h in order to enable complete dissolution in the nitric acid solution. The resultant solution was analyzed with AAS for its Na⁺ ion content. The dilution factors are listed in Table 3.2.

Table 3.2: AAS analysis of Na⁺ ions in CS

Sample	Dilution factor	Na [mg l ⁻¹]
CS without ion exchange	1:100	9.90
CS ion exchange with Lewatit Monoplus S 108 resin (once)	1:150	6.25
CS ion exchange with Lewatit Monoplus S 108 resin (four times)	1:25	1.78

The freshly ion-exchanged CS solution was used as a silica source. Colloidal processing as described in [79, 81], was carried out. Ethanol, distilled water, acetic acid and alumina particles were added as discussed in section 3.1, details are listed in Table 3.3.

Table 3.3: Molar ratio of precursors and ratio of SiO₂:Al₂O₃ derived for the CS route

CS	Ethanol	Water	SiO ₂ :Al ₂ O ₃	Sample composition	Denoted as
0.3	0.2	0.3	1:3.4	23 mol.-% SiO ₂ :77 mol.-% Al ₂ O ₃	CS-23
0.5	0.3	0.5	2:3	40 mol.-% SiO ₂ :60 mol.-% Al ₂ O ₃	CS-40

Sample compositions containing a silica-to-alumina molar ratio of 1:3.4 (23 mol.-% SiO₂:77 mol.-% Al₂O₃) and 2:3 (40 mol.-% SiO₂:60 mol.-% Al₂O₃) were calculated for the CS route as shown in Appendix 9 and Appendix 10. The calculated SiO₂:Al₂O₃ molar ratio for the CS route is denoted as CS-23 for the former sample and CS-40 for the latter sample. The 23 and 40 represent the amount of silica in mol.-%, and the remaining difference correspond to the derived mole percent of alumina, see Table 3.3.

The derived molar ratio of silica-to-alumina of 1:3.4 in the CS route is a surplus of alumina compared to silica, same as the molar ratio determined for the TEOS-23 sample. An alumina-to-silica molar ratio of 2:3 determined for the CS route corresponds to the mullite composition. Mullite compositions range from 59 mol.-% to 66.5 mol.-% alumina resulting in a molar composition from 3Al₂O₃-2SiO₂ to 2Al₂O₃-1SiO₂ [1].

3.2 Material processing

3.2.1 Mixing of the starting materials

The calculated amount for the TEOS and CS routes were mixed with alumina according to the schematic procedure in Figure 3.1. In the processing, silica precursors of TEOS (see Table 3.1) or CS (see Table 3.3) were added to ethanol under magnetic stirring (Bibby Scientific SAS, Nemours Cedex, France) and intimately mixed for 30 min. Distilled water was slowly added for hydrolysis. The pH value of the suspension was adjusted to 6 by drop wise addition of acetic acid while heating at 45 °C (1 h). The amount of catalyst was carefully optimized for the different compositions to give the suspension a tailored viscosity for casting. A pH of 6 was determined for both routes to be optimal. At these conditions, a homogeneous system was obtained suitable for mixing with alumina particles showing no sedimentation effects, see also [75, 84].

Alumina powder was dispersed into this system and ball mixed (with Si₃N₄ balls having diameters of 5, 10, 15 or 20 mm) with an overhead mixer for 6 h (Heidolph Instruments GmbH & Co.KG, Schwabach, Germany). This was followed by a homogenization/deaeration over 30 min with a planetary centrifugal mixer ARE-250 at a rotational speed of 2000 rpm (Thinky Corporation, Tokyo, Japan). This process allowed proper mixing and degassing simultaneously. The liquid phase served a double function: as transportation medium in the liquid-state for the Al₂O₃ particles during casting and shaping, and as a silica source after a liquid-solid

transformation during gelation. The suspensions were characterized with respect to their rheological behaviour prior to casting.

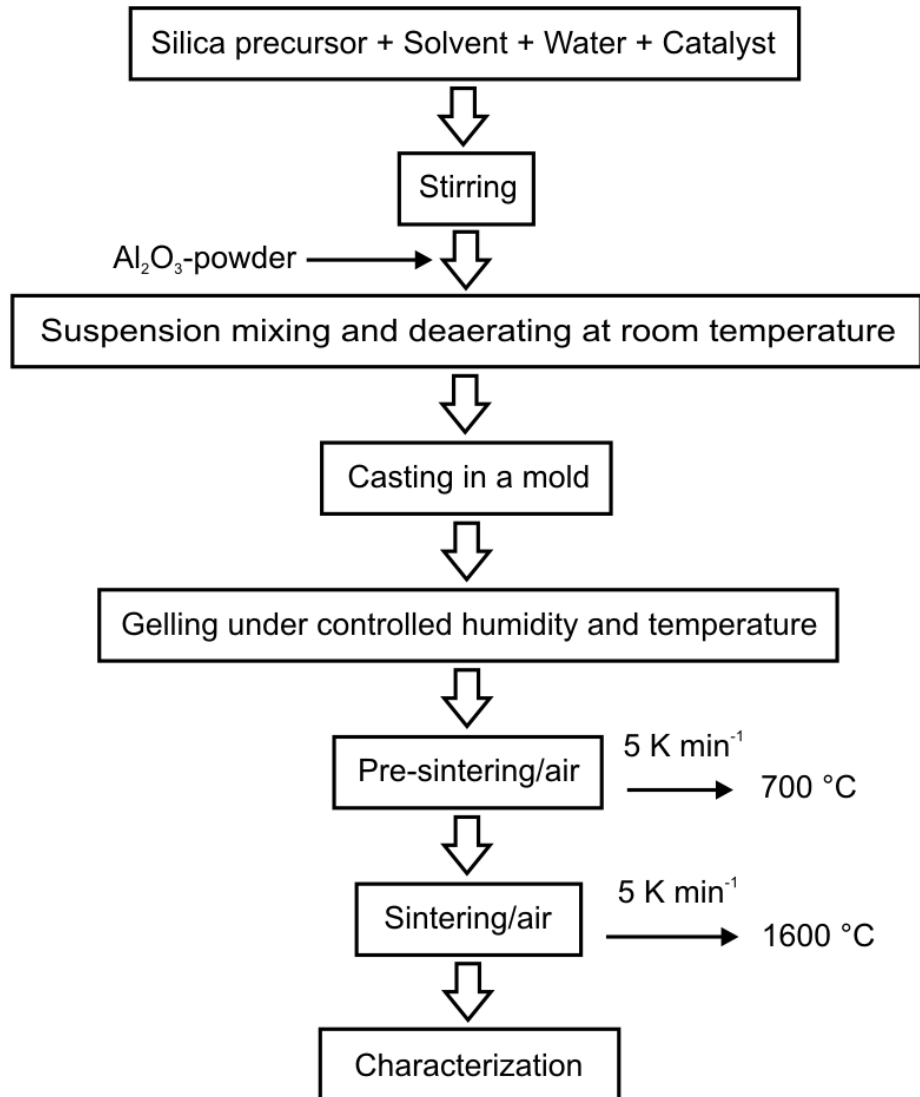


Figure 3.1: Processing scheme

3.2.2 Rheological characterization of the suspensions

The rheological properties of the suspensions were characterized using a rheometer with a concentric cylinder (MCR 301, Anton Paar GmbH, Ostfildern, Germany). Approximately 15 ml of the suspension were poured into the gap between an inner rotary cylinder and an outer stationary cylinder at 25 °C, where the viscosity was measured as a function of the shear rate. A

shear thinning behaviour in which the viscosity decreases with increasing shear rate allows for optimal casting conditions. The viscosity of the suspensions was measured at different pH values. From [95] it is known that, a pH value of 6 is optimal, no sedimentation occurs at pH values ranging from 5 to 7. Direct observation of the different suspensions upon standing at room temperature showed no sedimentation effects. This was also confirmed by viscosity measurements.

3.2.3 Shaping of molds and casting of suspensions

For the casting of the suspensions, polytetrafluoroethylene (PTFE; Teflon[®]) rods and plates (RS Components GmbH, Mörfelden-Walldorf, Germany) were cut, machined and polished into different forms with a Universal lathe DM.1000 A (KNUTH Werkzeugmaschinen GmbH, Wasbek, Germany). The molds are shown in Figure 3.2, isopropanol was used as a mold release agent.

The suspensions were poured into the Teflon[®] molds at room temperature and dried at 85 % relative humidity for approximately four to six weeks. The TEOS-23 and CS-23 samples were dried for one month; 5 weeks was the drying time for the CS-40 sample and six weeks for the TEOS-77 sample. Green compacts were carefully de-molded at room temperature, and they were wet, porous and fragile. Compacts processed with 77 mol.-% Al₂O₃ (TEOS-23 or CS-23) showed a higher green strength and a good de-molding behaviour compared to compacts prepared with 60 mol.-% Al₂O₃ (CS-40) and 23 mol.-% Al₂O₃ (TEOS-77).

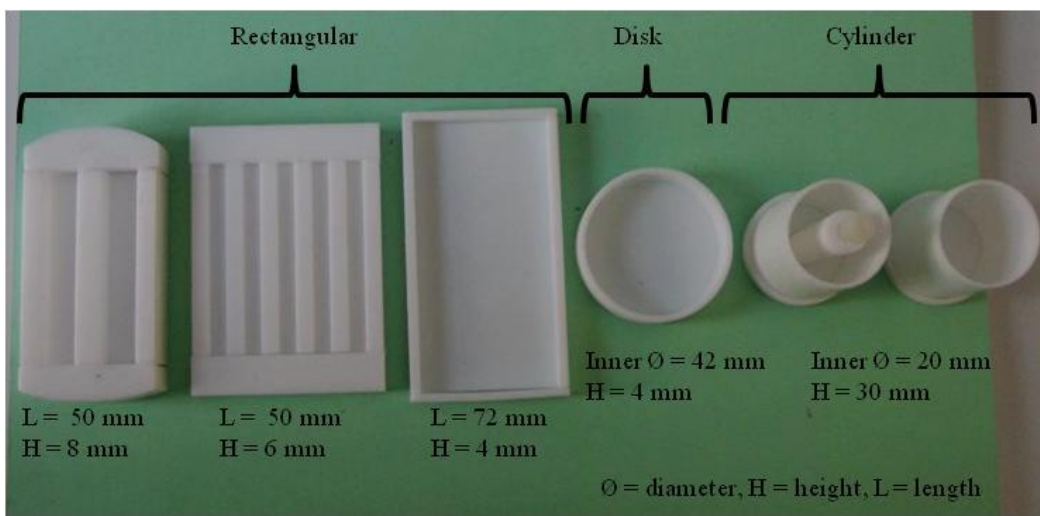


Figure 3.2: Teflon molds for slip casting of the SiO₂-Al₂O₃ sol-gel systems

3.2.4 Thermal treatment of green samples

The heat treatment includes drying of the green samples and sintering. In the drying process, water and solvents were removed off the samples in a laboratory oven (Binder GmbH, Tuttlingen, Germany) in the temperature range from 50 °C to 200 °C. A heating rate of 4 K min⁻¹ and a holding time of 5 h were applied up to the maximum temperature. The dried samples were calcined at a rate of 5 K min⁻¹ to 700 °C in a furnace following a holding time of 3 h.

Samples pre-sintered at 700 °C were partially machined into various forms and heat treated at a rate of 5 K min⁻¹ to 1000 °C with a holding time of 2 h, since fully sintered samples to higher temperatures present some difficulties during shaping and machining. Sintering was performed in a high temperature furnace (Carbolite GmbH, Ubstadt-Weiher, Germany) in a temperature range from 1100 °C to 1600 °C with holding times of 3 h and 12 h at peak temperature. Different heating rates (5 K min⁻¹) and cooling rates (3 K min⁻¹) were applied. The as-fired samples were either mortared or machined into the various shapes for further characterization. Cylindrical blocks were drilled to hollow cylinders (length = 15mm, inner Ø = 8 mm, outer Ø = 12 mm) with a Universal Lathe DM.1000 A (KNUTH Werkzeugmaschinen GmbH, Wasbek, Germany). Shaped samples were cut and polished.

3.3 Microstructure and property analysis

3.3.1 XRD, SEM and TEM analysis

The changes in microstructure and morphology during pyrolysis were studied with X-ray diffraction analysis (XRD) in combination with Rietveld refinement, and scanning electron microscopy (SEM) and transmission electron microscopy (TEM).

XRD gives information on the crystalline phase composition in materials, lattice parameters and crystallite size. The diffraction patterns of X-rays at crystallographic planes is described according to Bragg's law shown in Eqn. (3.3). These are related to distances between atomic planes in the crystal lattice (d_{hkl}), scattering angle ($2\theta_{hkl}$) and the wavelength of the incident beam (λ).

$$n\lambda = 2d_{hkl} \sin\theta \quad (3.3)$$

where n = order of the reflection, λ = wavelength, d = lattice space, hkl = Miller indices, θ = scattering angle

XRD studies of the ground powders were performed with an X'Pert Pro diffractometer (PANalytical GmbH, Almelo, Netherlands) with $\text{CuK}\alpha$ radiation (wavelength: $\lambda_{\alpha_1} = 1.54060$, $\lambda_{\alpha_2} = 1.54443$). A voltage of 40 kV was applied. Data were collected in steps of 0.017° in the 2θ angle measuring setup ranging from 10° to 140° . A least-square fit of the background was subtracted from the diffraction patterns, and the HighScore Plus software package (PANalytical GmbH, Almelo, Netherlands) was used to quantify the phase amount.

Scanning electron microscopy (SEM, Philips XL30 ESEM, Eindhoven, Netherlands) equipped with an energy dispersive spectrometer (EDS) was carried out to identify the microstructure of the samples. The SEM operates at a voltage of 1 kV to 30 kV. Specimens (~ 5 mm x 5 mm x 2 mm) cut from sintered samples were ground [silicon carbide paper, P80 ($180 \mu\text{m}$)-P4000 ($2.5 \mu\text{m}$)], polished (synthetic-silk cloth with diamond spray: $3 \mu\text{m}$ - $1 \mu\text{m}$), and were sputter coated with a gold film. Sputtering was performed in order to provide electrical conductivity at the samples surface using a plasma sputter coater (Plasma electronic GmbH, Neuenburg, Germany). The electron beam was focused by a series of electromagnetic lenses and was accelerated to the sample surface. The beam was deflected by scan coils to specific positions on the sample. Various interactions occur between the high energy electrons and proceed to different directions to the primary electron. Different detectors provide information on the investigated samples. The secondary electrons give a topographic contrast of the sample while the backscattered electrons provide compositional information based on the atomic numbers of the elements present in the sample [192].

Transition electron microscopy (TEM) was carried out with a Philips CM200 (FEI company, Oregon, USA) equipped with a CCD camera and an EDS system DX-4 (EDX, Mahwah, NJ). Image processing was performed with the software package analysis Pro (Olympus Imaging Corp. Tokyo, Japan). The instrument operates at a voltage of 20 kV to 200 kV. TEM samples were prepared by cutting thin slices approximately 6 mm x 4 mm x 2 mm from the sintered samples. They were ground as described above with the SEM samples. The final thinning to

electron transparency was prepared by dimpling (10 μm to 15 μm) and argon ion milling (2 μm). The samples were embedded in epoxy resin and coated with a thin gold layer prior to analysis.

Energy Dispersive X-ray Spectroscopy was used both in SEM and TEM for chemical analysis. Qualitative analysis was carried out to identify Al, Si and O atoms at peak positions in the generated spectrum [192].

3.3.2 Porosity analysis

The porosity was determined by two different methods. The first method makes use of computed tomography. A SkyScan 1172 X-ray Microtomography (SkyScan, Kontich, Belgium) was used to visualize and calculate the porosity of selected regions of interest, for specimens with a size of 10 mm x 3 mm x 3 mm. The Skyscan tomograph operates with an x-ray tube at 20 kV to 100 kV and is coupled to a CCD camera. The samples were attached to the sample holder with adhesive material and transferred to the measuring chamber. A voltage of 80 kV and current of 100 μA was used for acquisition of a series of two dimensional x-ray images following an exposure time of 147 ms at a stepwise rotation of 0.460°. Prior to scanning standard corrections such as frame averaging, noise reduction and random movement were performed. Cross section images were generated as a 256 grey scale image. The final 2D images were exported as BMP files for processing. The 2D reconstruction and 3D stacking were carried out with the software package NRECON and CTAn (SkyScan, Kontich, Belgium). The BMP files were imported into CTAn and a region of interest was selected. Individual algorithms used for image filtering and segmentation such as thresholding and despeckling, were carried out to separate the gray level of the solid voxels (white) and assemblage of the pore voxels (black). This allows the production of images with the separation of pores and solid material [193]. The porosity was calculated according to the algorithm implemented in the CTAn software.

Helium pycnometry (Accupy 1330, Micromeritics GmbH, Hammfelddamm, Germany) was used to measure the skeletal density and the Archimedes principle was applied to determine the bulk density. Both values were used for calculating the porosity of the samples. For the bulk density, sintered bodies were cut and polished into 15 mm x 5 mm x 4 mm rectangular specimens. The dry weight of the sample was measured in air. The samples were then immersed in water, suspended and weighed in the immersion liquid, removed and weighed in air. The bulk density was evaluated based on the Archimedes method discussed in [194, 195] using the relationship

in Eqn. (3.4). This is the weight of the object to the volume of solids plus all open and closed pores. Powders of the same samples were mortared, sieved and dried at 30 °C prior to determination of the skeletal density using helium pycnometry. The powders were weighed using the calibration cup and the skeletal density was obtained from the He gas pycnometry [196]. The porosity was evaluated based on the relationship in Eqn. (3.5).

$$\rho_{\text{bulk}} = \frac{W_{\text{dry}}}{W_{\text{sat}} - W_{\text{susp}}} \times \rho_{\text{liq}} \quad (3.4)$$

where ρ_{bulk} is the bulk density of the sample, W_{dry} is the dry weight of sample, ρ_{liq} is the density of immersion liquid, W_{sat} is the saturated weight of sample, W_{susp} is the suspended weight of sample in the liquid

$$\text{Porosity (\%)} = \left(1 - \frac{\rho_{\text{B}}}{\rho_{\text{S}}} \right) \times 100 \quad (3.5)$$

ρ_{B} = bulk density; ρ_{S} : skeletal density

The pore size distribution of the sintered samples was carried out with mercury (Hg) intrusion porometry (Quantachrome GmbH & Co. KG, Odelzhausen, Germany). Samples of 10 mm x 5 mm x 5 mm were shaped, polished and weighed. Test specimens were placed into the Hg penetrometer, evacuated and mercury was introduced. The intruded volume and pore diameter were determined by the volume of the mercury entering the pore as a function of the applied pressure in the range of 2 bar to 2236 bar [197, 198]. Different pressures (high- and low-pressure) were applied for obtaining intrusion/extrusion curves according to the pore volumes of the samples. The results were analyzed based on the PoreMaster Software package (Quantachrome GmbH & Co. KG, Odelzhausen, Germany).

3.3.3 Thermal analysis of as processed samples

The weight change of green powders was studied with NETZSCH STA 409 CD (NETZSCH Gerätebau GmbH, Selb, Germany) operating with a flow rate of 100 ml min⁻¹. As a carrier gas air was used. Ground powders of ~30 mg were placed in an Al₂O₃ crucible and Aluminium oxide was employed as the reference material during the measurements. The dimensional change of the samples (length = 16 mm, diameter = 4 mm) was monitored with NETZCH DIL 402 E, and a

heating rate of 10 K min^{-1} to a maximum temperature of $\sim 1550 \text{ }^\circ\text{C}$ under synthetic air (flow rate: 100 ml min^{-1}) was applied.

3.3.4 Specific surface area

The specific surface area (SSA) was determined with the nitrogen adsorption technique using the BET method [199]. Previously sintered samples of $10 \text{ mm} \times 5 \text{ mm} \times 5 \text{ mm}$ were heat treated at a temperature of $130 \text{ }^\circ\text{C}$ under N_2 -atmosphere for 2 h to remove any contaminants. The samples were placed in an evacuated glass chamber and were flushed with nitrogen, then locked and cooled down to the temperature of liquid nitrogen. The pressure difference to a reference chamber was measured. An ASAP 2000 analyzer (Micromeritics GmbH, Aachen, Germany) was used to evaluate the specific surface area.

3.3.5 Thermal analysis of sintered samples

A laser flash apparatus (LFA) 427 (NETZSCH Gerätebau GmbH, Selb, Germany) was used for measuring the thermal diffusivity under argon atmosphere. The sample diameter was $\sim 12.6 \text{ mm}$ and the thickness was 2 mm . The specimens were graphite coated to enhance the absorption of laser energy, and the measurement was performed up to $1000 \text{ }^\circ\text{C}$. The heat capacity (C_p) was measured with a differential scanning calorimeter (DSC) 404 C Pegasus. Disk shaped samples of a diameter of 5 mm and a thickness of 1 mm were used. Disks were placed in a corundum crucible attached to an S type thermocouple. The heat capacity from room temperature to $1000 \text{ }^\circ\text{C}$ (5 K min^{-1}) was evaluated based on the Proteus data acquisition and analysis software. A DIL 402 C pushrod dilatometer was used to determine the thermal expansion and the corresponding linear dimensional change of the sample ($\varnothing = 5.5 \text{ mm}$, $l = 25 \text{ mm}$) was measured from room temperature to $1000 \text{ }^\circ\text{C}$. The thermal conductivity (λ) was obtained from measurements of the heat capacity (C_p), the thermal diffusivity (D_{th}) and the density (ρ), and is calculated based on Eqn. (3.6).

$$\lambda = C_p D_{th} \rho \quad (3.6)$$

The linear coefficient of thermal expansion (α) of the sintered samples was measured with a dilatometer DIL 402 C (NETZSCH Gerätebau GmbH, Selb, Germany). Samples of 25 mm length and $\sim 5.5 \text{ mm}$ diameter were used. They were placed in the furnace inside the sample holder

attached to a pushrod. A heating rate of 5 K min⁻¹ was applied up to 1550 °C. The resultant expansion is a sum of the length changes of the sample, pushrod and sample holder. A corrective curve was used to remove additional changes from the push rod and the sample holder. The linear CTE was calculated based on Eqn. (3.7).

$$\alpha = \frac{1}{L_0} \frac{\Delta L}{\Delta T} \quad (3.7)$$

Where L₀: length of sample at ambient temperature, ΔL: change in length of sample to 1550 °C, ΔT: change in temperature

3.4 Material properties

3.4.1 Mechanical characterization

Flexural strength, Young`s modulus and Weibull statistics

Measurements were carried out with samples sintered at 1200 °C, 1400 °C and 1600 °C, a heating rate of 5 K min⁻¹ was applied with holding times of 3 h and 12 h at each temperature. The flexural strength was measured with a universal testing machine (Zwick/Roell 2100, Zwick GmbH & Co.KG, Ulm, Germany) using samples with dimensions of 25 mm x 2.5 mm x 2.5 mm, on a 25 mm span and cross head speed of 0.1 mm min⁻¹. The flexural strength values were determined at room temperature, at 500 °C and at 1000 °C in the three point bending mode. The holding time prior to high temperature measurement was 30 minutes. From the 3-point bending data the flexural strength was determined according to Eqn. (3.8), and the Young`s modulus was calculated according to Eqn. (3.9). In order to analyze the failure probability, 3-point bending data were used to calculate the Weibull modulus.

$$\sigma_{3pt} = \frac{3LP}{2bd^2} \quad (3.8)$$

$$E = \frac{L^3 M}{4bd^3} \quad (3.9)$$

where σ = flexural strength, L = support span, P = force, b = width of specimens, d = height of specimens, E = Young`s-modulus, M = tangent of the straight line of the load deflection beam.

The failure probability of the samples is related to the applied stress according to Eqn. (3.10), being a two parameter Weibull form which relates the scatter of fracture strength to the Weibull distribution. The failure probability corresponds to 10 samples for both sample series TEOS-23 and CS-23. The plot of $\text{LnLn}[1/(1-P_{fi})]$ of the cumulative probability of failure versus the fracture stress $\text{Ln}\sigma_i$ was fitted to a straight line. The Weibull parameter m is determined from the slope of this line represented in Eqn. (3.11), and the characteristic threshold strength (σ_0) values were obtained when $F = 0.632$ [40] or $\text{LnLn}[1/(1-P_{fi})] = 0$

$$F = 1 - \exp\left[-\left(\frac{\sigma_i}{\sigma_0}\right)^m\right] \quad (3.10)$$

$$\ln\left[\ln\left(\frac{1}{1-P_{fi}}\right)\right] = m\ln\sigma_i - m\ln\sigma_0 \quad (3.11)$$

where F = cumulative density function, σ_i = normalized material strength, σ_0 = threshold stress, m = weibull parameter, P_f = failure probability, ($f_i = i-0.5/n$), n = total number of specimens, i = specimens number.

Microhardness

A microhardness tester MHT-10 (Anton Paar GmbH, Ostildern, Germany) was used in combination with an optical microscope for hardness analysis. Specimens of 5 mm x 5 mm x 3 mm were polished and placed on the x-y stage and focused to optimum resolution. A load of 4N was applied for 5 s to the sample surface and the Vickers hardness was obtained from the ratio of the applied force to the mean of the two diagonals of the indentation according to Eqn. (3.12). Figure 3.3 shows an example after the hardness measurement.

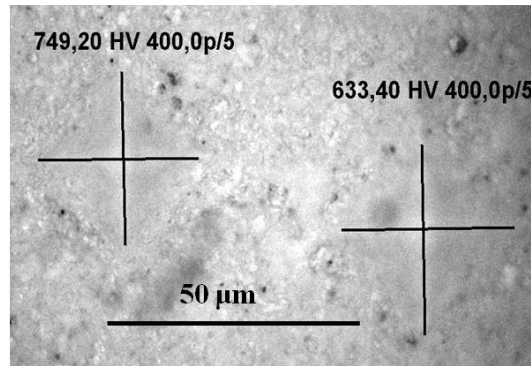


Figure 3.3: Indentation on a surface of the TEOS-23 sample

$$HV = 0.1891 \frac{F}{d^2} \quad (3.12)$$

where HV: Vickers hardness, F: applied load (N), d: mean of the two diagonals of the indentation (mm)

3.4.2 Thermal shock characterization

The influence of thermal cycling on the microstructure of sintered samples was analyzed using an x-ray computer tomograph Phoenix nanotom® S (GE Sensing & Inspection Technologies GmbH, Wunstorf, Germany) operating at 180 KeV/15 W. The μ -CT analyzer is suitable for non-destructive imaging and visualization. Thermal cycling tests were carried out with sample bars of 6 mm x 3 x mm 2 mm sintered at 1600 °C with holding times of 12 h. These samples were heated to a temperature of 1000 °C and 1200 °C, respectively. The samples were kept in the furnace for 30 min in order to achieve uniformity in temperature. Water was used as quenching medium with 5, 10, 15 and 20 cycles tested for each temperature [200, 201]. The sample transfer to the quenching medium was carried out within 5 s. The samples were dried after quenching at 500 °C for 3 h, followed by density measurements and imaging with the μ -CT. All samples were imaged before and after thermal cycling. Sample with a geometry 6 mm x 3 mm x 2 mm were mounted on the sample holder, and a voltage of 60 kV to 80 kV and current of 40 μ A to 70 μ A was used for acquisition of a series of two-dimensional x-ray images at an exposure time of 1 ms with a rotation step of 0.25° (i.e. 4 pictures per 1° rotation). The images were recorded and subsequently reconstructed to obtain a volume of interest. Cross section images were generated using the GE-reconstruction software, with different attenuation values to obtain a 256 grey scale image, which represents a section through the sample. The final image was exported as BMP data for processing. The 2D reconstruction was carried out with the Phoenix datos/x CT software.

The thermal shock behaviour of the samples was evaluated based on thermal and mechanical data. These data were used with the equations proposed by Hasselman and Kingery for estimating the critical temperature difference for an expected failure (ΔT) and the thermal shock resistance (R_s) of a material to fracture initiation by thermal stresses, see Eqn. (3.13) and Eqn. (3.14), respectively.

$$\Delta T = \frac{[\sigma(1 - \nu)]}{E\alpha} \quad (3.13)$$

$$R_s = \frac{\lambda[\sigma(1 - \nu)]}{E\alpha} \quad (3.14)$$

where ΔT : = Critical temperature difference for expected failure, R_s = thermal shock resistance of material to fracture initiation by thermal stresses, E = Young's modulus, σ = flexural strength, α = thermal expansion coefficient, λ = Thermal conductivity, ν = the Poisson's ratio.

4 Results and discussion

4.1 Rheological behaviour, sample shape and shrinkage

4.1.1 Rheological behaviour

Figure 4.1 shows the viscosity versus the shear rate for the two sample series. The highest viscosity at low shear rates was found in the CS-23 system. The viscosity of both CS samples is higher as compared to that of the TEOS samples.

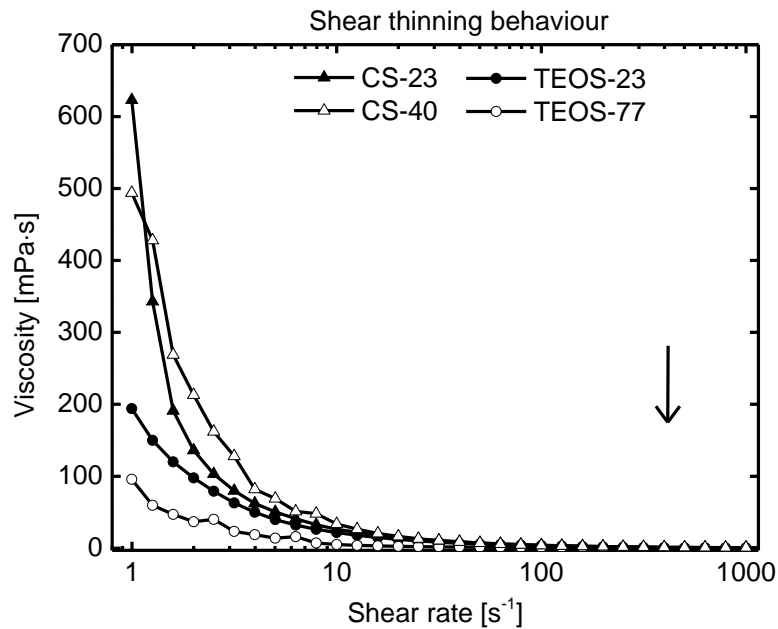


Figure 4.1: Variation of viscosity versus shear rate

The viscosity decreases in all samples with an increasing shear rate. This indicates a shear thinning behaviour of these systems. Shear thinning is important for casting process. At high flow rates, e.g. in shaping processes such as pouring the suspension into a mold, a low viscosity results; at low flow rates an increase in the viscosity occurs. This behaviour is important for the sedimentation of fillers: no or negligible sedimentation effects occur after shaping [89].

The high viscosity of the CS might be explained by two facts: In the TEOS system hydrolysis reaction occur converting Si-OR groups to Si-OH groups, ligands slow down hydrolysis with more water use (TEOS-23: H₂O/TEOS = 2) compared to the CS system with reactive silanol

groups and less water use (CS-23: H₂O/CS = 1), see Table 3.1 and Table 3.3. The higher amount of water used in the former system reduces its viscosity. The viscosity of the supplied colloidal silica is 20 mPa·s at 25 °C compared 0.8 mPa·s at 25 °C for TEOS. The second fact is that CS is a suspension of particles in water, thus the particle load of the CS system is higher compared to that of the TEOS system.

The catalyst amount also influenced the viscosity differently, suspensions with a pH value of 6 showed a lower starting viscosity and the resultant cast samples dried more homogeneously compared to samples with pH values ≤2 and ≥10 with fast evaporation and inhomogeneous drying. With a pH value of 6, the alumina particles are positively charged whereas the silica particles are negatively charged which enabled heteroflocculation suitable for gel formation in mullite systems [85]. The catalyst is important for the separation of the particles in the suspensions. An acidic catalyst is preferred due to the higher reaction rate within the suspension and thus limited evaporation [1].

The suspensions were poured into Teflon® molds at room temperature and dried at a relative humidity of 85 % for a period of four (TEOS-23 and CS-23), five (CS-40) and six (TEOS-77) weeks. The de-molding of the green samples containing TEOS-77 and CS-60 lead often to damage while easy de-molding and mechanically stable green forms were obtained from TEOS-23 and CS-23 samples. The high amount of TEOS and CS in the former samples might have affected the de-molding process. The difficulties in de-molding were reflected in drying and machining of the resultant samples.

4.1.2 Green sample shaping and stability after heat treatment

Drying of the green samples was carried out in three stages. A primary step in which de-molded samples were dried at intervals of 50 °C to 200 °C, with a holding time of 5 h at peak temperature. This was to achieve uniformity in temperature, to minimize warping and to reduce cracking. A secondary stage in which the compacts were subjected to a heat treatment of 5 K min⁻¹ to 700 °C with holding time 3 h was applied, and samples are shown in Figure 4.2 and Figure 4.3. This step was applied since the machining is less tool-consuming in the pre-fired state.

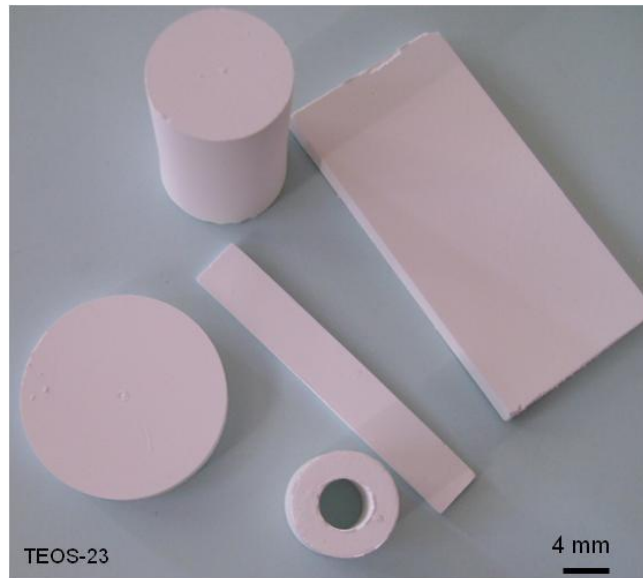


Figure 4.2: TEOS-23 green samples heat-treated to 700 °C with a holding time of 3 h; disk (\varnothing : 42 mm, H: 4 mm); block cylinder (L: 30 mm, \varnothing : 20 mm), hollow cylinder (L: 20 mm, inner \varnothing : 10 mm, outer \varnothing : 16 mm), rectangular plates (72 mm x 32 mm x 4 mm), rectangular bars (72 mm x 4 mm x 3 mm) where \varnothing : diameter, H: thickness, L: length

The obtained samples from TEOS-23 and CS-23 compositions were mechanically stable for pre-machining processes such as cutting and polishing in comparison to smaller samples from the other compositions, related to the difficulties in de-molding as previously explained.

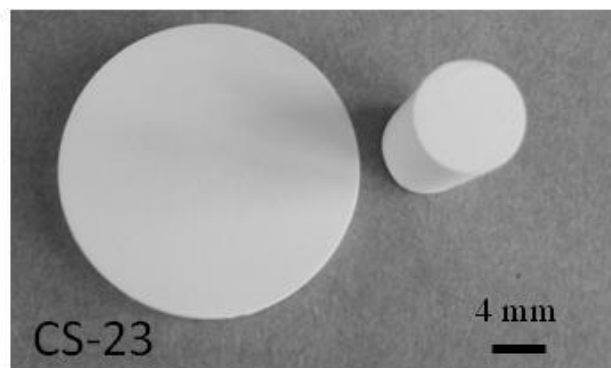


Figure 4.3: CS-23 green samples heat-treated to 700 °C with a holding time of 3 h; disk (\varnothing : 42 mm, H: 4 mm), cylinder (L: 18 mm, \varnothing : 14 mm)

Sintering was performed for the pre-machined samples in air to a maximum temperature range between 1100 °C to 1600 °C at 5 K min⁻¹ with holding times of 3 h and 12 h. It was concluded

that pre-machining cracks before final sintering, were healed by heat treatment. The fired samples with different geometries are shown in Figure 4.4 and Figure 4.5. The TEOS series allowed more complex shapes compared to the CS series, possibly due to its lower viscosity as described above. The CS samples represent a higher hardness when demolded compared to the TEOS samples. The metallographic preparation of the CS samples showed particles pull out, compared to less effect observed with the TEOS samples, this limit the size and shape of samples obtained from the CS series.

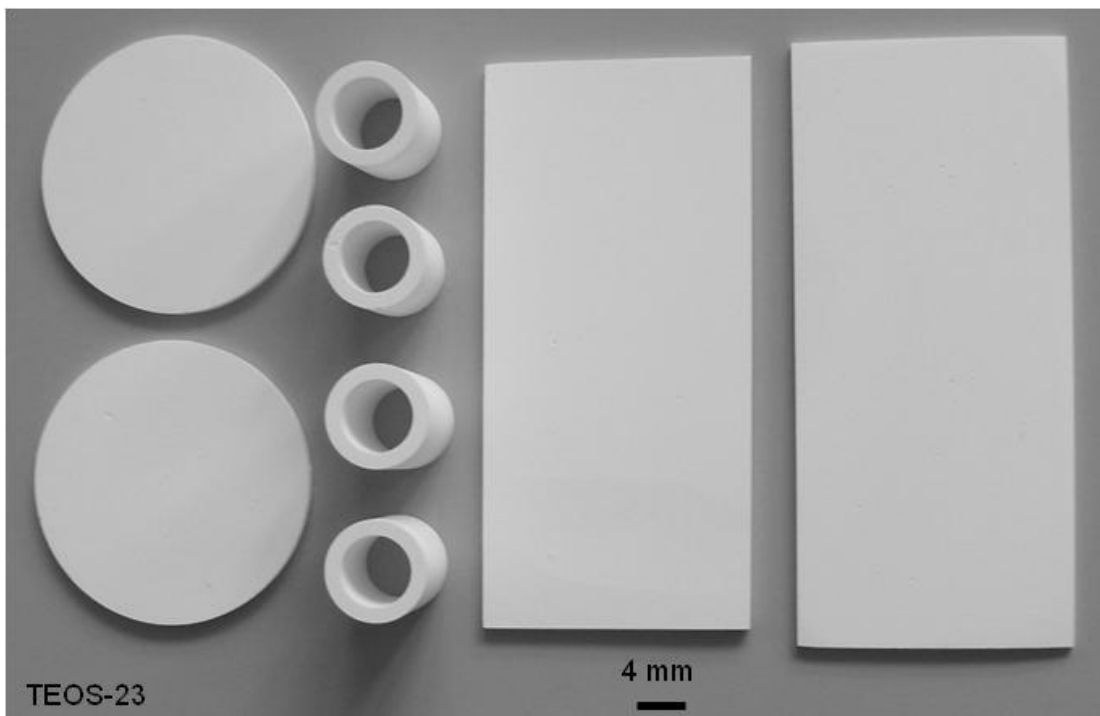


Figure 4.4: TEOS-23 ceramic parts sintered at 1600 °C with a holding time of 12 h; disk (\varnothing : 40 mm, H: 2 mm); cylinder (L: 15 mm, inner \varnothing : 8 mm, outer \varnothing : 12 mm), rectangular plates (70 mm x 30 mm x 2 mm)

Samples from the different compositions were machined based on the requirements for different characterization techniques with processing dimensions and measurement methods shown in Table 4.1. Powders were prepared from corresponding samples according to the characterization methods described in chapter 3.

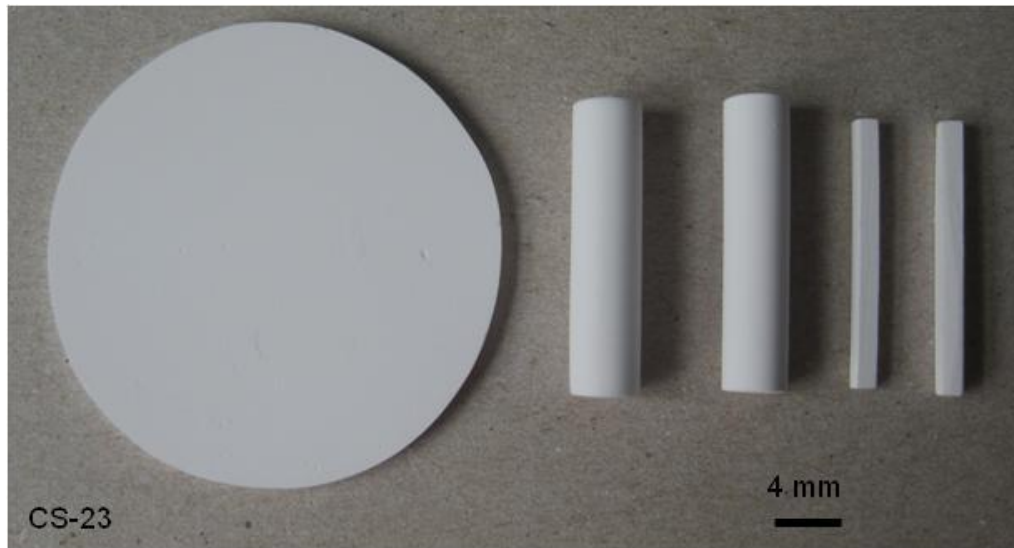


Figure 4.5: CS-23 ceramic parts (1600 °C, 12 h); disk (\varnothing : 40 mm, H: 2 mm), cylindrical bars (L= 25, H = 5.5 mm), rectangular bars (25 mm x 2.5 mm x 2.5 mm)

Table 4.1: Dimension of samples and characterization methods

Sample dimension	Measurement
L = 16 mm, \varnothing = 4 mm	shrinkage of green samples
5 mm x 5 mm x 2 mm	SEM analysis
6 mm x 4 mm x 2 mm	TEM analysis
10 mm x 5 mm x 5 mm	bulk density
10 mm x 5 mm x 5 mm	specific surface area
\varnothing = 12.6 mm, H = 2 mm	thermal diffusivity
\varnothing = 5 mm, H = 1 mm	heat capacity
L = 25 mm, \varnothing = 5.5 mm	linear coefficient of thermal expansion
25 mm x 2.5 mm x 2.5 mm	flexural strength
5 mm x 4 mm x 4 mm	Vickers hardness
6 mm x 3 mm x 2 mm	thermal cycling test with μ -CT

4.2 Thermal analysis of the as processed parts

The shrinkage behaviour as shown in Figure 4.6 was measured with a heating rate of 5 K min⁻¹ up to 1550 °C in synthetic air. The sample length does not change up to 300 °C, followed by a small change in length to ~1000 °C. Significant shrinkage occurs between 1100 °C and 1450 °C. Prior to 700 °C compacts show little shrinkage due to cross linking reactions of TEOS or CS, see also Eqn. (2.6). As the temperature increases, siloxane ($\equiv\text{Si-O-Si}\equiv$) and $\equiv\text{Si-O-Al}\equiv$ bridges are formed, see reaction mechanisms in Figure 2.8 [80, 88]. The onset of the densification is indicated at approximately 1000 °C to 1100 °C [1]. The linear shrinkage of the samples is listed in Table 4.2.

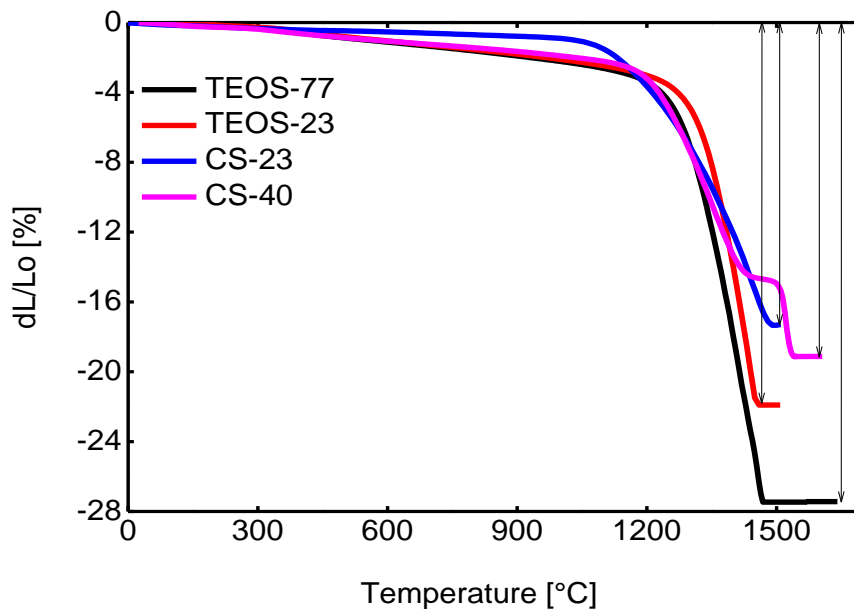


Figure 4.6: Shrinkage of green samples

Table 4.2: Shrinkage and mass change of the compacts sintered to 1550 °C at 5 K min⁻¹

Sample	After pre-drying	
	shrinkage (%)	mass change (%)
TEOS-23	22	12
CS-23	17	4.5
TEOS-77	27	13.5
CS-40	19	6

Figure 4.7 (left) represents the weight loss for different powders sintered in air at 5 K min^{-1} to a maximum temperature of $1550 \text{ }^\circ\text{C}$. The weight loss can be divided into three regions; the region from $25 \text{ }^\circ\text{C}$ to $300 \text{ }^\circ\text{C}$ with a high weight loss which is related to the loss of water and/or part of TEOS; the region from $400 \text{ }^\circ\text{C}$ to $1000 \text{ }^\circ\text{C}$ with a smaller weight loss caused by dehydration of Si-OH groups and Al-OH groups [92] and the region from $1100 \text{ }^\circ\text{C}$ to $1550 \text{ }^\circ\text{C}$ with little or no significant weight change. The TEOS samples showed a higher weight loss which originates from the TEOS hydrolysis and its increase in intensity with an increasing amount of TEOS, see also Table 4.2. Heating of the TEOS green samples resulted in condensation and a loss of four moles ethanol per mole TEOS, if the TEOS is not completely cross linked yet. This would explain the significant higher weight loss compared to the CS samples [81, 84].

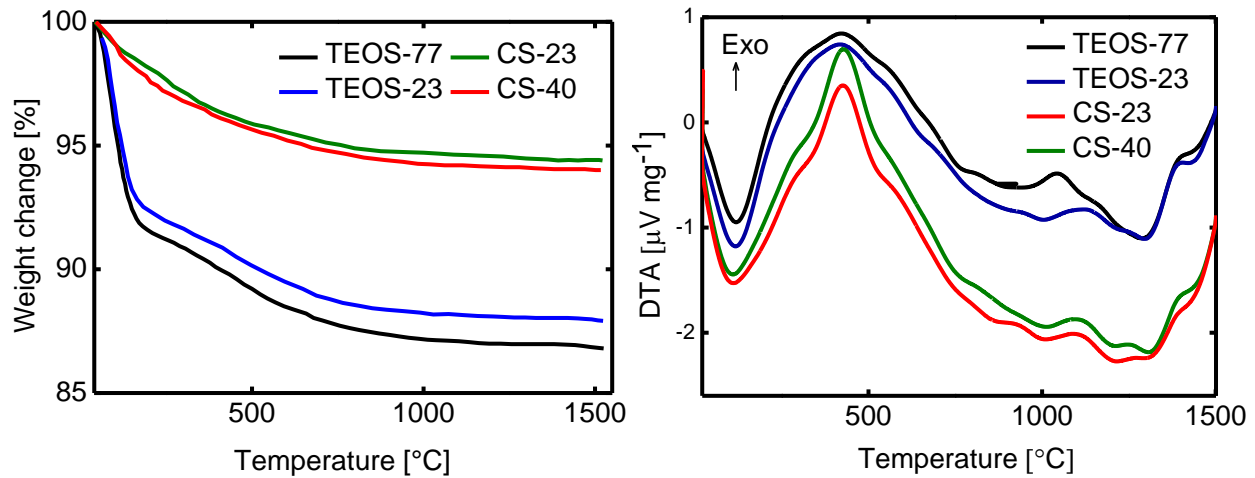


Figure 4.7: Thermal analysis of green samples heat treated to $1550 \text{ }^\circ\text{C}$ in air at 5 K min^{-1}

DTA analysis shown in Figure 4.7 (right) revealed an endothermic peak at $125 \text{ }^\circ\text{C}$ for CS samples and an endothermic peak at $130 \text{ }^\circ\text{C}$ for the TEOS samples. An increase of the temperature to $900 \text{ }^\circ\text{C}$ intensified the dehydration reactions of the OH groups and the liberation of trapped water within the pores. The onset of densification (see Figure 4.6) is indicated by an endothermic region ranging from $900 \text{ }^\circ\text{C}$ to $1000 \text{ }^\circ\text{C}$ for the CS series and shifted to $1000 \text{ }^\circ\text{C}$ for the TEOS samples, which was also found in [52]. Smaller endothermic peaks are found in the CS samples prior to $1000 \text{ }^\circ\text{C}$ indicating the onset of crystallizing to cristobalite. An increase in the temperature indicates a strong endothermic peak at $\sim 1200 \text{ }^\circ\text{C}$ for the CS samples and $\sim 1300 \text{ }^\circ\text{C}$ for the TEOS samples. This is related to the onset of the mullite phase formation and was confirmed by TEM measurements [5]. However the oxidation of the residuals is associated with exothermic peaks in the temperature range between $200 \text{ }^\circ\text{C}$ to $600 \text{ }^\circ\text{C}$ [80].

A higher weight loss and shrinkage was found with the TEOS samples compared to the CS samples. This is attributed to the higher TEOS content in the TEOS-77 sample. It is also noticed that samples with a high amount of alumina present a low weight loss and shrinkage when compared within the same series.

4.3 Microstructure and porosity of sintered samples

4.3.1 SEM and XRD analysis

SEM images of samples after sintering in the temperature range from 1200 °C to 1600 °C are represented in Figure 4.8 (TEOS-23 and CS-23) and Figure 4.9 (TEOS-77 and CS-40). As demonstrated by the SEM images, the silica source and silica content influences the morphology of the materials. In the TEOS samples the particles appear separated, Figure 4.8 (a) while parts of the CS samples appear amorphous, Figure 4.8 (d). Sintering at 1400 °C did not show significant changes compared to samples sintered at 1200 °C. A major change in the sample morphology was observed after sintering at 1600 °C. While TEOS samples showed a pronounced porosity, the CS samples appear less porous. No major difference between the TEOS-23 and CS-23 samples morphology has been found after sintering at 1600 °C. The grain sizes seem to increase for all the samples sintered at 1600 °C. CS samples, however, show well developed grains. The TEOS-77, Figure 4.9 (left) and CS-40 samples, Figure 4.9 (right) seem to host a glassy phase. This is attributed to the silica phase; their amount in sample (TEOS-77) is higher compared to the silica amount in the samples containing TEOS-23 and CS-23 [57].

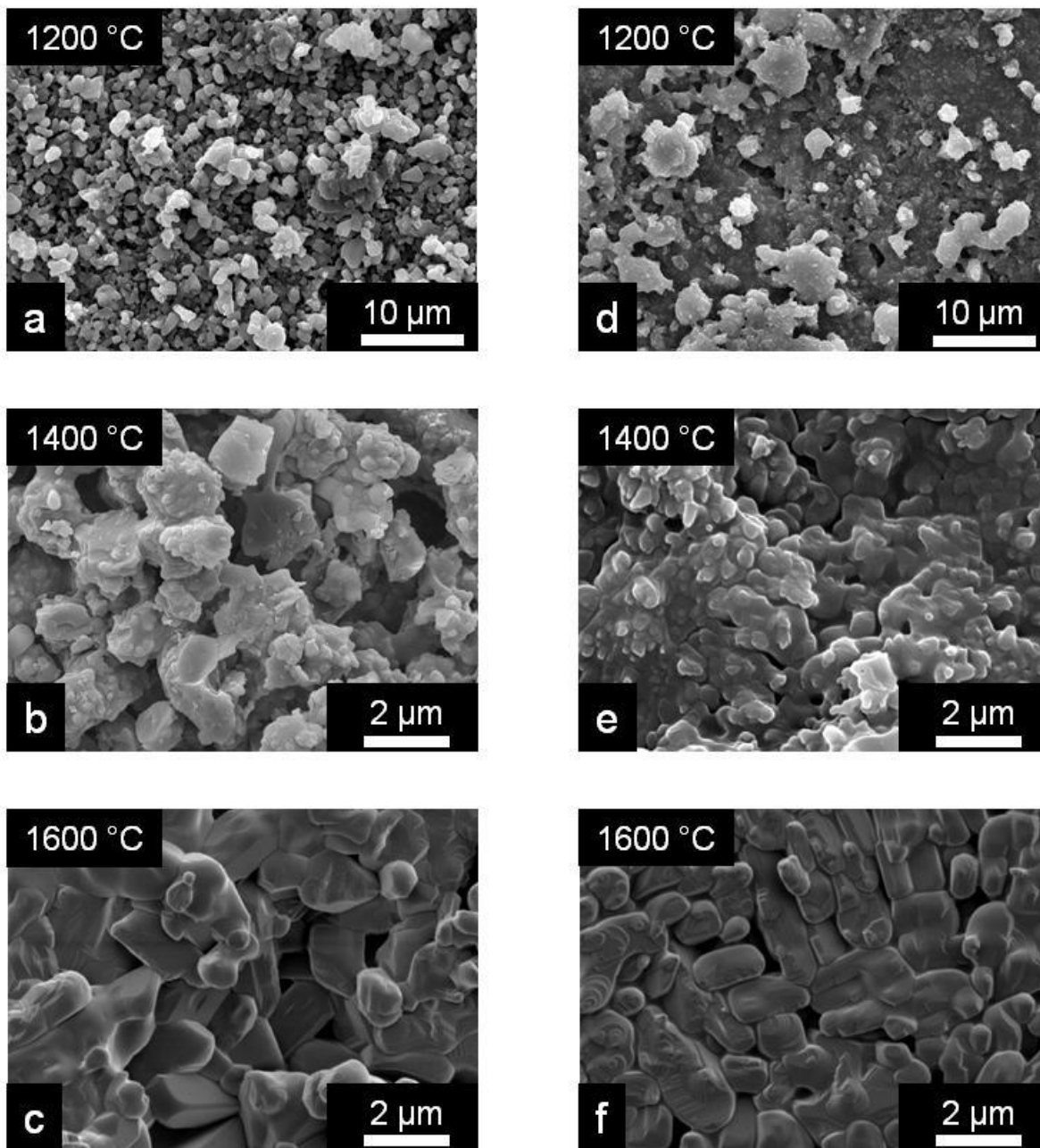


Figure 4.8: TEOS-23 (left) and CS-23 (right) SEM images of samples sintered from 1200 °C to 1600 °C, at 5 K min⁻¹ with holding time of 12 h at peak temperature

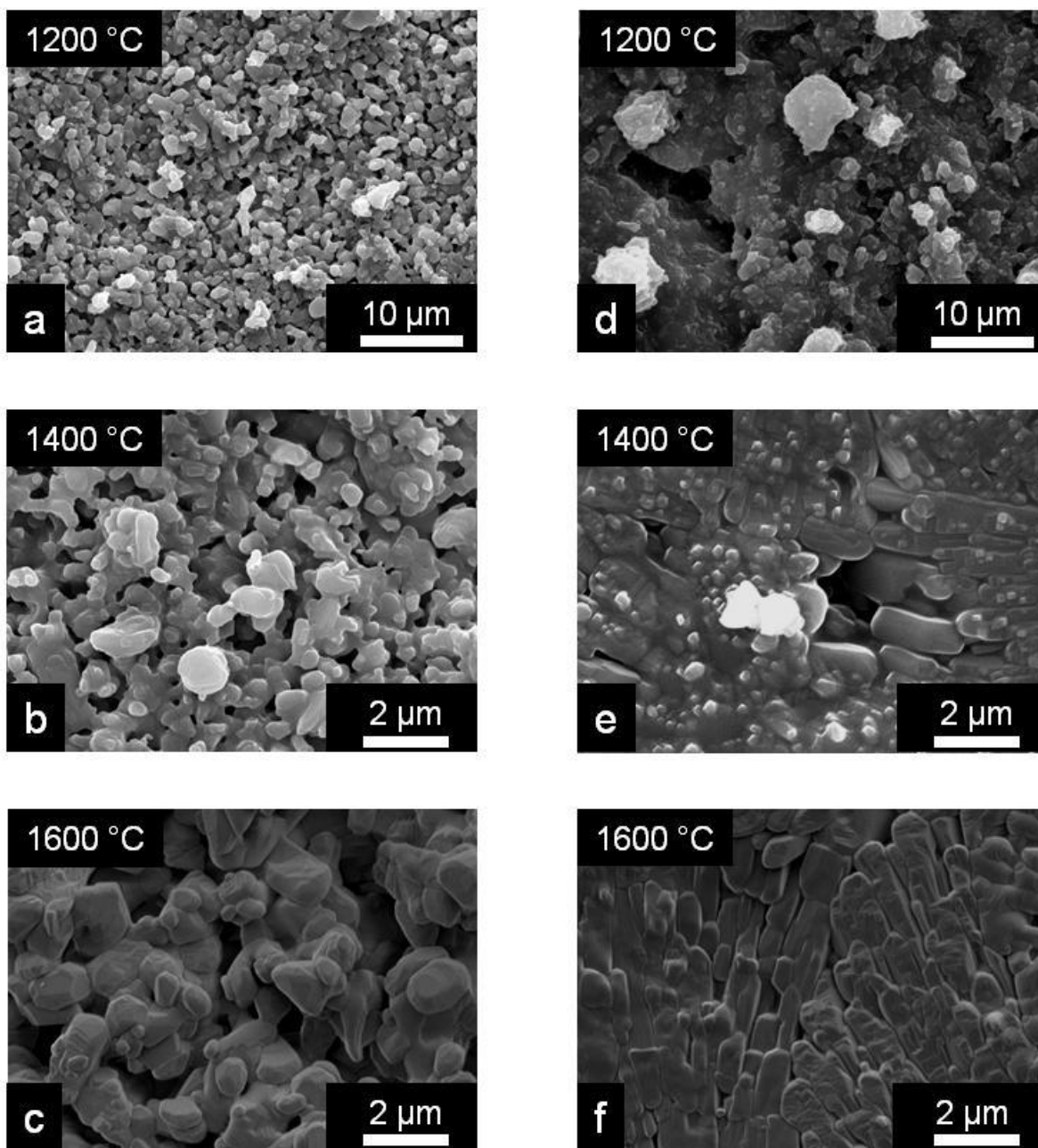


Figure 4.9: TEOS-77 (left) and CS-40 (right) SEM images of samples sintered from 1200 °C to 1600 °C, at 5 K min⁻¹ with holding time of 12 h at peak temperature

The phase evolution as a function of the firing temperature was analyzed by XRD and is shown in Figure 4.11 (a) for TEOS-23, Figure 4.11 (b) for CS-23, Figure 4.11 (c) for TEOS-77 and Figure 4.11 (d) for CS-40 samples. Details based on Rietveld quantitative analysis are listed in Appendix 11. The peak intensities of the corresponding phases are represented in Figure 4.10, and Appendix 12 to Appendix 14. In the assessment of the phase compositions, peaks with a

high intensity were cristobalite (tetragonal system, hkl: 011, 2θ -CuK α : 21.9°), corundum (hexagonal system, hkl: 012, 2θ -CuK α : 25.5°) and mullite (orthorhombic system, hkl: 110, 2θ -CuK α : 16.4°); some traces were identified as sillimanite (anorthite), cristobalite low (cubic), and tridymite (anorthite) [52, 101]. Changes in the peak patterns were clearly observed between 1200 °C to 1600 °C which confirmed the transformation into mullite. A semi-quantitative analysis based on XRD data was carried out with the Rietveld method.

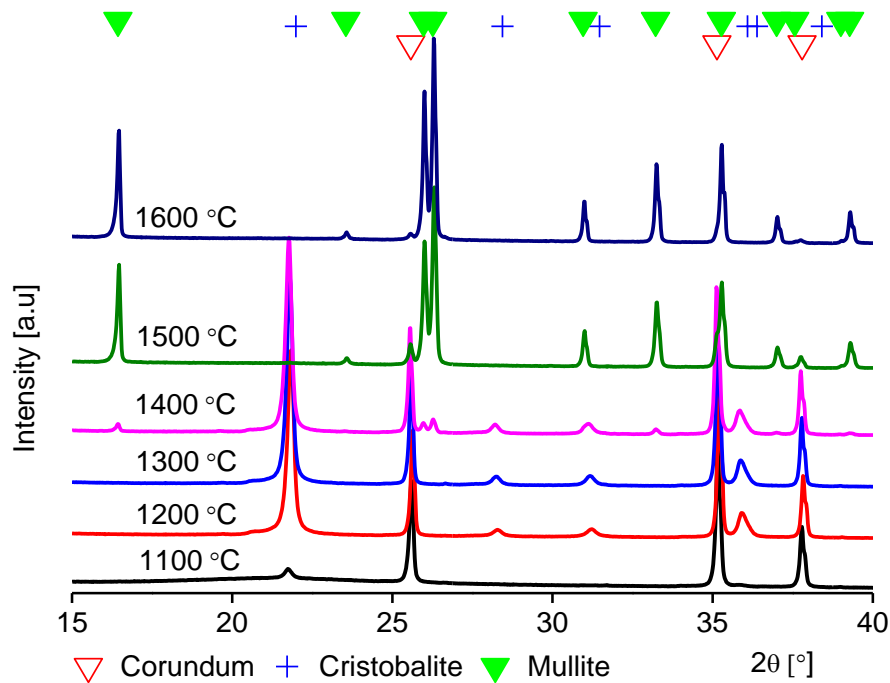


Figure 4.10: XRD patterns of the CS-40 samples sintered at different temperatures with holding times of 12 h

The phase composition of all sample series as a function of the sintering temperature is given in Figure 4.11, and details are listed in Appendix 11. The composition changes with an increase in the heating temperature from 1100 °C to 1600 °C. In the series with CS, cristobalite formation starts at 1100 °C (see Figure 4.10, cristobalite: 2θ -CuK α : ~21.9°) while in the TEOS series, cristobalite was observed at 1200 °C (see Appendix 14, cristobalite: 2θ -CuK α : ~21.9°). A similar effect was found with the onset temperature of the mullite formation. Traces of mullite were found in the base peaks of the CS series for samples sintered at 1300 °C while in the TEOS derived samples, traces were found at temperatures ≥ 1350 °C. Samples sintered at 1400 °C

indicated a high amount of mullite in the CS series in the range from 7 mol.-% to 23 mol.-% compared to 4 mol.-% for the TEOS-23 sample. In the TEOS-77 derived samples, mullite appeared after sintering at 1500 °C. At a maximum temperature of 1600 °C, all samples revealed an increase in their amount of mullite and a corresponding decrease in the cristobalite and corundum amount, see, Figure 4.11.

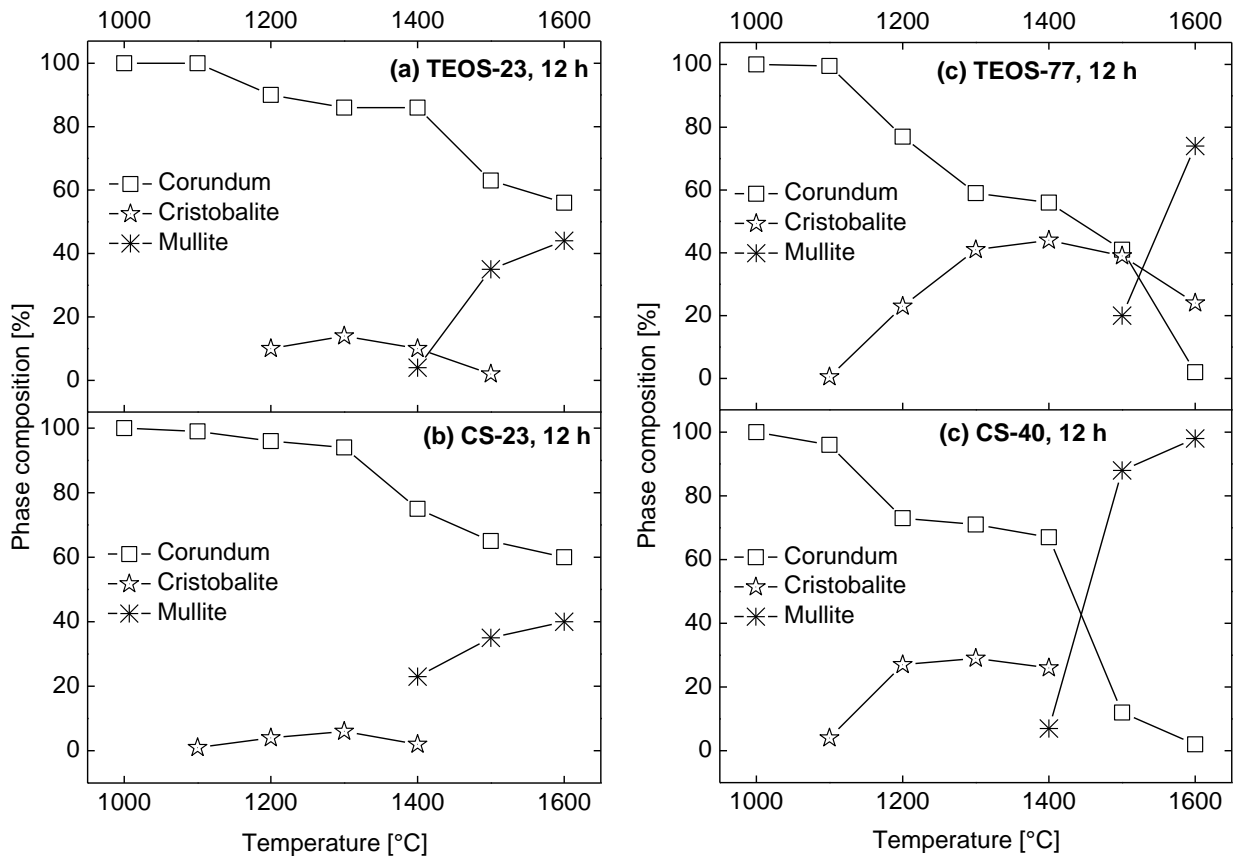


Figure 4.11: Semi quantitative Rietveld analysis of samples after sintering in a temperature range from 1100 °C to 1600 °C with holding times of 12 h

The main differences between the samples might be related to the starting composition. The TEOS-77 sample sintered at 1600 °C for 12 h, showed 24 mol.-% cristobalite due to its high amount of TEOS used in the sample preparation. Approximately 2 mol.-% corundum was found unreacted. This might have come from mullite formation at the interface of cristobalite and corundum [132]. A similar effect was found in the CS-40 sample with 98 mol.-% mullite and 2 mol.-% corundum. XRD indicated a corundum-to-mullite molar ratio of 56:44 for the TEOS-23 sample and 60:40 for the CS-23 sample, respectively. The difference in 4 mol.-% mullite less in

the CS-23 sample might be a consequence of its early densification (i.e. 900 °C), which retards complete densification before the onset of the mullitization. Phase segregation might have occurred which caused reduced decrease in the mullitization rate of this system compared to a higher densification rate of the TEOS-23 sample which started at ~1000 °C with a high mullitization rate [82, 133].

Results of the phase analysis of samples with a holding time of 3 h at peak temperature are shown in Figure 4.12 and details are given in Appendix 15

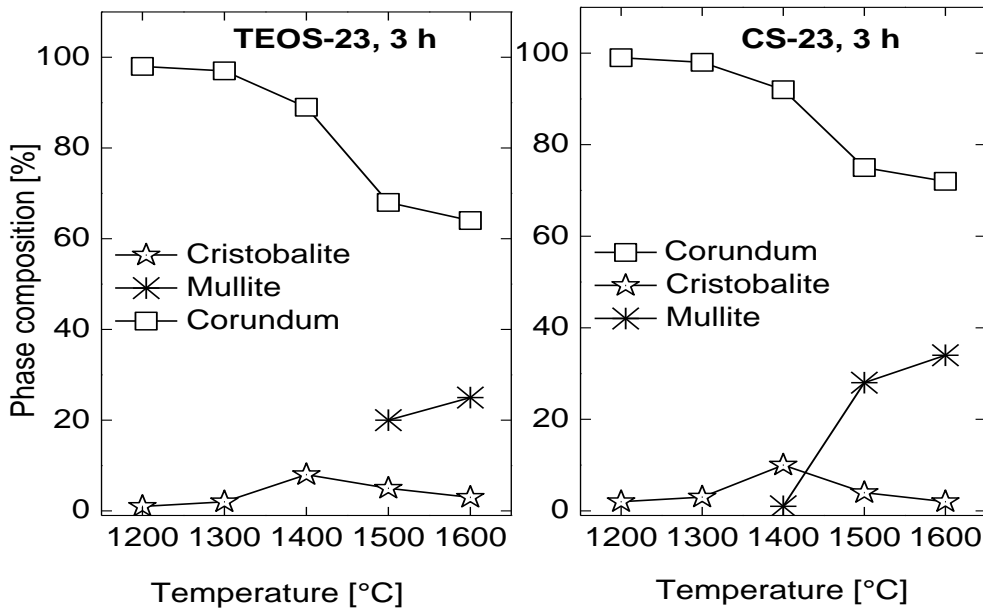


Figure 4.12: XRD phase analysis of samples sintered at different temperatures with holding times of 3 h at peak temperature

For 12 h holding time, first cristobalite was identified at a temperature of 1100 °C compared to a shift to 1200 °C for 3 h holding times found in the CS series. A similar shift was observed in the TEOS-series. Mullite was found at 1400 °C following a holding time of 12 h and a shift to higher temperatures was observed at a holding time of 3 h, see Figure 4.12. A complete mullitization for TEOS-23 and CS-23 samples sintered at 1600 °C for 3 h holding time was not observed, as found for 12 h holding time, see Figure 4.11 for samples sintered at 1600 °C for 12 h.

The first formation of cristobalite was identified at 1100 °C corresponding to a decrease in the alumina content [132]. Cristobalite and mullite formation vary with starting material

characteristics, temperature and holding time. Prior to 1100 °C the only crystalline phase was alumina and no cristobalite was found before this temperature. Cristobalite was considered to exist in an amorphous form, which was not indicated by XRD. For a more detailed look inside the samples, TEM studies were carried out. Prior to this study the porosity was analysed. The results are presented in the following section.

4.3.2 Porosity analysis

The density, porosity, pore size and specific surface area were measured as described in chapter 3. Figure 4.13 and Figure 4.14 show the bulk density, the skeletal density and the total porosity for the samples after sintering between 1200 °C and 1600 °C for a holding time of 12 h at peak temperature, see Appendix 16 for calculated density and porosity values.

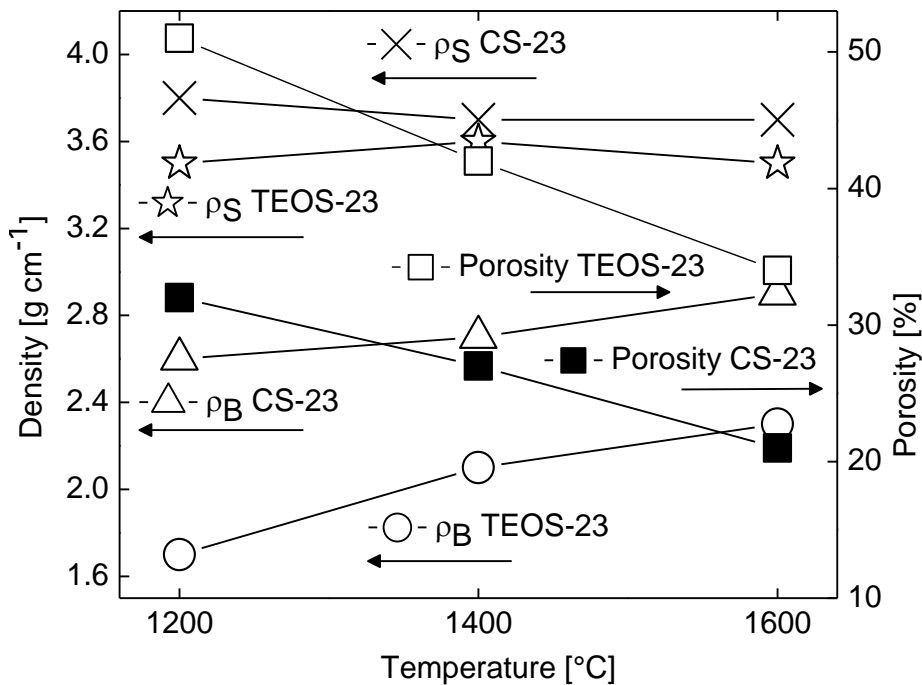


Figure 4.13: Bulk density (ρ_B), skeletal density (ρ_S) and porosity of TEOS-23 and CS-23 samples sintered in the temperature range from 1200 °C to 1600 °C for 12 h

The bulk density values were found to increase with an increasing annealing temperature. A bulk density of 2.96 g cm⁻³ was measured for the CS-23 sample compared to 2.31 g cm⁻³ for the TEOS-23 sample, in comparison to a value of 3 g cm⁻³ reported for alumina-mullite in [141, 180].

The CS series possesses a higher bulk density compared to the TEOS series. A probable reason for this is the start of the densification process at 900 °C, see also Figure 4.7. A bulk density of 2.96 g cm⁻³ was measured for the CS-77 sample prepared with 23/77 mol.-% of SiO₂/Al₂O₃ compared to 2.86 g cm⁻³ for the CS-40 sample prepared with 40/60 mol.-% of SiO₂/Al₂O₃, respectively. The differences in bulk density values for the CS series is linked to the intense densification of the CS-40 sample with 4 mol.-% cristobalite found following sintering at 1100 °C compared to 1 mol.-% cristobalite found with the CS-23 sample, see Appendix 11.

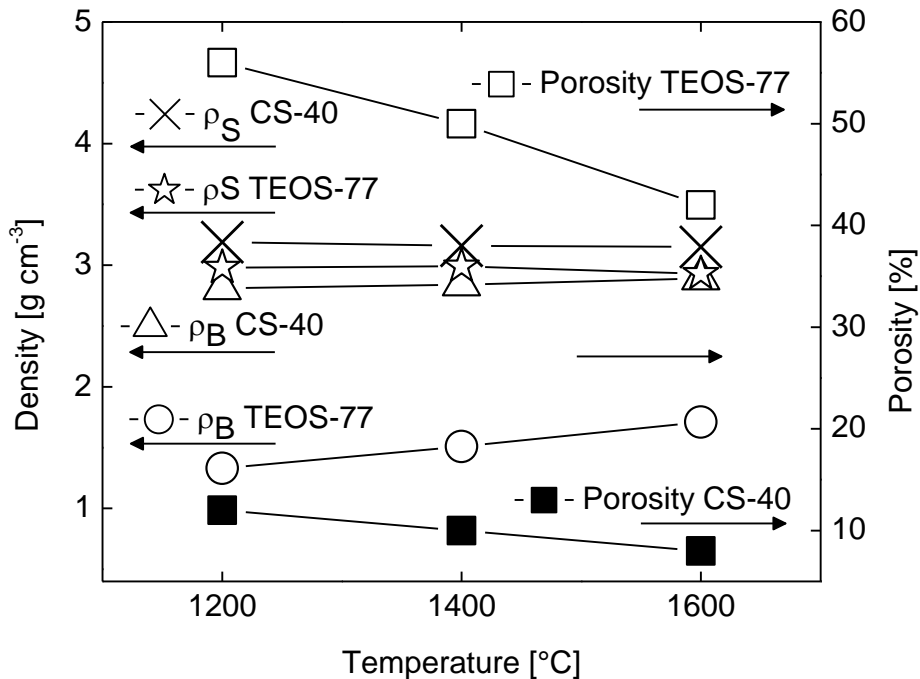


Figure 4.14: Bulk density (ρ_B), skeletal density (ρ_S) and porosity of TEOS-77 and CS-60 samples sintered in the temperature range from 1200 °C to 1600 °C with a holding time at peak temperature of 12 h

The increase in bulk density from 1100 °C to 1600 °C is associated to the transformation of metastable siliceous amorphous forms to stable and crystalline cristobalite which react with alumina and mullite is formed. Generally it is observed in all samples that cristobalite formation increase densification reducing reaction paths for Al and Si ions leading to intensification of mullitization with increasing bulk densities [71], following pore consolidation, pore removal, components shrinkage and grain growth. The bulk density was also found to be controlled by the amount of silica source. Within the TEOS series, the TEOS-77 sample prepared with 77/23 mol.-%

% of $\text{SiO}_2/\text{Al}_2\text{O}_3$ represents a lower bulk density of 1.71 g cm^{-3} compared to 2.31 g cm^{-3} for the TEOS-23 sample prepared with 23/77 mol.-% of $\text{SiO}_2/\text{Al}_2\text{O}_3$, respectively. The CS-23 and TEOS-23 samples with high content of alumina showed high bulk density values, this is explained by their high alumina amount use in preparation.

The skeletal density increases to $1400 \text{ }^\circ\text{C}$ with a small decrease to $1600 \text{ }^\circ\text{C}$ shown in Figure 4.13 and Figure 4.14. This is enabled by the increase in activation temperature, which compact particles leading to changes in size and shape of grains from primitive crystals structures with smaller grain sizes at lower temperatures to crystalline forms with larger grain sizes at higher temperatures, see Figure 2.4 and Figure 2.5 for crystalline crystal structures of cristobalite and mullite, respectively. A higher skeletal density of 3.7 g cm^{-3} was measured for the CS-23 sample sintered at $1600 \text{ }^\circ\text{C}$ linked to its high alumina content of 60 mol.-% and early densification temperature compared to the TEOS-23 sample with 56 mol.-% alumina represented by XRD measurements in Figure 4.11. The small decrease in the skeletal density from $1400 \text{ }^\circ\text{C}$ to $1600 \text{ }^\circ\text{C}$ is linked to liquid phase sintering which might have break down agglomerates reducing the particle sizes [66]. The elimination or reduction of pores is confirmed in all the samples by a decrease in porosity values following sintering of samples to $1600 \text{ }^\circ\text{C}$, see Figure 4.13 and Figure 4.14 [112].

The porosity was found to decrease with increasing sintering temperatures in both sample series, Figure 4.13 and Figure 4.14. In all samples porosity was found having pores with diameters of some microns as shown by the SEM, Figure 4.8 and Figure 4.9. Results from pycnometry and from the Archimedes principle revealed a porosity of 34 % for the TEOS-23 sample compared to 21 % for the CS-33 sample, while μ -CT investigations showed a porosity of 26 % for the TEOS-23 sample and 11 % for the CS-23 sample, both sintered at $1600 \text{ }^\circ\text{C}$ for 12 h. Figure 4.15 shows a three dimensional μ -CT reconstruction of the samples, and the pore distribution within the Al_2O_3 -mullite matrix is visible. From the differences in the porosity values as measured with both methods, it was deduced that there are pores in the samples which are below $1 \text{ }\mu\text{m}$ in diameter. This is the limit of the resolution of the μ -CT analyzer. This was also confirmed by mercury porometry. The pore diameters were in the range from $0.2 \text{ }\mu\text{m}$ to $7 \text{ }\mu\text{m}$ for the TEOS-23 sample and from $0.5 \text{ }\mu\text{m}$ to $5 \text{ }\mu\text{m}$ for the CS-23 sample, see Figure 4.16.

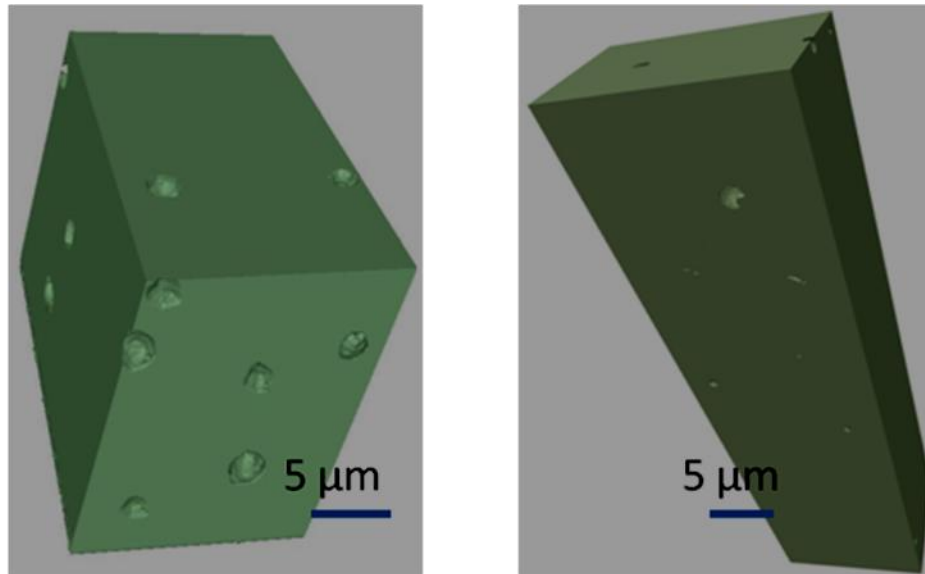


Figure 4.15: μ -CT 3D reconstruction of a “volume of interest” from alumina-mullite parts of TEOS-23 (left) and CS-23 (right) samples sintered at 1600 °C for 12 h

A total intergraded volume of $\sim 0.3 \text{ cm}^3 \text{ g}^{-1}$ was measured for the TEOS-23 sample compared to $\sim 0.1 \text{ cm}^3 \text{ g}^{-1}$ for the CS-23 sample. These differences were also found by the μ -CT 3D measurement of the samples shown in Figure 4.15, however, with the fidelity/limits of the μ -CT system. The typical mercury intrusion and expression behaviour is shown in Figure 4.16 for the TEOS-23 sample and the CS-23 sample (1600 °C, 12 h). These results include only those pores into which Hg can penetrate as a function of the applied pressure, and as a function of the nature of the pores: closed or open. The porosity analysis shows with all methods applied that it is higher in the TEOS-23 sample. The lowest porosity was measured with the μ -CT in both samples, but the values exceeded 10 % porosity. This is in accordance with the resolution of this method. If porosity can be measured by μ -CT, however, this qualifies this method to be used in the thermal cycling experiments as described in section 3.4.2 for non-destructive testing and data generation after each thermal cycle.

Table 4.3 shows the specific surface areas (SSA) for TEOS-23 and CS-23 samples sintered at 1200 °C and 1600 °C with a holding time of 12 h at peak temperature. The SSA was found to decrease with increase annealing temperatures. The surface area for the TEOS-23 sample decreased from $2.07 \text{ m}^2 \text{ g}^{-1}$ (1200 °C) to $0.75 \text{ m}^2 \text{ g}^{-1}$ (1600 °C) compared to $4.74 \text{ m}^2 \text{ g}^{-1}$ (1200 °C) to $0.36 \text{ m}^2 \text{ g}^{-1}$ (1600 °C) for the CS-23 sample. This is a consequence of the reaction/sintering process: pores are eliminated and the samples shrink. Both processes are responsible for the

reduction of the specific surface area. The obtained SSA values were smaller than specific surface area of $6.22 \text{ m}^2 \text{ g}^{-1}$ measured for $\alpha\text{-Al}_2\text{O}_3$ particles supplied. In comparison, a specific surface area of $\sim 19.5 \text{ m}^2 \text{ g}^{-1}$ was reported for mullite samples sintered at $1100 \text{ }^\circ\text{C}$ and was found to decrease to $\sim 1.5 \text{ m}^2 \text{ g}^{-1}$ when the sintering temperature was increased to $1350 \text{ }^\circ\text{C}$ [141]. Moreover, the specific surface area for mullite was observed in other investigations to decrease from $2.77 \text{ m}^2 \text{ g}^{-1}$ to $1.7 \text{ m}^2 \text{ g}^{-1}$ after calcinations at $1400 \text{ }^\circ\text{C}$ for 1 h [107]. A SSA value of approximately $0.8 \text{ m}^2 \text{ g}^{-1}$ and $0.4 \text{ m}^2 \text{ g}^{-1}$ is in good agreement with previous results due to high sintering temperature up to $1600 \text{ }^\circ\text{C}$ and with holding time of 12 h [140, 182].

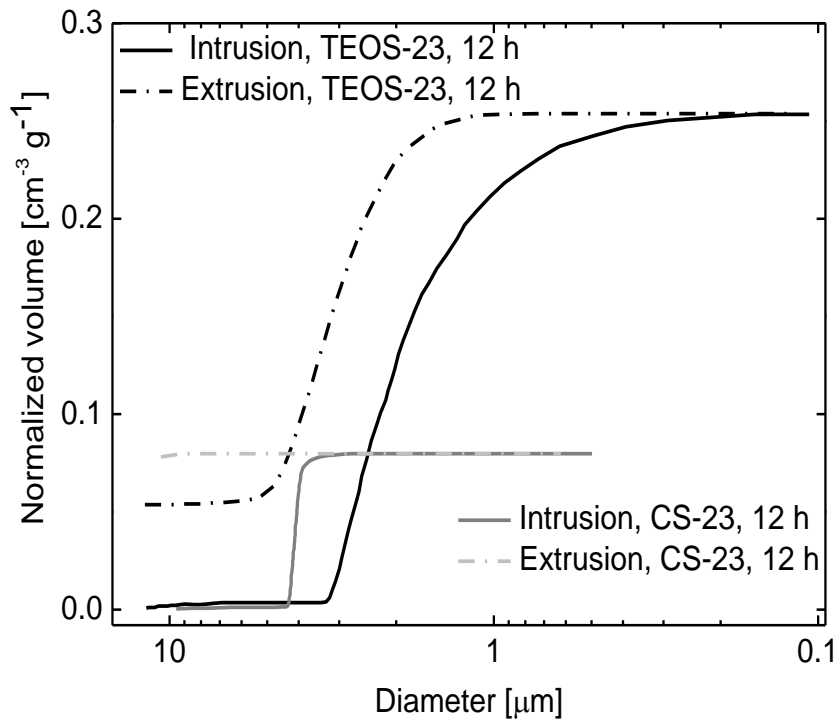


Figure 4.16: Typical intrusion and extrusion curves of the as synthesized alumina-mullite composites, samples are sintered at $1600 \text{ }^\circ\text{C}$ for 12 h

An increase in temperature from $1200 \text{ }^\circ\text{C}$ to $1600 \text{ }^\circ\text{C}$ caused an increase in bulk density with a corresponding decrease in porosity. Porosity decreases to $\sim 33 \%$ in the TEOS-23 sample compared to $\sim 34.4 \%$ in the CS-23 sample following sintering of samples to $1600 \text{ }^\circ\text{C}$. Densification behaviour is significantly different as shown by the plot of density against sintering temperatures, thus generating changes in the porosity, surface area and pore size of the produced samples [140]. The skeletal density of the samples decreased with increasing annealing temperature (see Appendix 16) and differs according to the amount of TEOS or CS

used in the sample preparation. The bulk density of all the samples increases from 1200 °C to 1600 °C with a corresponding decrease in the porosity. This is due to the mullitization and densification of the systems, see also DTA and XRD results in section 4.2 and 4.3, and refs. [7, 61]. The porosity is attributed to pores derived from elimination of residual by-products and heterogeneities in the particle sizes of alumina and mullite grains [66]. A low porosity of the CS-40 sample is attributed to a low amount of residual by-products: in TEOS four ethoxy groups and water leave the system while in the CS system only water is released when the sample is heated for drying [89]. TEM analysis was carried out to identify crystalline and amorphous components, since XRD has limitations in the identification of amorphous phase and is not able to localize the phases.

Table 4.3: Specific surface area (SSA), pore size diameter and intruded volume of mullite-alumina samples

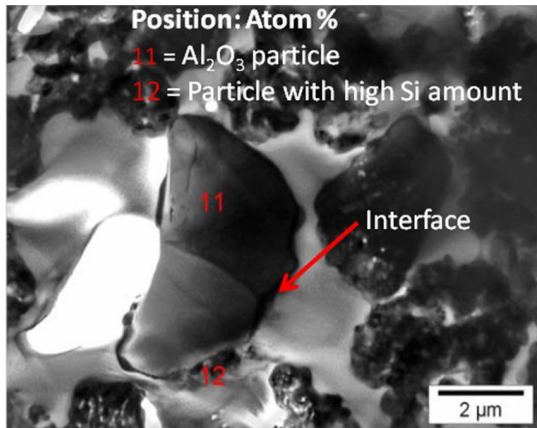
Property and sintering temperature	TEOS-23	CS-23
SSA ($\text{m}^2 \text{g}^{-1}$), 1200 °C, 12 h	2.07	4.74
SSA ($\text{m}^2 \text{g}^{-1}$), 1600 °C, 12 h	0.75	0.36
Pore size diameter (μm), 1600 °C, 12 h	0.2-7.0	0.5-5.0
Intruded volume ($\text{cm}^3 \text{g}^{-1}$), 1600 °C, 12 h	~ 0.3	~ 0.1

4.3.3 TEM analysis

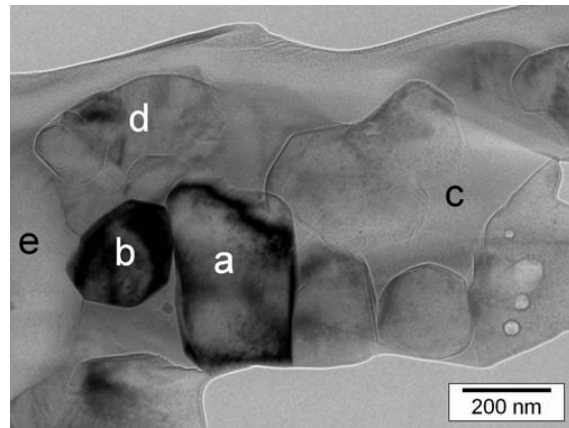
TEM micrographs and EDX spot analysis for TEOS-23 and CS-23 derived samples are shown in Figure 4.17 to Figure 4.19. The results of the EDX spot analysis are listed in Appendix 17 to Appendix 23. It should be noted, that the balance in mol.-% for Al, Si and O atoms is the percentage of carbon which originates from the resin infiltration of the samples.

In Figure 4.17 (i), the EDX spot analysis of the TEOS-23 sample at position 12 (30 Al + 15 Si + 20 O) shows a particle with a comparatively high Si amount having a composition close to that of mullite along the rim covering an inner Al_2O_3 particle in position 11 (78 Al + 20 O). The composition of position 12 indicates the start of the mullite formation at ~1200 °C; in the sample TEOS-23 this was found by XRD first at 1300 °C. A similar shift was also found for the TEOS-77 and CS samples. These findings are in accordance with results found by MAS NMR

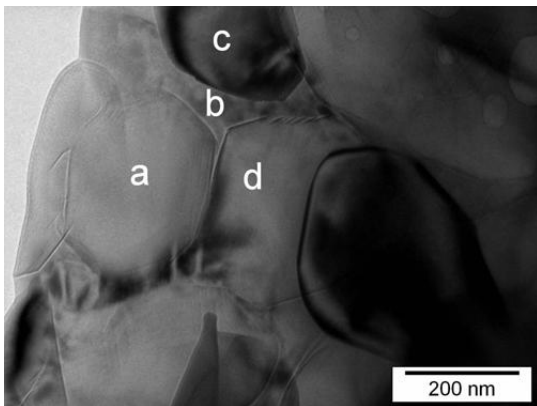
spectroscopy studies for diphasic gels which revealed nucleation and mullitization/crystallization between 1000 °C to 1200 °C according to [83, 131, 133].



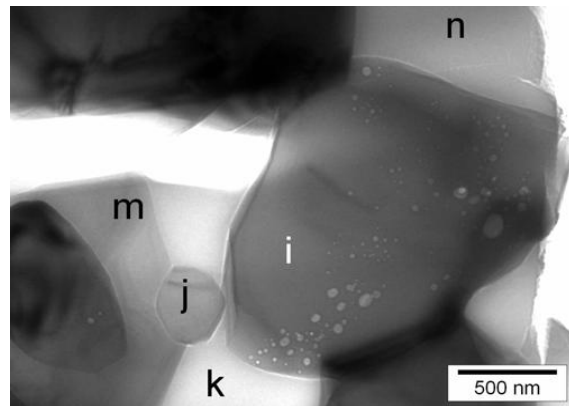
(i) Al₂O₃ particle encircled by high Si amount, (1200 °C, 3 h)



(iii) Crystalline (a-d) and amorphous region (e), (1600 °C, 3 h)



(ii) Mullite (b) between two Al₂O₃ particles (a, c) at triple junction, (1600 °C, 3 h)



(iv) Mullite (j, m), Al₂O₃ (i) un-reacted close to amorphous region (n), (1600 °C, 12 h)

Figure 4.17: TEM images and marks of EDX spot analysis from the TEOS-23 derived sample

Figure 4.17 (iii) shows a TEM micrograph of the sample TEOS-23 after sintering at 1600 °C for 3 h. EDX spot analysis (see Appendix 18) revealed high aluminium and high oxygen concentrations (a: 31 Al + 63 O, b: 27 Al + 66 O) indicating both particles are alumina. Analysis of spot c showed an elemental composition of 3 Al + 14 Si + 47 O of d: 8 Al + 15 Si + 58 O and of e (2 Al + 15 Si + 52 O). Spot c and d were identified to be a crystalline phase, and it was deduced that the compositions are close to that of the mullite composition. Region e was identified to be amorphous, cf. also ref. [132]. Figure 4.17 (ii) shows a different arrangement of

several phases, a (35 Al + 63 O) and c (32 Al + 58 O) are close to the theoretical composition of plain alumina while b (10 Al + 15 Si + 69 O) and d (22 Al + 6 Si + 58 O) contain Al:Si ratios which point out the formation of mullite.

An increase of the holding time to 12 h at 1600 °C, as presented in, Figure 4.17 (iv) showed compositions close to that of mullite (m) and alumina (i ,j) with an amorphous phase spot n: 2 mol.-% Al, 0.3 mol.-% Si and 27 mol.-% O (see also Appendix 20). XRD Rietveld estimates indicate complete mullitization for the TEOS-23 sample at 1600 °C, but TEM-EDX spot analyses revealed a residual amorphous phase even at a holding time of 12 h [3]. TEM investigations of the TEOS-23 sample showed a shift of the onset of the mullitization to occur at lower temperatures, and samples sintered at 1600 °C revealed the presence of an amorphous glass phase. The amorphous glass may arise from inhomogeneity in precursors forming agglomerates which persist to high temperatures or from interface barriers between Al₂O₃-mullite-SiO₂ phases [74, 132]. Similar amorphous phases were observed following the reaction sintering of α-alumina and cristobalite at 1625 °C, which is described in [72].

Figure 4.18 shows a TEM image and a spot analysis of the TEOS-77 sample after sintering at 1600 °C for 12 h. The elemental compositions are as follow: a: 33 Al + 9 Si + 58 O, b: 33 Al + 8 Si + 59 O, d: 30 Al + 8 Si + 61 O, which is close to the composition of mullite, and the composition of the amorphous phase is c: 3 Al + 29 Si + 68 O and e: 4 Al + 27 Si + 68 O. Spot c reveals a high amount of Si, Figure 4.18 (ii) which is almost pure cristobalite. This was confirmed by XRD analysis, see Figure 4.11 (c) having a total amount of ~24 mol.-% of cristobalite The presence of cristobalite in this sample is related to the high amount of TEOS used in its preparation, see Figure 2.1.

From the TEOS series, TEM and XRD confirmed large residual amounts of silica in the TEOS-77 sample prepared with a SiO₂-to-Al₂O₃ molar ratio of 3.4:1. In the TEOS-23 sample an amorphous glass phase was found [60]. Processing with the TEOS-77 composition represents mullite and cristobalite phases while TEOS-23 shows an alumina and a mullite phase. XRD showed 2 mol.-% Al₂O₃ in the TEOS-77 sample sintered at 1600 °C. It appears to be isolated or enclosed within crystalline mullite as a result of growth of mullite crystals [73]. The kinetics of the mullite formation reaction revealed mullite formed at the interface between Al₂O₃ and SiO₂

leading to the formation of reaction barriers resulting in 2 mol.-% of alumina and an amorphous glass phase [61, 132].

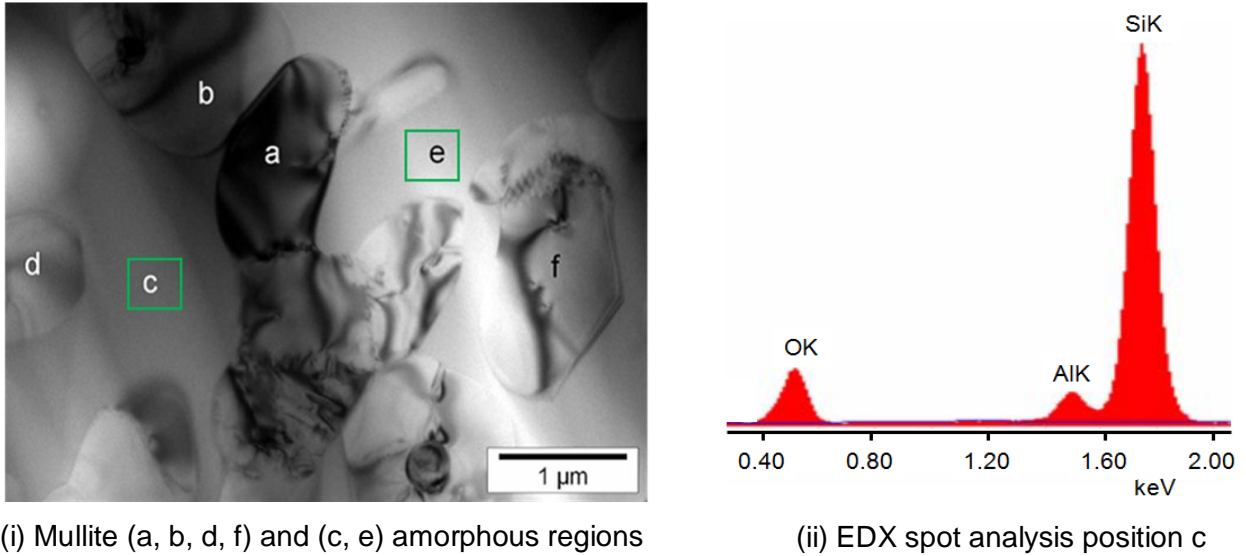


Figure 4.18: TEM image and marks of EDX spot analysis for TEOS-77 derived mullite sample sintered at 1600 °C for 12 h holding time

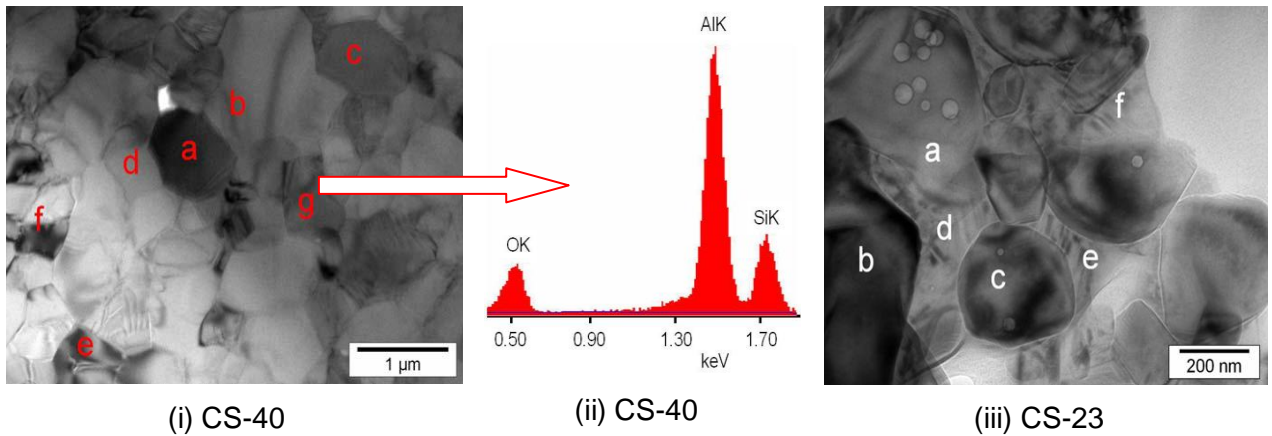


Figure 4.19: TEM images and EDX spot analysis of CS samples sintered at 1600 °C for 12 h holding time, (ii) EDX-spectrum of position g with high Al mol.-%

Different crystalline phases were identified possessing compositions as follow: a: 34 Al + 8 Si + 58 O, b: 34 Al + 8 Si + 59 O, c: 34 Al + 8 Si + 58 O, d: 30 Al + 7 Si + 63 O, e: 30 Al + 6 Si + 64 O, f: 31 Al + 7 Si + 62 O). These compositions point out the formation of mullite. Alumina was found at spot g: 42 Al + 57 O, in the sample CS-40 Figure 4.19 (i). Figure 4.19 (iii) represents a

different arrangement with phases of alumina (a: 37 Al + 62 O, b: 42 Al + 57 O; c: 42 Al + 56 O) and mullite (d: 17 Al + 14 Si + 65 O), and region f was identified to be close to an amorphous glass composition constituting 5 mol.% Al + 21 mol.% Si + 62 mol.% O, as found in the CS-23 sample. This is comparable to the TEOS-23 sample.

The CS-40 sample (see Figure 4.22 (i)) showed an Al_2O_3 particle at position g, and the microstructure appears to be similar like the microstructure of the sample CS-23. In XRD measurements a phase composition was found with 2 mol.% of alumina and 98 mol.% of mullite found in the CS-40 sample; in the CS-23 sample the phase composition was found to be 60 mol.% of alumina and 40 mol.% of mullite, see also Figure 4.11 (b, d). The 2 mol.% alumina found in the CS-40 sample might be unreacted due to a diffusion barrier as described for the TEOS-77 sample above [22].

An amorphous glass phase was found in position f with high silicon amount similar to the amorphous glass phase found in the TEOS-23 sample. Compositions prepared from Al_2O_3 -to- SiO_2 molar ratio of 3.4:1 (TEOS-23 and CS-23 samples) formed phases of alumina-mullite in accordance with the phase diagrams [13, 18]. A difference of 4 mol.% mullite was found in the TEOS-23 sample sintered at 1600 °C, as compared to the CS-23 sample [82]. The high degree of mullitization of the TEOS-23 sample is related to its almost complete densification prior to the mullitization onset. This is reflected in the peak intensities for mullite in the XRD patterns for TEOS-23 sample (see Appendix 12) and CS-23 sample (see Appendix 13).

4.4 Material properties

4.4.1 Mechanical properties

Figure 4.20 to Figure 4.23 represent the Vickers hardness, the flexural strength, for samples sintered from 1200 °C to 1600 °C; the Weibull (M) distribution and the failure probability is shown for samples sintered at 1600 °C for 12 h. The flexural strength for fired samples at 1600 °C were determined at 25 °C, at 500 °C and at 1000 °C with the three point bending model, see Figure 4.24.

The Vickers hardness for TEOS-23 and CS-23 samples is shown in Figure 4.20 and details are listed in Appendix 24. The hardness of samples sintered from 1200 °C increases and shows a

maximum at 1400 °C. This was also found in [3]. The CS-23 sample possesses a high Vickers hardness compared to the TEOS-23 sample. The indentation test showed a high variability degree of scattering of the micro-hardness values. The scatter in the values of the samples arises from pores and inhomogeneities. The decrease in micro-hardness from 1400 °C to 1600 °C is small, a value of ~9 GPa was obtained for the CS-23 sample and ~5 GPa for the TEOS-23 sample. The values are lower than those of dense mullite showing 15 GPa at room temperature. For comparison, a Vickers hardness for alumina-mullite range from 9.2 GPa to 11.6 GPa [180].

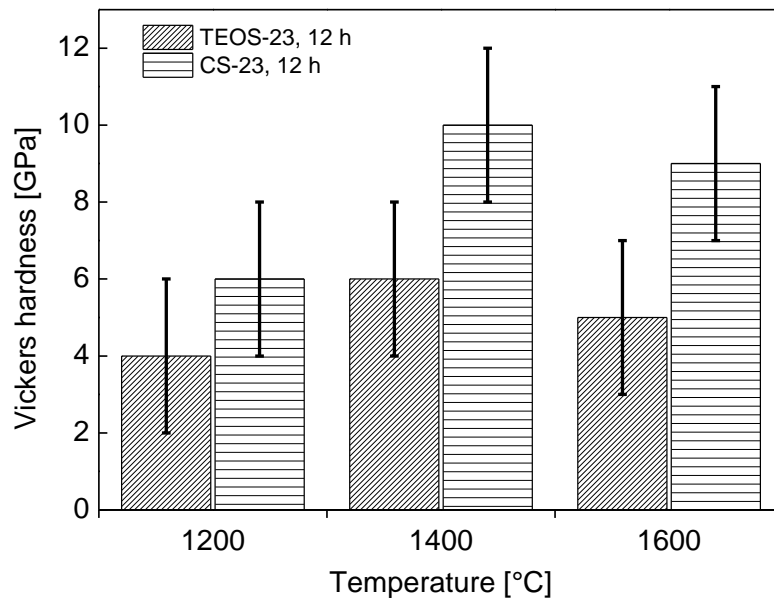


Figure 4.20: Vickers-hardness as a function of sintering temperature; samples sintered at 5 K min⁻¹ with holding times of 12 h at peak temperature

In Figure 4.21, the flexural strength (σ_f) for samples sintered from 1200 °C to 1400 °C increased up to 1400 °C and decreased slightly to 1600 °C. The CS-23 sample has a higher flexural strength as compared to the TEOS-23 sample; differences were observed for samples sintered for 3 h and 12 h holding times. The flexural strength for the TEOS-23 sample sintered for 3 h was found to be in the range from 12 MPa to 28 MPa. The CS-23 sample has a strength maximum at 1400 °C, and the strength decreases to 101 MPa at 1600 °C, see also [145].

The TEOS-23 sample sintered for 12 h represents an increase in flexural strength from 1200 °C to 1400 °C and decrease to ~6 % at 1600 °C, which was also found in [140]. A similar trend was observed for the CS-23 but with a decrease of ~5 % at 1600 °C. The initial low strength for the

samples sintered at 1200 °C is related to the high porosity, the low density and the almost unreacted and unsintered state of the sample, see also Figure 4.8. The increase of the flexural strength for samples sintered at 1400 °C is enabled by two factors: the formation of mullite from the starting components and the ongoing sintering process with its resulting microstructure. In spite of the decrease of the porosity of samples sintered at 1400 °C and at 1600 °C, the flexural strength decreases from 1400 °C to 1600 °C. This effect was assigned to the silica phase, which is still present as a glass.

Table 4.4: Mechanical properties of the samples TEOS-23 and CS-23, both sintered at 1600 °C for 12 h

Sample	Vickers hardness [GPa]	Flexural strength σ_0 [MPa]	Weibull parameter (m)	Young's modulus [GPa]
TEOS-23	5±2	33.8±5	7.7	27±2
CS-23	9±2	99.5±14	7.6	49.2±2

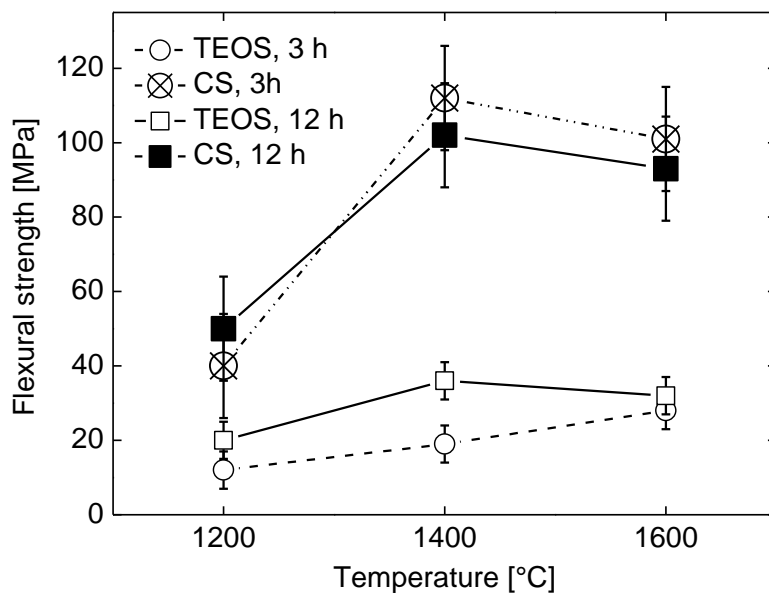


Figure 4.21: Flexural strength of the samples TEOS-23 and CS-23 after firing at 1600 °C for 3h and for 12 h

The variations in the flexural strength values shown in Figure 4.21 were evaluated using the Weibull statistics to determine the threshold strength (σ_0) for the samples. The Weibull plot and the failure probability of samples are shown in Figure 4.22 and Figure 4.23. The plot of $\text{Ln}[\ln(1/1-$

$\text{Ln}[\ln(1/1-P_f)]$ versus the fracture stress ($\text{Ln}\sigma_i$) provided the Weibull parameter (m) as the slope of the straight line. The threshold stress (σ_0) from the location of the line was obtained when $\text{Ln}[\ln(1/1-P_f)] = 0$. The failure probability was evaluated from the flexural strength (σ_i), the Weibull parameter (m) and the threshold stress (σ_0) according to Eqn. (3.10). Weibull parameters m of 7.7 and 7.6 were calculated for the TEOS-23 and CS-23 samples, respectively. Both sample series were sintered at 1600 °C for 12 h. The threshold strength (σ_0) of 33.8 MPa was obtained for the TEOS-23 sample and 99.5 MPa for the CS-23 sample, see Table 4.4. These values were used with the flexural strength values to obtain the failure probability in Figure 4.23, and details are given in Appendix 26

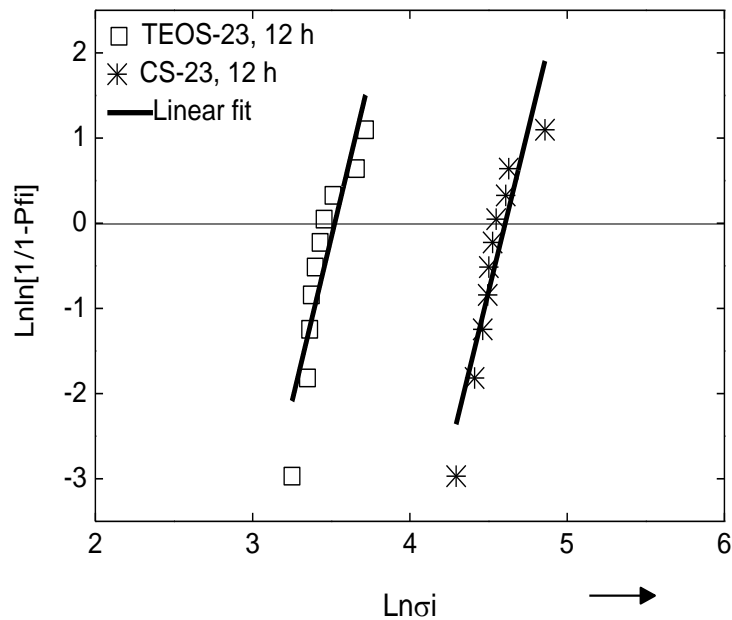


Figure 4.22: Weibull plot for TEOS-23 and CS-23 alumina-mullite samples sintered at 1600 °C with 12 h holding times

The data set of the alumina-mullite ceramics for the cumulative probability of failure [$\text{Ln}[\ln(1/1-P_f)]$ versus the fracture stress ($\text{Ln}\sigma_i$) do not lie on a straight line for both samples. This indicates some heterogeneity in microstructure originating from pores, grain boundaries and alumina-mullite interfaces. This is also in good agreement of the scattering behaviour in the Vickers hardness values in Figure 3.3 and with SEM images as shown in Figure 4.8. It was found that, at strength values of 33.8 MPa (TEOS-23) and 99.5 MPa (CS-23) approximately 63 % of the samples failed, see Figure 4.23, details are shown in Appendix 26.

The degree of scattering in the flexural strength values for the TEOS-23 (i.e. 33.8 ± 5 MPa) sample is less compared to the CS-23 sample (i.e. 99.5 ± 14 MPa). The CS-23 sample, however, represents a higher strength. This results in a Weibull parameter of 7.7 for the TEOS-23 sample and of 7.6 for the CS-23 sample. From the engineering point of view, Weibull parameters obtained in this analysis from 7.6 to 7.7 lies in the range of calculated m values for ceramic reported from 5 to 20 [40]. Weibull parameters in the range from 4.4 to 13.6 were reported for sol-gel derived mullite ceramics, see Table 2.4 [135]. The data show less scattering.

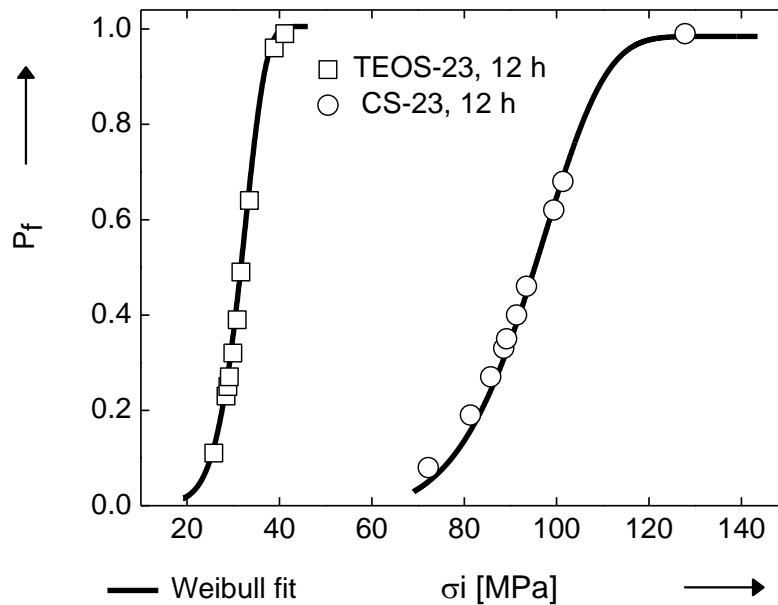


Figure 4.23: Weibull distribution plot with probability of failure for TEOS-23 and CS-23 samples sintered at 1600 °C for 12 h holding times

The differences in the strength values may be related to the interactions of the different components of the microstructure: pores, ceramic phases (alumina, mullite, glass phase) and their grain size distribution and grain boundaries. Less strength of the TEOS-23 sample may originate from its high porosity (34 %). The relation between the flexural strength and the porosity (21% to 34 %) is shown in Eqn.(4.1), which was also shown for samples investigated in [139]. The difference of 4 mol.-% alumina in the CS-23 obtained at 1600 °C might have increased its flexural strength. Mullite ceramics are reported to retain ~90 % of its flexural strength at 1500 °C and reduce its flexural strength on further heating. A similar trend was shown by the samples studied in [183]. Aksel [181] observed a porosity of 23 % and 25 % with

slip-cast alumina-mullite ceramics having a flexural strength of 10 MPa and 8 MPa, respectively. The higher strength reported in the produced alumina-mullite sample is associated with the homogeneous process of the sol-gel method with ball milling and the difference in the alumina amount [7].

$$\sigma_{fs} = \sigma_0 \exp(-nP) \quad (4.1)$$

where σ_{fs} is the flexural strength of the porous material, P is the porosity, σ_0 is flexural strength of the non-porous ceramic and n is the experimental constant.

The calculated Young`s moduli are shown in Table 4.4. A low Young`s modulus of 27 GPa was obtained for the TEOS-23 sample compared to 49 GPa for the CS-23 sample. This is similar to the differences in flexural strength values presented above. In comparison, a Young`s modulus of 410 GPa is reported for dense alumina compared to 144 GPa for dense mullite [40]. Moreover, a flexural strength value of 10 MPa with a Young`s modulus of 9.7 GPa are reported for alumina-mullite ceramics in [181].

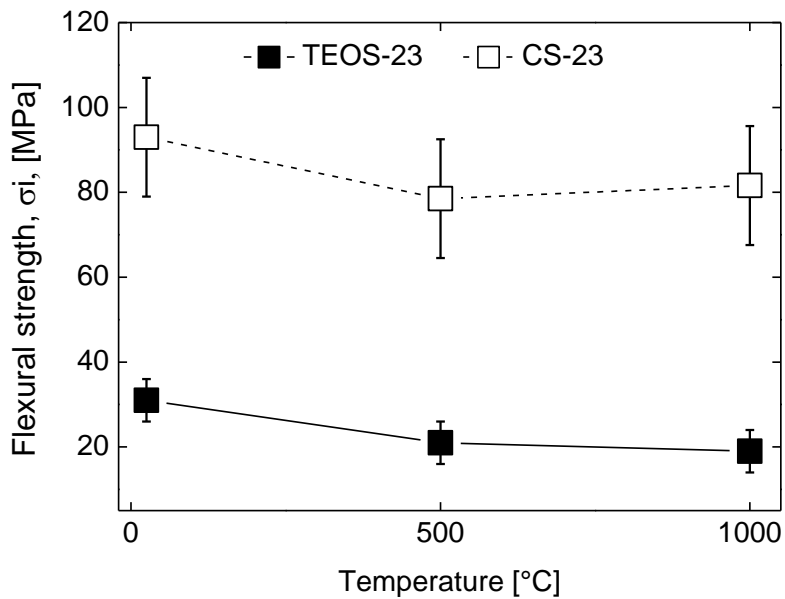


Figure 4.24: Flexural strength at 25 °C, 500 °C and 1000 °C of TEOS-23 and CS-23 samples sintered at a temperature of 1600 °C for 12 h

Figure 4.24 shows the results of the three point bending test performed on samples previously fired at 1600 °C for 12 h. The first sample was tested at 25 °C, the second at 500 °C and the third at 1000 °C. Measurements were conducted at a heating rate of 5 K min⁻¹ with a holding time of 30 minutes before the load was applied. This was carried out to achieve temperature uniformity. A drop in flexural strength with increasing temperature was observed for all the samples. The flexural strength versus the temperature plot displays a drop in strength at 500 °C. The strength decrease was approximately 25 % for the TEOS-23 sample and ~7 % for the CS-23 ceramic sample. Some authors reported that an increase in the temperatures stimulates the thermal vibrations of the material's constituents resulting in a change of the tetrahedral and octahedral angles. This leads to the formation of point's defects followed by expansion weakening of the chemical bonds. A consequence is the reduction of the strength of the materials [1, 129].

4.4.2 Thermal properties

Figure 4.25 and Figure 4.26 shows the thermal properties of the as-sintered alumina-mullite ceramics measured from room temperature to 1000 °C, for details see Appendix 27 and Appendix 28.

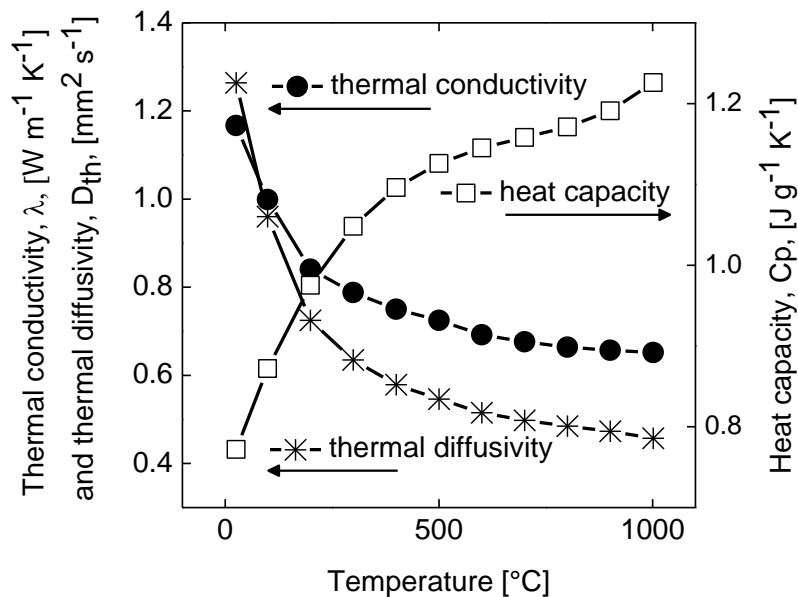


Figure 4.25: Thermal behaviour of heat treated TEOS-23 alumina-mullite ceramic samples after sintering at 1600 °C for 12 h, λ: thermal conductivity, C_p: Heat capacity and D_{th}: thermal diffusivity

The thermal conductivity values for TEOS-23 and CS-23 alumina-mullite samples were found to decrease with increasing temperature and are almost constant from above 800 °C to 1000 °C [149]. The thermal conductivity of the TEOS-23 ceramic decreases from 1.17 W m⁻¹ K⁻¹ to 0.65 W m⁻¹ K⁻¹ compared to 5.56 W m⁻¹ K⁻¹ to 3.21 W m⁻¹ K⁻¹ for the CS-23 sample [134]. A high thermal conductivity value was measured for the CS-23 sample. The differences in the values may be explained by their differences in porosity and by the different silica precursor used for the sample preparation. From this result, a high density CS-23 sample possesses the highest thermal conductivity. This correlates with its bulk density of 2.9 g cm⁻³ compared to the TEOS-23 sample with a density of 2.3 g cm⁻³. In comparison, the thermal conductivity of dense mullite ceramic is reported to decrease from 6 to 4 W m⁻¹ K⁻¹ [152]. The average thermal conductivity of dense mullite is shown in blue dotted lines in Figure 4.26. A lower thermal conductivity was measured for both ceramic samples which are related to their porosity [134].

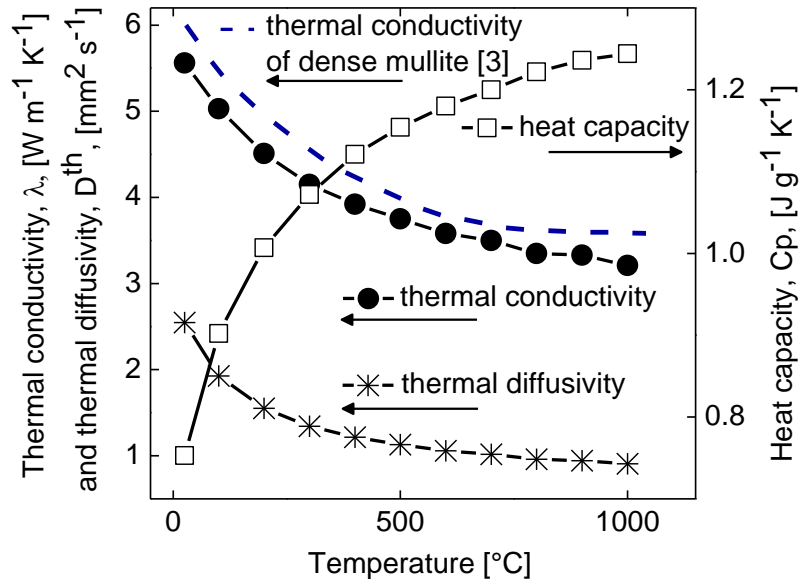


Figure 4.26: The thermal behaviour of heat treated CS-23 alumina-mullite ceramic samples after sintering at 1600 °C with holding time of 12 h. λ : thermal conductivity, C_p : heat capacity and D_{th} : thermal diffusivity

The specific heat capacity increases from 100 °C to 1000 °C with a corresponding decrease in thermal diffusivity. A specific heat of 1.22 J g⁻¹ K⁻¹ (TEOS-23) and of 1.24 J g⁻¹ K⁻¹ (CS-23) was found at 1000 °C. The specific heat is reported to be influenced by the material's porosity, grain size and shape. In comparison, the specific heat of 1.26 J g⁻¹ K⁻¹ is reported for dense mullite at 1000 °C compared to 1.25 J g⁻¹ K⁻¹ for dense Al₂O₃ [40]. Similar decrease in thermal diffusivity

and increase in heat capacity values for mullite ceramics are reported in [53, 146]. The TEOS-23 alumina-mullite sample with high porosity represents a small thermal conductivity and a small specific heat. The thermal conductivity has been reported to depend on the content of pores according to Eqn. (4.2) [134].

$$\lambda_p = \lambda(1 - V_p) \quad (4.2)$$

where λ is the value for dense material and V_p is the porosity

Figure 4.27 shows the linear thermal expansion behaviour of samples sintered at 1600 °C for 3 h and 12 h holding times.

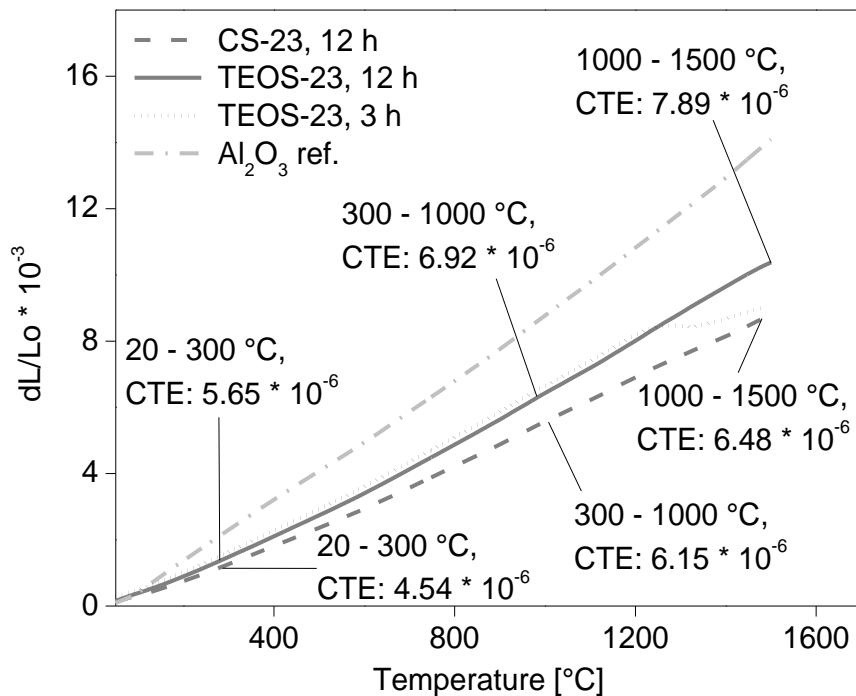


Figure 4.27: Linear coefficient of thermal expansion of TEOS-23 and CS-23 samples sintered at 1600 °C for 3 h and 12 h

Dilatometer measurement showed a linear and a non linear increase in the thermal expansion from room temperature to 1500 °C [150]. The TEOS-23 ceramic sample sintered at 1600 °C for 3 h showed a linear increase in the CTE to approximately 1250 °C. Above this temperature, its length decreases by ~1 % of its original length and its CTE shows a non-linear behaviour and increases to 1500 °C. The TEOS-23 and CS-23 samples sintered for 12 h at 1600 °C show a

linear increase in the CTE from 20 °C to 1500 °C. At a maximum of 1500 °C, a linear CTE of $6.9 \times 10^{-6} \text{ K}^{-1}$ was measured for the TEOS-23 sample compared to $6.4 \times 10^{-6} \text{ K}^{-1}$ for the CS-23 sample, respectively, see also ref. [152].

The TEOS-23 ceramic sample sintered at 1600 °C for 3 h, showed a non-linear behaviour in its CTE above 1250 °C. This behaviour might be assigned to the amorphous glass phase determined from XRD measurements, which appear as a non-reacted component in the composite material. By heating during thermal expansion measurements, the un-reacted glass phase (see Figure 4.17) may react with alumina resulting in a decrease in bulk volume. This effect was not found in TEOS-23 and CS-23 samples sintered at 1600 °C for 12 h. Mullite is reported to show an average linear thermal expansion coefficient from $4.5 \times 10^{-6} \text{ K}^{-1}$ to $7.5 \times 10^{-6} \text{ K}^{-1}$ in the temperature range from 200 °C to 1600 °C [150, 152]. The thermal expansion of mullite is relatively low compared to that of $\alpha\text{-Al}_2\text{O}_3$, which is in the range of $5.4 \times 10^{-6} \text{ K}^{-1}$ to $9.5 \times 10^{-6} \text{ K}^{-1}$ [37, 149]. It must be noticed that the values obtained in this work are located at the midpoint of the average for mullite and alumina CTE as reported in [168].

The linear coefficient of thermal expansion for the CS-23 ceramic sample is low compared to a higher value measured for the TEOS-23 sample. This effect is not clear yet. However, the amorphous phase found in the TEOS-23 sample, its high porosity and its microstructure influence its CTE. The differences in the CTE of the TEOS-23 and the CS-23 sample may originate from the different silica source used and their final alumina amount. Schneider et al [53] observed that the composition which controlled the expansion of Al octahedral, Al tetrahedral and oxygen vacancies distribution is associated with the Al_2O_3 content of mullite and increases the CTE of mullite differently in the corresponding lattice, see Appendix 1. This might be a possible reason for the observed increase in the linear CTE of the ceramic samples since they contain mullite and alumina. The low thermal expansion coefficient of these materials may be associated with a good resistance to thermal shock [37, 38].

4.5 Thermo-shock behaviour

The thermo-shock behaviour of the produced alumina-mullite ceramics was evaluated based on the thermophysical data obtained in this work and by tracing crack growth after a thermo-shock with non-destructive $\mu\text{-CT}$.

In the first method the critical temperature difference for expected failure (ΔT) and the thermal shock resistance to fracture initiation by thermal stresses (R_s) were calculated based on the threshold strength, the Young's modulus, the coefficient of thermal expansion and the thermal conductivity values determined at room temperature. A Poisson's ratio of 0.2 for mullite ceramics found in the literature was used [40]. The thermophysical data and calculated ΔT and R_s values for TEOS-23 and CS-23 (both sintered at 1600 °C for 12 h) are listed in Table 4.5.

Table 4.5: Evaluated parameters

Properties	TEOS-23	CS-23
porosity [%]	34	21
micro-hardness at room temperature, [GPa]	5±2	9±2
bending strength at room temperature, σ_o , [MPa]	33.8±5	99.5±14
Young's modulus at room temperature, E, [GPa]	27	49.9
coefficient of thermal expansion from 20 °C to 1573 °C, $\cdot 10^{-6}$, [K ⁻¹]	5.65-6.97	4.54-6.48
Density, ρ_b , [g cm ⁻³]	2.3±0.2	2.9±0.2
thermal conductivity from room temperature to 1000 °C, λ , [W m ⁻¹ K ⁻¹]	1.17-0.65	5.56-3.22
heat capacity from room temperature to 1000 °C, [J g ⁻¹ K ⁻¹],	0.77-1.23	0.75-1.24
thermal diffusivity from room temperature to 1000 °C, [mm ² s ⁻¹]	1.26-0.46	2.55-0.91
critical temperature difference for expected failure (ΔT), [K]	177.25	351.36
thermal shock resistance to fracture initiation by thermal stresses (R_s), [kW m ⁻¹]	0.21	1.95

A critical temperature difference of 351 K and thermal shock parameter R_s of 1.95 kW m⁻¹ was obtained for the CS-23 ceramic sample, and 177 K and 0.21 kW m⁻¹ for the TEOS-23 sample, respectively. The high value of the CS sample might be related to the high flexural strength of the CS sample having a value of 99.5 MPa; the value of the TEOS sample is 33.8 MPa. The increase in the critical temperature difference might be related to the high level of porosity in the range of 21 % to 34 %; a porosity of 23 % to 25 % was reported for slip-cast alumina-mullite in ref. [181]. Other authors reported similar thermal shock temperature difference from 181 K to 215 K and thermal shock sensitivity values ranging from 1.40 kW m⁻¹ to 1.56 kW m⁻¹ for porous

corundum-mullite [180]. However, a direct comparison cannot be given due to differences in the starting materials and the resulting differences in the microstructure.

In the second approach, a μ -CT was used to image the alumina-mullite samples, which were thermally shocked following 5, 10, 15 and 20 cycles of heating to 1200 °C (5 K min⁻¹). The density values of the as-shocked and dried samples (500 °C, 3h) are listed in Table 4.6 and Table 4.7. No significant changes were observed for the measured density values confirming material stability during rapid thermal expansion and contraction.

Table 4.6: Density of the CS-23 sample heat treated at 1600 °C for 12 h and quenched in water following 20 cycles

Thermal shock cycles	Height [mm]	Length [mm]	Width [mm]	Mass [g]	Density [g cm⁻³]
0	2.00	6.00	3.00	0.1064	2.9555
5 (1000 °C)	1.99	6.01	2.99	0.1065	2.9781
10 (1000 °C)	1.99	6.00	2.99	0.1064	2.9803
15 (1000 °C)	1.98	6.01	3.00	0.1065	2.9832
20 (1200 °C)	1.98	6.01	2.99	0.1065	2.9932

Table 4.7: Density of the TEOS-23 sample heat treated at 1600 °C for 12 h and quenched in water following 20 cycles

Thermal shock cycles	Height [mm]	Length [mm]	Width [mm]	Mass [g]	Density [g cm⁻³]
0	2.00	6.00	3.00	0.0835	2.3194
5 (1000 °C)	2.01	6.00	2.99	0.0836	2.3183
10 (1000 °C)	2.01	5.99	3.00	0.0836	2.3145
15 (1000 °C)	2.01	5.99	3.01	0.0835	2.3040
20 (1200 °C)	2.01	6.00	3.01	0.0836	2.3029

The samples were inspected by μ -CT before and after thermal cycling. The TEOS-23 alumina-mullite ceramic sample returns its shape and stability after 20 thermal cycling tests to 1200 °C, see Figure 4.28 (top). A thermally induced crack was identified by μ -CT analysis in the CS-23 sample after the fifth cycle and it was found that the crack propagates less continuously during

the 10th and 20th thermal cycles, see Figure 4.28 (bottom). Figure 4.28 shows the samples before (a, b), and after 5th (b, e) and 20th (c, f) cycles. Pictures of samples tested with different sizes are shown in Figure 4.29.

The TEOS sample showed fast absorption of water compared to the CS sample resulting in bubbles some seconds after the sample was thermally shocked in water. This is a hint to the high porosity and pore shape: it is believed that this sample possesses ink-bottle shaped pores. The CS-23 sample, however, is less sensitive to thermal shock. These differences are illustrated in the μ -CT 3D images from the TEOS-23 and from the CS-23 sample. The TEOS-23 sample with a porosity of 34 %, a total pore volume of 0.3 cm³ g⁻¹ and pore diameters in the range from 0.2 μ m to 7 μ m presents good thermal shock behaviour with no crack after thermal cycling. The CS-23 sample, however, is significantly more sensitive to crack formation during thermal cycling. Its porosity is smaller (21 % with a total pore volume of 0.1 cm³ g⁻¹) and pore diameters ranging from 0.5 μ m - 5 μ m.

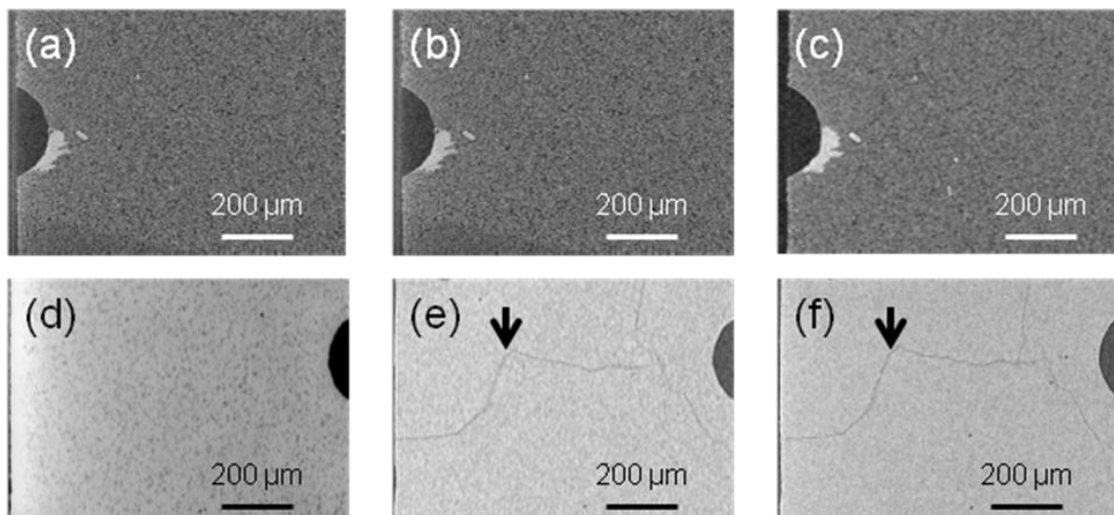


Figure 4.28: μ -CT slices of the alumina-mullite ceramic samples after sintering at 1600 °C for 12 h; (top: TEOS-23; bottom: CS-23 sample) thermally shocked from 1000 °C to 1200 °C and quenched with water. Images of sample before (a, d) after 5th (b, e) and 20th (c, f) thermal cycle

Samples with different dimensions were also tested and imaged before and after the 10th and 20th cycles, see Figure 4.29. The sample size represents different temperature behaviours (ΔT) when thermally shocked. Smaller samples as shown in Figure 4.29 (c, d) with a maximum

thickness of 2 mm withstand 20 cycles of thermal shock compared to 10 cycles for samples with a larger size, as shown in Figure 4.29 (a, b). The CS-23 sample represents less stability to thermal shock compared to the TEOS-23 sample, identified in both small and large samples. Hence, increase in size of samples reduces the thermal stability, and the CS-23 sample with large size crumbles into smaller particles during the 10th cycle (see Figure 4.29 (b)). Sample pictures after the 20th cycle did not showed cracks, but μ -CT detected a crack in the CS sample already after the 5th cycle.

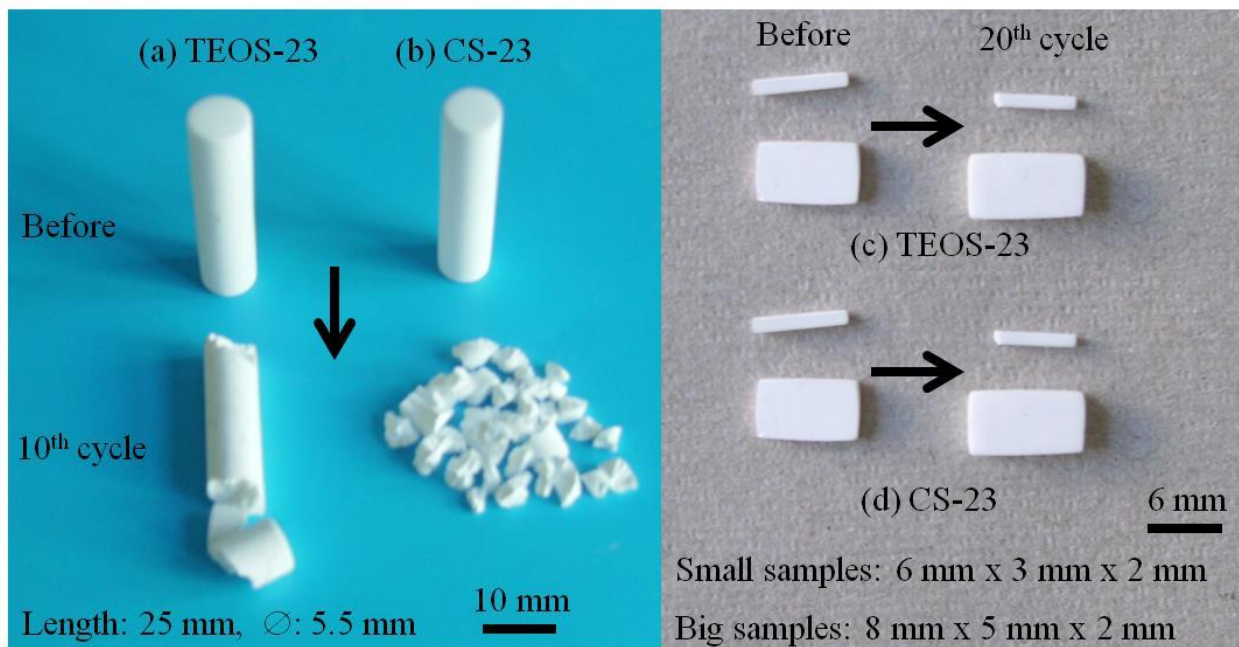


Figure 4.29: Pictures of TEOS-23 and CS-23 samples with different dimensions thermally shocked

The crack formation started during the 5th thermal cycle for the CS-23 sample. Computed values based on experimental data, cf. Table 4.5, revealed a critical temperature difference of 351 K and a thermal shock resistance of 1.95 kW m⁻¹ for the CS-23 sample. For the TEOS-23 sample values of 177 K and 0.21 kW m⁻¹ were computed, respectively. In the TEOS-23 sample no cracks were found. This is, however, in contradiction to the expected thermo shock behaviour. Both, the amorphous/crystalline phases as well the porosity influence the thermo shock behaviour in a complex manner. Both sample series showed mullite formation and residual alumina; both components have been quantified. However, the amount of the remaining glassy phase is not known. Moreover, the thermal properties of the glassy phase are still unknown.

Thus, it is not possible yet to develop a model which describes the thermo mechanical behaviour of this system. It might be plausible, that the amount of sodium ions remaining in the CS system (1.78 mg l^{-1}) influences the phase formation a) during mullitization and b) while being dissolved within the silica matrix. This provides uncertainties in the prediction of the composition of the microstructure, and consequently no modelling of the thermo mechanical behaviour is possible.

The overall performance of the alumina-mullite ceramics depend on their microstructure: the phase amount of crystalline phases (mullite, alumina), the phase amount of amorphous phases, the grain boundaries, the homogeneity of the phase distribution and the porosity (the shape of pores, the pore size distribution and the number of pores) influence the thermo mechanical properties. It has been found that samples with higher porosity (shown in the TEOS-23 sample) may accommodate more thermo mechanical stress as compared to samples with a lower porosity. In contrast: the ΔT and R_s values lead to the assumption that the sample with lower porosity has a better thermo shock performance. This contradictory behaviour might be explained with an inhomogeneous distribution of the phases which built up the material. Moreover the role of the amorphous phase (its chemical composition and the resulting properties and its share within the composite material) and its influence on the thermal properties is not clear.

5 Summary and outlook

The aim of this work was to develop an alumina-core/mullite-shell like composite material and to link its microstructure with its mechanical and thermal properties. Four different compositions were chosen based on two different silica precursors: as a model precursor tetraethyl orthosilicate (TEOS) was used. This type of silica source does not contain any alkali cations. The second silica precursor was colloidal silica (CS). This silica source is stabilized with sodium cations which have to be removed prior to processing; it is a precursor of high technical relevance.

The compositions were calculated to have a) a surplus of silica, which should result in a complete conversion of the alumina and b) a deficit of silica. This should result in the development of a core/shell like structure. The processing was carried out by known sol-gel syntheses for both systems, and different shapes of the ceramic parts were realized via a casting process.

The microstructure was characterised by means of solid state characterisation: XRD, SEM-EDX, porosity analysis and TEM investigations. Mechanical properties (flexural strength from room temperature to 1000 °C; hardness at room temperature) and thermophysical properties were analysed. Based on the thermophysical data the temperature difference ΔT and the thermo shock parameter R_s were computed. In order to verify these calculated parameters thermo shock experiments were carried out and crack development was monitored with micro computertomography.

The slurries of both systems showed a viscosity behaviour which allows a simple casting process: shear thinning was found resulting in a homogeneous distribution of the alumina particles within the system. The altering times necessary for the sol-to-gel transformation, however, was in the range of several weeks.

Reactive sintering was carried out in air in the temperature range from 1200 °C to 1600 °C, and the phase amount was estimated by XRD in combination with Rietveld analysis. It was found that the onset temperature of the mullite formation is in all samples in the same temperature range starting between 1300 °C and 1400 °C. However, this is assigned to the crystalline phase;

thermal analysis and investigations of the linear change indicated a difference in the onset of shrinkage: the onset of dimensional change in the CS-sample series was found at ~ 1100 °C, and that of the TEOS series was found at ~ 1200 °C. From these findings it was concluded that the CS precursor contributes to the control of the mullite formation, and it is assumed that the remaining sodium cations, even if their concentration is low, increase the mobility of the Al³⁺ and Si⁴⁺ species during reaction. However, the role of alkali is not clear yet.

Moreover it was found that the same amount of silica from TEOS and CS precursor (here: 23 mol.-%) resulted in a similar final composition of the as received ceramic. A surplus of the silica precursor content lead to a higher amount of mullite; in the case of CS an almost complete conversion was found while in the TEOS system the unreacted alumina content was significantly higher as compared to that of the CS system. This proves the hypothesis that the alkali ions contribute to the control of the mullite formation.

The porosity was found to be higher in the TEOS derived systems, which was assigned to the loss of four ethoxy groups during the sol-to-gel transformation process. The total porosities were measured to be 21 % in the CS-23 system and 34 % in the TEOS-23 system after thermal treatment at 1600 °C for 12 h.

In SEM investigations a part of the matrix was identified to be in an amorphous state and not completely reacted to mullite. With the help of TEM investigations the state of each phase of the composite was identified. Beside mullite and alumina as crystalline phases, a significant amount of an amorphous phase was found consisting of silica with some amount of alumina (~ 4 mole %). Moreover, results from the TEM investigations suggest that the mullite formation in the TEOS derived system is favoured due to a good wettability of the alumina particles and the intimate contact at the interface. However, the sol particles in the CS system showed a lower onset temperature of the mullite formation.

Both sample series showed sufficient flexural strength even at 1000 °C; the flexural strength values of the TEOS samples showed a higher decrease with an increase of the measuring temperature (~25 % of its value as measured at room temperature) as compared to the CS sample having a decrease of ~ 7 % at 500 °C to 1000 °C. The Weibull moduli for both sample series were in good accordance with data from literature.

The thermophysical data, thermal conductivity, thermal diffusivity, heat capacity and coefficient of thermal expansion were used to compute the critical temperature difference for expected failure (ΔT) and the thermal shock resistance to fracture initiation by thermal stresses (R_s). The results of these calculations suggest that the CS samples possess the better thermo shock performance. However, in thermo shock experiments it was found, that cracks appear in the CS samples while the TEOS derived samples remained crack-free even after 20 thermo shock cycles. It was concluded, that the phases within the microstructure might be inhomogeneous distributed which generates different levels of thermally induced stress, resulting in an inhomogeneous stress distribution.

In this work it has been shown, that an alumina-core/mullite-shell like microstructure can be formed using two different silica precursors and α -alumina powder. The reaction mechanisms seem to vary as a function of the precursor type, which was assigned to the remaining amount of alkali ions in the colloidal silica precursor. Both sample series show a pronounced porosity and both sample series are composed of mullite, alumina and a glassy phase. The composition and the amount of this glassy phase as a component of the microstructure is not well understood yet. This is of disadvantage, since it does not allow modelling and simulation of the mechanical and thermal properties.

Ongoing work should be focused on the analysis of the amorphous phase (total amount, composition and properties), on the phase homogeneity (grain size, phase distribution within the composite material) and on mechanical properties on a nanometer scale. A combination of small angle diffraction methods, local compositional analysis, local/global chemical bond analysis and nanoindentation should be able to provide a deeper understanding of the resulting material properties, which, in turn, can be used for the optimisation of the microstructure; one of the key factors might be the variation in filler size and the filler volume fraction of the system.

Works cited

- [1] H. Schneider and S. Komarneni, Mullite (ed.), Weinheim: Wiley-VCH, 2005, pp. 1-487.
- [2] N. L. Bowen and J. W. Greig, "The System Alumina-silica," J. Am. Ceram. Soc., vol. 7, no. 4, pp. 238-54, 1924.
- [3] H. Schneider, K. Okada and J. Pask, Mullite and Mullite Ceramics, John Wiley and Sons Ltd, 1994, pp. 1–251.
- [4] I. A. Aksay, D. M. Dabbs and M. Sarikaya, "Mullite for Structural, Electronic, and Optical Applications," J. Am. Ceram. Soc., vol. 74, no. 10, pp. 2343–58, 1991.
- [5] M. G. M. U. Ismail, Z. Nakai and S. Somiya, "Microstructure-mechanical Properties of Mullite Prepared by the Sol-Gel Method," J. Am. Ceram. Soc., vol. 70, no. 1, pp. C7-C8, 1987.
- [6] H. Schneider and A. Majdic, "Preliminary Investigations on the Kinetics of the High-temperature Transformation of Sillimanite to 3/2-mullite plus Silica and Comparison with the Behaviour of Andalusite and Kyanite," Sci. Ceram., vol. 11, pp. 191-96, 1981.
- [7] S. Cividanis, B. Campos, A. Rodrigues, D. Brunelli and P. Thim, "Review of Mullite Synthesis Routes by Sol-gel Method," J. Sol-Gel Sci. Tech., vol. 55, no. 1, pp. 111-25, 2010.
- [8] S. Somiya, R. F. Davis and J. A. Pask, Mullite and Mullite Matrix Composites, vol. 6, Ceram. Trans., 1990, pp. 1-649.
- [9] B. R. Marple and D. J. Green, "Incorporation of Mullite as a Second Phase into Alumina by an Infiltration Technique," J. Am. Ceram. Soc., vol. 71, pp. 471–73, 1988.
- [10] S. Taktak, R. Artır, S. Yılmaz and C. Bindal, "Fracture Toughness of Alumina-mullite Composites Produced by Infiltration Process," Key Eng. Mat., Vols. 264-268, pp. 981-84, 2004.
- [11] S. Taktak and S. M. Baspinar, "Wear and Friction Behaviour of Alumina-mullite Composite

by Sol-gel Infiltration Technique," *Materials and Design*, vol. 26, pp. 459-64, 2005.

- [12] B. Marple and D. Green, "Mullite Processing, Structure, and Properties. Mullite-alumina Particular Composites by Infiltration Processing: Mechanical Properties," *J. Am. Ceram. Soc.*, vol. 74, no. 10, pp. 2453-59, 1991.
- [13] S. Aramaki and R. Roy, "Revised Phase Diagram for the System Alumina-silica," *J. Am. Ceram. Soc.*, vol. 45, no. 5, pp. 229-42, 1962.
- [14] S. Freimann and S. Rahman, "Refinement of the Real Structures of 2:1 and 3:2 Mullite," *J. Eur. Ceram. Soc.*, vol. 21, pp. 2453-61, 2001.
- [15] P. Rehak, G. Kunath-Fandrei, P. Losso, B. Hildmann, H. Schneider and C. Jager, "Study of the Al Coordination in Mullites with Varying Al:Si ratio by ^{27}Al NMR Spectroscopy and X-ray Diffraction," *Am. Mineral.*, vol. 83, pp. 1266-1276, 1998.
- [16] X. R. Fischer, H. Schneider and D. Voll, "Formation of Aluminium Rich 9:1 Mullite and its Transformation to low Alumina Mullite upon Heating," *J. Eur. Ceram. Soc.*, vol. 16, pp. 109-13, 1996.
- [17] N. A. Toropov and Y. F. Galakhov, "Solid Solutions in the System Alumina-silica," *Aka. Nauk SSSR Otd. Khim. Nauk.*, vol. 8, 1958.
- [18] F. R. Davis and J. A. Pask, "Diffusion and Reaction Studies in the System Alumina-silica," *J. Am. Ceram. Soc.*, vol. 55, no. 10, pp. 525-31, 1972.
- [19] W. Bauer and I. Gordon, "Flame Fusion Synthesis of Several Types of Silicate Structures," *J. Am. Ceram. Soc.*, vol. 34, p. 250-54, 1951.
- [20] J. F. Schairer and N. L. Bowen, "The System Sodium Oxide Alumina-silica," *Am. J. Sci.*, vol. 254, pp. 129-95, 1956.
- [21] D. Hoffmann, R. Roy and S. Komarneni, "Diphasic Xerogels, A New Class of Materials: Phases in the Systems Alumina-silica," *J. Am. Ceram. Soc.*, vol. 67, pp. 467-68, 1984.
- [22] J. F. Klug, S. Prochazka and H. R. Doremus, "Alumina-silica Phase Diagram in the Mullite

Region," J. Am. Ceram. Soc., no. 70, pp. 750-59, 1987.

- [23] W. Guse and D. Mateika, "Growth of Mullite Single Crystals (Mullite) by the Czochralski Method," J. Cryst. Growth., vol. 22, pp. 237-40, 1974.
- [24] W. M. Kriven and J. A. Pask, "Solid Solution Range and Microstructure of Melt-grown Mullite," J. Am. Ceram. Soc., vol. 66, pp. 649-54, 1983.
- [25] R. F. Davis, "Decomposition of Mullite," J. Am. Ceram. Soc., vol. 55, no. 2, pp. 98-101, 1972.
- [26] J. A. Pask, The Alumina-silica System: Logical Analysis of Phenomenological Experimental Data. In: Tomsia, A. P. and Glaeser, A. (eds.) Ceramic Microstructure: Control at the Atomic Level, New York: Plenum Press, 1998, pp. 255-62.
- [27] H.-J. Kleebe, F. Siegelin, T. Straubinger and G. Ziegler, "Conversion of Alumina-silica Powder Mixtures to 3:2 Mullite Following the Stable or Metastable Phase Diagram," J. Am. Ceram. Soc., vol. 21, no. 14, pp. 2521-33, 2001.
- [28] A. K. Evans, "The Manufacture of Alumina and its Uses in Ceramics and Related Applications," Key. Eng. Mater., vol. 489, pp. 122-24, 1996.
- [29] W. H. Gitzen, "Alumina as a Ceramic Material," Am. Ceram. Soc., pp. 15, 1970.
- [30] S. P. Santos, S. H. Santos and P. S. Toledo, "Standard Transition Aluminas, Electron Microscopy Studies," Mat. Res., vol. 3, no. 4, pp. 104-14, 2000.
- [31] H. H. Pohland, Alcoa Chemie GmbH, Aluminium Oxide. Production, Properties, Applications, Verlag Modern Industries, 1999, pp. 1-70.
- [32] S. R. Zhou and L. R. Snyder, "Structures and Transformation Mechanisms of gamma, kappa and theta Transition Aluminas," Struct. Sci., vol. 47, pp. 617-30, 1991.
- [33] I. Levin and D. Brandon, "Metastable Alumina Polymorphs: Crystal Structures and Transition Sequences," J. Am. Ceram. Soc., vol. 81, no. 8, pp. 1995-2012, 1998.
- [34] H. Saalfeld, "The Structures of Gibbsite and of the Intermediate Products of its

Dehydration," *Neues Jahrb. Miner. Abhandl.*, pp. 1-87, 1960.

- [35] H. Saalfeld, "A Modification of Alumina with Sillimanite Structure," *Trans. Brit. Ceram. Soc.*, vol. 8, pp. 71-74, 1962.
- [36] J. Lewis, D. Schwarzenbach and H. D. Flack, "Electric Field Gradients and Charge Density in Corundum alpha-alumina," *Acta Crystallographica*, vol. 38, pp. 733-39, 1982.
- [37] R. Morell, *Handbook of Properties of Technical and Engineering Ceramics. Part II, Data Reviews, Section I, High-alumina Ceramics*, London, 1987, pp. 1-255.
- [38] P. Auerkari, "Mechanical and Physical Properties of Engineering Alumina Ceramics," Espoo, 1996.
- [39] B. C. Carter and G. M. Norton, *Ceramics Materials Science and Engineering*, Springer, 2007, pp. 1-716.
- [40] D. Munz and T. Fett, *Ceramics. Mechanical Properties, Failure Behaviour, Materials Selection*, Springer, 1999, pp. 1-298.
- [41] R. K. Iler, "The Chemistry of Silica," Wiley-Interscience, pp. 172-77, 1979.
- [42] S. Sakka and M. R. Almeida, *Handbook of Sol-Gel Science and Technology (eds): Processing, Characterization and Applications*-edited by Sumio Sakka, Netherland: Kluwer Academic Publishers, 2005, pp. 211-233.
- [43] N. Wiberg, F. A. Holleman and E. Wiberg, *Lehrbuch der Anorganischen Chemie*, Berlin, New York: Walter de Gruyter, 1995, pp. 911-930.
- [44] R. W. G. Wyckoff, "Crystal Structure of High Temperature (beta) Modification of Quartz," *America Journal of Science*, vol. 11, pp. 101-12, 1926.
- [45] E. W. Lee and M. W. Rainforth, *Ceramic Microstructures, Property Control by Processing*, Chapman & Hall, 1994, pp. 1-590.
- [46] P. L. Knauth, *Silica Physical Behavior, Geochemistry and Materials Applications*,

Petrogenesis of Chert in: Reviews in Mineralogy, vol. 29, Washington, D.C., 1994.

- [47] S. K. Ariffin, "What is Silica," EBS 425-Mineral Perindustrian, pp. 1-7, 2004.
- [48] H. Tada, A. Kumpel, R. Lathrop, J. Slanina, P. Nieva, P. Zavracky, I. Miaoulis and P. Wong, "Thermal Expansion Coefficient of Polycrystalline Silicon and Silicon Dioxide Thin Films at High Temperatures," Journal of Applied Physics, vol. 87, no. 9, pp. 1-5, 2000.
- [49] R. J. Angel and C. T. Prewitt, "Crystal Structure of Mullite. A Re-examination of the Average Structure," Am. Mineral., vol. 71, pp. 1476-82, 1986.
- [50] D. Mazza, S. Ronchetti and A. Costanzo, "Atomistic Simulations on Mullite $Al_4(Al_{2+2x}Si_{2-2x})O_{10-x}$ in a Variable Range of Composition," J. Eur. Ceram. Soc., vol. 28, pp. 367-70, 2008.
- [51] I. A. Aksay and J. A. Pask, "Stable and Metastable Equilibrium in the System Silica-alumina," J. Am. Ceram. Soc., vol. 58, no. 11-12, pp. 507-12, 1975.
- [52] C. Gerardin, S. Sundaresan, J. B. Benziger and A. Navrotsky, "Structural Investigation and Energetics of Mullite Formation from Sol-gel Precursors," Chem. Mater., vol. 6, pp. 160-70, 1994.
- [53] H. Schneider, J. Schreuer and B. Hildmann, "Structure and Properties of Mullite A Review," J. Am. Ceram. Soc., vol. 28, pp. 329-44, 2008.
- [54] L. H. Merwin, A. Sebald, H. Rager and H. Schneider, " ^{29}Si and ^{27}Al MAS NMR Spectroscopy of Mullite," Physics and Chemistry of Minerals, vol. 18, pp. 47-52, 1991.
- [55] C. Paulmann, "Study of Oxygen Vacancy Ordering in Mullite at high Temperatures," Phase Trans., vol. 59, pp. 77-90, 1996.
- [56] S. Somiya, T. Yoshimura, M. Suzuki and T. Yamaguchi, "Hydrothermal Processing of Mullite Powders from Alkoxides in "mullite" Somiya (ed.)," Uchida Rokakuho Publishing Co. Japan, pp. 63-87, 1985.
- [57] D. M. Sacks and J. A. Pask, "Sintering of Mullite Containing Materials. Effects of

Composition," J. Am. Ceram. Soc., vol. 65, pp. 65–70, 1982a.

- [58] D. M. Sacks, K. Wang, W. G. Scheiffele and N. Bozkurt, "Effect of Composition on Mullitization Behavior of alpha-alumina-silica Microcomposite Powders," J. Am. Ceram. Soc., vol. 80, no. 3, pp. 2663-72, 1997.
- [59] S. Johnson and J. Pask, "Role of Impurities on Formation of Mullite from Kaolinite and Alumina-silica Mixtures," Am. Ceram. Soc. Bull., vol. 61, pp. 838-42, 1982.
- [60] S. Sundaresan and A. I. Aksay, "Mullitization of Diphasic Aluminosilicate Gels," J. Am. Ceram. Soc., vol. 74, no. 10, p. 2388–92, 1991.
- [61] D. X. Li and W. J. Thomson, "Kinetics Mechanisms for Mullite Formation from Sol-gel Precursors," J. Mater. Res., vol. 5, no. 9, pp. 1963-69, 1990.
- [62] W. Krönert and H. Buhl, "The Influence of Various Gaseous Atmospheres on Refractories of the System Alumina-silica (Part II)," Interceram, vol. 2, pp. 140-46, 1978b.
- [63] S. T. Tso and J. A. Pask, "Reaction of Silicate Glasses and Mullite with Hydrogen Gas," J. Am. Ceram. Soc. , vol. 65, pp. 383-87, 1982.
- [64] V. N. Pitak and A. S. Antonov, "Effect of Oxidizing-reducing Medium on the Destruction of Mullite-corundum Refractories at High Temperatures," Antonov in Refractories, vol. 11, no. 11-12, pp. 763-67, 1970.
- [65] K. Hamano, K. Okada, Y. Nakajima and F. Okuda, "Preparation of Mullite Ceramics from Kaolin and Aluminium Hydroxide," Ceram. Soc. Jpn., vol. No. 2F05, 1988.
- [66] D. M. Sacks and J. Pask, "Sintering of Mullite Containing Materials," J. Am. Ceram. Soc., vol. 65, p. 70–77, 1982b.
- [67] Y. Nurishi and J. A. Pask, "Sintering of Alpha-alumina Amorphous Silica Compacts," Ceram. Int., vol. 8, no. 2, pp. 57–9, 1982.
- [68] B. Kanka and H. Schneider, "Sintering Mechanisms and Microstructural Developemnt of Co-precipitated Mullite," J. Mat. Sci., vol. 29, pp. 1239-49, 1994.

- [69] B. Müller and H. Schneider, "Reaction Sintering of Slip Casted Quartz plus alpha-alumina," Unpublished results, 1993b.
- [70] S. H. Hong and L. G. Messing, "Mullite Transformation Kinetics in Diphosphorus pentoxide-, Titanium dioxide-, and Diboron Trioxide-doped Aluminosilicate Gels," *J. Am. Ceram. Soc.*, vol. 80, pp. 1551–59, 1997.
- [71] B. Saruhan, W. Albers, H. Schneider and W. Kaysser, "Reaction and Sintering Mechanisms of Mullite in the Systems Cristobalite-alpha-Alumina and Amorphous Silica/ α -alumina," *J. Eur. Ceram. Soc.*, vol. 16, no. 10, pp. 1075–81, 1996.
- [72] A. Rana, O. Aiko and J. A. Pask, "Sintering of alpha-alumina-quartz and Alumina-cristobalite Related to the Mullite Formation," *Ceram. Int.*, vol. 8, no. 2, pp. 151–56, 1982.
- [73] M. Schmücker, W. Albers and H. Schneider, "Mullite Formation by Reaction Sintering of Quartz and alpha-Alumina a TEM Study," *J. Eur. Ceram. Soc.*, vol. 15, pp. 511–15, 1993.
- [74] W. Albers, "Reaction Sintering of Quartz, Cristobalite, and Silica Glass with alpha-alumina," PHD Thesis, University of Hannover, 1993.
- [75] J. Leivo, M. Linden, C. Teixeira, J. Puputti, J. Rosenholm, E. Levänen and T. A. Mäntylä, "Sol-gel Synthesis of a Nanoparticulate Aluminosilicate Precursor for Homogeneous Mullite Ceramics," *J. Mater. Res.*, vol. 21, p. 1279–85, 2006.
- [76] W. R. Jones, *Fundamental Principles of Sol-gel Technology*, London: Academic press, 1989, pp. 1-40.
- [77] M. C. Matos, L. Ilharco and R. Almeida, "The Evolution of TEOS to Silica Gel and Glass by Vibrational Spectroscopy," *J. of Non-Cry. Solids*, Vols. 147-48, pp. 232–37, 1992.
- [78] J. Pask, X. Zhang and A. Tomsia, "Effects of Sol-gel Mixing on Mullite Microstructure and Phase Equilibria in the α -alumina-silica," *J. Am. Ceram. Soc.*, vol. 70, pp. 704-07, 1987.
- [79] O. Burgos-Montes, I. M. Nieto and R. Moreno, "Mullite Compacts Obtained by Colloidal Filtration of Alumina Powders Dispersed in Colloidal Silica Suspensions," *Ceram. Int.*, vol. 33, pp. 327–32, 2007.

- [80] K. MacKenzie, R. Meinhold, J. Patterson, H. Schneider, M. Schmücker and D. Voll, "Structural Evolution in Gel-derived Mullite Precursors," *J. Eur. Ceram. Soc.*, vol. 16, pp. 1299–308, 1996a.
- [81] A. Boccaccini, R. Aldo and C. B. Ponton, "Colloidal Processing of Mullite Ceramics: Are Silica-alumina "Composite" Precursor Particles Essential?," *J. Mat. Sci. Lett.*, vol. 19, no. 19, pp. 1687–88, 2000.
- [82] S. Komarneni and R. Roy, "Application of Compositionally Diphasic Xero-gels for Enhanced Densification, the System Alumina-silica," *J. Am. Ceram. Soc.*, vol. 69, pp. C155-156, 1986.
- [83] K. Okada and N. Otsuka, "Characterization of the Spinel Phase from Silica-alumina Xerogels and the Formation Process of Mullite," *J. Am. Ceram. Soc.*, vol. 69, pp. 652-56, 1986.
- [84] M. Fukuoka, Y. Onoda, S. Inoue, K. Wada, A. Nukui and A. J. Makashima, "The Role of Precursor in the Structure of Silica-alumina Sols and Gels by the Sol-gel-process," *Sol-gel Sci. Tech.*, vol. 1, pp. 47-53, 1993.
- [85] J. E. Lee, J. W. Kim, Y. G. Jung, C. Y. Jo and U. Paik, "Effects of Precursor pH and Sintering Temperature on Synthesizing and Morphology of Sol-gel Processed Mullite," *Ceram. Int.*, vol. 28, pp. 935-40, 2002.
- [86] J. Anggono, *Mullite Ceramics: Its Properties, Structure, and Synthesis*, vol. 7, 2005, pp. 1-10.
- [87] J. C. Brinker and W. G. Scherer, *Sol-Gel Science. The Physics and Chemistry of Sol-Gel Processing*, San Diego: Academic Press INC, 1990.
- [88] C. Aoki, T. Ban, S. Hayashi and K. Okada, "Analysis of Mullitization Process by NMR-analysis for Sol-gel Solution. In: Abstracts of the Annual Meeting of the Ceramic Society of Japan," *Ceram. Soc. Jpn.*, vol. No. 2E16, 1992.
- [89] L. A. Paulick, Y. F. Yu and T. I. Mah, *Ceramic Powders from Metal Alkoxide Precursors*, vol. 21, G. L. Messing, K. S. Mazdiasni, J. W. McCauley and R. A. Habe, Eds.,

Westerville, OH: Advances in Ceramics, 1987, pp. 121-29.

- [90] A. K. Chakraborty, "Effect of pH on 980 °C Spinel Phase-Mullite Formation of Alumina-silica Gels," *J. Mater. Sci.*, vol. 29, pp. 1558-68, 1993.
- [91] I. Jaymes, A. Douy, D. Massiot and J. P. Coutures, "Characterization of Mono- and Diphasic Mullite Precursor Powders Prepared by Aqueous Routes, ^{27}Al and ^{29}Si MAS-NMR Spectroscopy Investigations," *J. Mater. Sci.*, vol. 31, pp. 4581-89, 1996.
- [92] D. Voll, A. Beran and H. Schneider, "Temperature-dependent Dehydration of Sol-gel-derived Mullite Precursors: A FTIR Spectroscopy Study," *J. Eur. Ceram. Soc.*, vol. 21, pp. 2479-85, 1998.
- [93] B. E. Yoldas, "Microstructure of Monolithic Materials Formed by Heat Treatment of Chemically Polymerized Precursors in the Alumina-silica Binary," *Ceram. Bull.*, vol. 59, no. 4, pp. 479-83, 1980.
- [94] H. Schneider, B. Saruhan, D. Voll, L. Merwin and A. Sebald, "Mullite Precursor Phases," *J. Eur. Ceram. Soc.*, vol. 11, pp. 87-94, 1993b.
- [95] B. Ghate, D. Hasselman and R. M. Spriggs, "Synthesis and Characterisation of High Purity, Fine Grained Mullite," *Am. Ceram. Soc. Bull.*, vol. 52, pp. 670-72, 1973.
- [96] K. Okada, N. Otsuka and S. Somiya, "Review of Mullite Synthesis Routes," *Am. Ceram. Soc. Bull.*, vol. 70, pp. 1633-40, 1991b.
- [97] D. J. Cassidy, J. L. Woolfrey, J. R. Bartlett and B. Ben-Nissan, "The Effect of Precursor Chemistry on Crystallization and Densification of Sol-gel Derived Mullite Gels and Powders," *J. Sol-Gel Sci. Tech.*, vol. 10, pp. 19-30, 1997.
- [98] T. Ban, S. Hayashi, A. Yasumori and K. Okada, "Characterization of Low Temperature Mullitization," *J. Eur. Ceram. Soc.*, vol. 16, pp. 127-32, 1996.
- [99] I. Jaymes and A. Douy, "New Aqueous Mullite Precursor Synthesis, Structural Study by ^{27}Al and ^{29}Si NMR Spectroscopy," *J. Eur. Ceram. Soc.*, vol. 16, pp. 155-60, 1996.

- [100] P. Padmaja, G. Anilkumar, P. Mukundan, G. Aruldas and K. Warriar, "Characterisation of Stoichiometric Sol-gel Mullite by Fourier Transform Infrared Spectroscopy," *J. Inorg. Mater.*, vol. 3, pp. 693–98, 2001.
- [101] X. H. Jin, L. Gao and J. K. Guo, "The Structural Change of Diphasic Mullite Gel Studied by XRD and IR Spectrum Analysis," *J. Eur. Ceram. Soc.*, vol. 22, pp. 1307–11, 2002.
- [102] H. Shiga, M. Ismail and K. Katayama, "Sintering of Zirconium Dioxide Toughened Mullite Ceramics and its Microstructure," *J. Ceram. Soc. Jpn.*, vol. 99, pp. 798-02, 1991.
- [103] R. H. Ewell and H. Insley, "Thermal Behavior of the Kaolin Minerals," *J. Res. Nat. Bur.*, vol. 14, pp. 615-27, 1935.
- [104] J. Ossaka, "Tetragonal Mullite-like Phase from Coprecipitated Gels," *Nature*, vol. 19, pp. 1000-1001, 1961.
- [105] S. A. Baspinar and F. Kara, "Optimization of the Corrosion Behaviour of Mullite Refractories Against Alkali Vapor Via Zirconia Sulphate Addition to the Binder Phase," *Ceramics Silikáty*, vol. 54, no. 4, pp. 242-49, 2009.
- [106] K. S. Mazdiasni and L. M. Brown, "The Synthesis and Mechanical Properties of Stoichiometric Aluminium Silicate," *J. Am. Ceram. Soc.*, vol. 55, no. 11, pp. 548-52, 1972.
- [107] M. Ismail, Z. Nakai, K. Minegishi and S. Somiya, "Synthesis of Mullite Powder and its Characteristics," *J. High Technol. Ceram.*, vol. 3, pp. 123–34, 1986.
- [108] F. Mizukami, K. Maeda and M. Toba, "Effect of Organic Ligands on the Formation of Mullite," *Ceram. Soc. Jpn.*, Vols. No. 6-1A01, 1990.
- [109] M. O. S. Nogami and K. Nagasaka, "Preparation of Cordierite Glass by the Sol-gel Process," *J. Mat. Sci.*, pp. 4339-42, 1989.
- [110] K. Nishu, T. Yokoyama, T. Watanabe and T. Taritani, "Characterization of Amorphous Aluminosilicate formed by Adsorption of Silicic acid on Aluminium Hydroxide," *Ceram. Soc. Jpn.*, vol. Paper No. 1B08, 1989.

- [111] D. M. Sacks, N. Bozkurt and W. G. Scheiffele, "Fabrication of Mullite and Mullite-matrix Composites by Transient Viscous Sintering of Composite Powders," *J. Am. Ceram. Soc.*, vol. 74, pp. 2428–37, 1991.
- [112] J. Wang, C. B. Ponton and P. Marquis, "Effects of Green Density on Crystallization and Mullitization in the Transiently Sintered Mullite," *J. Am. Ceram. Soc.*, vol. 75, pp. 3457–61, 1992.
- [113] M. Bartsch, B. Saruhan, M. Schmücker and H. Schneider, "Novel Low Temperature Processing Route of Dense Mullite Ceramic by Reaction Sintering of Amorphous Silica Coated gamma-alumina Particle Nanocomposites," *Am. Ceram. Soc.*, vol. 82, pp. 1388-92, 1999.
- [114] M. Iwata, K. Oshima, T. Isoda, M. Arai, K. Nakano and A. Kamiya, "Mechanical Properties and Micro-structures of Fiber Reinforced Silicon Nitride and Mullite Composites. In: Abstracts of the Annual Meeting of the Ceramic Society of Japan," *Ceram. Soc. Jpn. Paper No. 2E36*, 1989.
- [115] L. Pach, S. Komarneni and C. Liu, "Nano-composite Route to the Stabilization of Porous θ -Alumina," *J. of Porous Materials*, vol. 2, pp. 131–34, 1995.
- [116] B. L. Metcalfe and J. Sant, "The Synthesis, Microstructure, and Physical Properties of High Purity Mullites," *Trans. Brit. Ceram. Soc.*, vol. 74, pp. 193–201, 1975.
- [117] E. Tkalcec, H. Ivankovic, R. Nass and H. Schmidt, "Crystallization Kinetics of Mullite Formation in Diphasic Gels Containing Different Alumina Components," *J. Eur. Ceram. Soc.*, vol. 23, pp. 1465-75, 2003.
- [118] W. Wei and W. J. Halloran, "Phase Transformation of Diphasic Aluminosilicate Gels," *J. Am. Ceram. Soc.*, vol. 71, no. 3, pp. 166–72, 1988.
- [119] A. Boccaccini, K. T. Khalil and M. Bucker, "Activation Energy for the Mullitization of Diphasic Gel Obtained from Fumed Silica and Boehmite Sol," *Mat. Lett.*, vol. 38, pp. 116–20, 1999.
- [120] P. Boch, T. Chartier and P. D. D. Rodrigo, "High-Purity Mullite Ceramics by Reaction-

Sintering," *Ceram. Trans.*, vol. 6, pp. 353–74, 1990.

- [121] R. Baranwal, M. P. Villar, R. Garcia and R. M. Laine, "Flame Spray Pyrolysis of Precursors as a Route to Nano-mullite Powder: Powder Characterization and Sintering Behavior," *J. Am. Ceram. Soc.*, vol. 84, pp. 951-61, 2001.
- [122] S. Hori and R. Kurita, "Characterization and Sintering of Alumina Powders Formed by Chemical Vapor Deposition," *Ceram. Trans.*, vol. 6, pp. 311-22, 1990.
- [123] K. Itatani, T. Kubozono, S. F. Howell, A. Kishioka and M. Kinoshita, "Some Properties of Mullite Powders Prepared by Chemical Vapor Deposition," *J. Mat. Sci.*, vol. 30, pp. 1158-65, 1995.
- [124] O. R. Monteiro, Z. Wang and I. G. Brown, "Deposition of Mullite and Mullite-like Coatings on Silicon Carbide by Dual Source Metal Plasma Immersion," *J. Mat. Res.*, vol. 12, pp. 2401-10, 1997.
- [125] C. Kaya, Y. J. He, X. Gu and G. E. Butler, "Nanostructured Ceramic Powders by Hydrothermal Synthesis and their Applications," *Microporous and Mesoporous Materials*, vol. 54, pp. 37-49, 2002.
- [126] M. Suzuki, S. Hiraishi, M. Yoshimura and S. Somiya, "Preparation of Mullite Powder by Calcination of the Products Hydrothermally Treated from Mixed Alkoxide or Mixed Sol," *Yogyo- Kyokaishi*, vol. 92, pp. 320-27, 1984.
- [127] F. Zhang, T. Kato, M. Kato, M. Fuji and M. Takakashi, "Gel-casting Fabrication of Porous Ceramic using a Continuous Process," *J. Eur. Ceram. Soc.*, vol. 26, pp. 667-71, 2006.
- [128] D. B. Kong, S. Ying, H. Yang, H. Li, S. Wei and J. Wang, "Preparation of Dense Mullite Ceramics through Gel-Castings of Alumina Slurry Dispersed in Silica Sol," *Adv. Eng. Mat.*, vol. 7, no. 8, pp. 746-50, 2005.
- [129] T. Sato, M. Ishizuka and M. Shimada, "Sintering and Characterization of Mullite-Alumina Composites," *Ceram. Int.*, vol. 12, no. 2, pp. 61-65, 1986.
- [130] P. Boch and J. Niepce, *Ceramic Materials. Processes, Properties and Applications (Eds)*,

ISTE Ltd, 2007, pp. 1-573.

- [131] L. Pach and P. Mankos, "Diphasic Mullite Gel Pressed at 1.5 GPa: Mechanical Properties and Microstructure of Ceramics," *J. Mater. Sci.*, vol. 32, pp. 3195-99, 1997.
- [132] Y. M. Sung, "Kinetics Analysis of Mullite Formation Reaction at High Temperatures," *Acta Mater.*, vol. 48, pp. 2157-62, 2000.
- [133] F. Orgaz, "Densification and Crystalization Kinetics of Mullite Diphasic Gels from Non-isothermal Dilatometry Experiments," *Bol. Soc. Esp. Ceram.*, vol. 43, no. 6, pp. 358-65, 2008.
- [134] R. Barea, I. Osendi, F. Ferreira and P. Miranzo, "Thermal Conductivity of Highly Porous Mullite Material," *Acta Materialia*, vol. 53, pp. 3313-18, 2005.
- [135] H. Ivankovic, E. Tkalcevic, R. Rein and H. Schmidt, "Microstructure and High Temperature 4-point Bending Creep of Sol-gel Derived Mullite Ceramics," *J. Europ. Ceram. Soc.*, vol. 26, pp. 1637-46, 2006.
- [136] S. Kanzaki, H. Tabata, T. Kumazawa and S. Ohta, "Sintering and Mechanical Properties of Stoichiometric Mullite," *J. Am. Ceram. Soc.*, vol. 68, pp. C6-C7, 1985.
- [137] H. Ohira, M. G. M. U. Ismail, Y. Yamamoto, T. Akiba and S. Somiya, "Mechanical Properties of High Purity Mullite at Elevated Temperatures," *J. Eur. Ceram. Soc.*, vol. 16, no. 2, pp. 225-29, 1996.
- [138] H. Ohnishi, T. T. Kawanami, A. Nakahira and K. Niihara, "Microstructure and Mechanical Properties of Mullite Ceramics," *Yogyo Kyokaiishi*, vol. 98, no. 6, pp. 541-47, 1990.
- [139] W. R. Rice, *Porosity of Ceramics*, Virginia: Marcel Dekker, Inc., 1998, pp. 1-539.
- [140] W. Yan, N. Li and B. Han, "Effects of Sintering Temperature on Pore Characterization and Strength of Porous Corundum-mullite Ceramics," *J. Ceram. Proc. Res.*, vol. 11, no. 3, pp. 388-91, 2010.
- [141] H. She and T. Ohji, "Porous Mullite Ceramics with High Strength," *J. Mat. Sci. Lett.*, vol.

21, pp. 1833-34, 2002.

- [142] R. Sivakumar, D. D. Jayaseelan, T. Nishikawa, S. Honda and H. Awaji, "Influence of MgO on Microstructure and Properties of Mullite-Mo Composites Fabricated by Pulse Electric Current Sintering," *Ceram. Int.*, vol. 27, no. 5, pp. 537-41, 2001.
- [143] C. Aksel, "The Role of Fine Alumina and Mullite Particles on the Thermo-mechanical Behavior of Alumina-mullite Refractory Ceramics," vol. 57, pp. 708-14, 2002.
- [144] W. Kollenberg and H. Schneider, "Microhardness of Mullite at Temperatures up to 1000 degree," *J. Am. Ceram. Soc.*, vol. 72, pp. 1739-40, 1989.
- [145] T. Kumazawa, S. Kanzaki, S. Ohta and H. Tabata, "Influence of Mechanical Properties of Silica-alumina Ceramics," *J. Ceram. Soc. Jpn.*, vol. 96, pp. 85-91, 1988.
- [146] B. Hildmann and H. Schneider, "Thermal Conductivity of 2:1-Mullite Single Crystals," *J. Am. Ceram. Soc.*, vol. 88, no. 10, pp. 2879-82, 2005.
- [147] P. Miranzo, M. I. Osendi and E. Garcia, "Porous Mullite Templated from Hard Mullite Beads," *J. Eur. Ceram. Soc.*, vol. 31, pp. 1397-1403, 2011.
- [148] H. Schneider and E. Eberhard, "Thermal Conductivity of 2/1-mullite Single Crystals," *J. Am. Ceram. Soc.*, vol. 88, pp. 2879-82, 2005.
- [149] J. Schreuer, B. Hildmann and H. Schneider, "Elastic Properties of Mullite Single Crystals up 1400 °C," *J. Am. Ceram. Soc.*, vol. 89, no. 5, pp. 1624–31, 2006.
- [150] G. Brunauer, H. Boysen, F. Frey, H. Schneider and T. h. Hansen, "High Temperature Crystal Structure of a 3:2 Mullite from Neutron Diffraction Data," *Z. Krist.*, vol. 216, pp. 284-90, 2001.
- [151] P. A. Lessing, R. S. Gordon and K. S. Mazniasni, "Creep of Polycrystalline Mullite," *J. Am. Ceram. Soc.*, vol. 58, no. 3-4, pp. 149-153, 1975.
- [152] H. Schneider and S. Komarneni, "Thermal Properties of Mullite (Eds)," Weinheim, 2005, pp. 149-64.

- [153] M. Hamidouche, N. Bouaouadja, C. Olagnon and G. Fantozzi, "Thermal Shock Behaviour of Mullite Ceramics," *Ceram. Int.*, vol. 29, pp. 599-609, 2003.
- [154] W. E. Lee and W. M. Rainforth, *Structural Oxides: Alumina and Mullite in Ceramic Microstructures: Property Control by Processing*, Chapman and Hall, 1994, pp. 290-316.
- [155] A. Startsev, V. Voronov, I. Kaplun, A. Panevkin and A. Vasin, "Open-Hearth Furnace Steel Melting Bath Refractory Servicing," *Refractories and Industrial Ceramics*, vol. 51, no. 3, pp. 142-45, 2010.
- [156] A. V. Kononov, "The Crisis in Refractories, its Causes, its Lessons," *Novye Ogneupory*, vol. 1, pp. 44-51, 2010.
- [157] L. A. Lay, *Corrosion Resistance of Technical Ceramics*, Middlesex, UK: National Physical Laboratory, 1984, pp. 1-158.
- [158] *Hand Book of Ceramic Engineering* . Ceramic Society of Japan, 2nd edn, Tokyo: Gihodo, 1990a, pp. 1690-15.
- [159] M. L. Auger, "Development of CVD Mullite Coatings for Si-based Ceramics, PHD Dissertation, Boston University," 1999.
- [160] K. N. Lee, R. A. Miller and N. S. Jacobson, "New Generation of Plasma-sprayed Mullite Coatings on Silicon Carbide," *J. Am. Ceram. Soc.*, vol. 78, no. 3, pp. 705-10, 1995.
- [161] A. Schrijnemakers, S. Andre, G. Lumay, N. Vandewalle, F. Boschini, R. Cloots and B. Vertruzen, "Mullite Coatings on Ceramics Substrates Stabilization of Alumina-silica Suspensions for Spray Drying of Composite Granules Suitable for Reactive Plasma Spraying," *J. Eur. Ceram. Soc.*, vol. 29, pp. 2169–75, 2009.
- [162] *Hand Book of Ceramic Engineering*, Ceramic Society of Japan, 2nd edn, Tokyo: Gihodo, 1990c, pp. 2081-84.
- [163] H. Horitsu, "Ceramics Bioreactor," *Kinozairyuu*, vol. 11, pp. 14-28, 1991.
- [164] Matsushita Electric Co, Kadoma, Japan: Catalogue, 1991.

- [165] M. T. Dario and A. Bachiorrini, "Interaction of Mullite with Some Polluting Oxides in Diesel Vehicles Filters," *Ceram. Int.*, vol. 25, pp. 511–16, 1999.
- [166] *Hand Book of the Ceramic Engineering*, Ceramic Society of Japan, 2nd edn, Tokyo: Gihodo Publishing, 2002, pp. 1249-50.
- [167] M. Horiuchi, K. Mizushima and Y. Takeuchi, "New Mullite Ceramic Packages and Substrates," *Trans. Comp. Hybrids Manuf. Technol.*, vol. 11, pp. 439-46, 1988.
- [168] F. Shackelford, R. Doremus, J. D. Duval and S. H. Risbud, *Ceramic and Glass Materials: Structure, Properties and Processing* (eds), Springer, 2008, pp. 20-50.
- [169] J. I. Andrews, G. H. Beall and A. Lempicki, "Luminescence of Cr ion in Mullite Transparent Glass-Ceramics," *J. Lumin.*, vol. 36, pp. 65-74, 1986.
- [170] S. Prochazka and J. F. Klug, "Infrared-Transparent Mullite Ceramic," *J. Am. Ceram. Soc.*, vol. 66, pp. 874-80, 1983.
- [171] T. Hanazawa, "Cermets for Friction Materials," *Tetsu Hagane*, vol. 73, pp. 786-95, 1987.
- [172] H. Takada, A. Nakahira, H. Ohnishi, s. Ueda and K. Niihara, "Improvement of Mechanical Properties of Natural Mullite-SiC Nanocomposite," *J. Powder Mat.*, vol. 38, pp. 348-51, 1991.
- [173] J. F. D. M. Bartholome and J. S. Moya, "Influence of Metal Particle Size on Crack Growth Resistance in Mullite-molybdenum Composites," *J. Am. Ceram. Soc.*, vol. 85, pp. 2278–8, 2002.
- [174] W. G. Fahrenholtz, K. G. Ewsuk, R. E. Loehman and P. Lu, "Kinetics of Metal Composite Formation by Reactive Metal Penetration," *J. Am. Ceram. Soc.*, vol. 81, pp. 2533-41, 1998.
- [175] C. Aneziris, S. Dudczig, N. Gerlach, H. Berek and D. Veres, "Thermal Shock Performance of Fine Grained Alumina Ceramics with Titanium Dioxide and Zirconium Dioxide Additions for Refractory Applications," *Adv. Eng. Mater.*, vol. 12, no. 6, pp. 478–85, 2010.
- [176] A. Khan, M. H. Chan, P. M. Harmer and F. R. Cook, "Toughness-Curve Behavior of an

Alumina–mullite Composite," *J. Am. Ceram. Soc.*, vol. 81, no. 10, pp. 2613-23, 1998.

- [177] G. Nicoletto, L. Esposito and A. Tucci, "Wear and Microstructure of Polycrystalline Aluminas," *Ceram. Acta*, vol. 9, pp. 13-19, 1997.
- [178] N. Schmitt, A. Burr, A. Berthaud and J. Poirier, "Micromechanics Applied to the Thermal Shock Behavior of Refractory Ceramics," *Mechanics of Materials*, vol. 34, pp. 725-47, 2002.
- [179] S. Li and N. Li, "Influences of Composition of Starting Powders and Sintering Temperature on the Pore Size Distribution of Porous Corundum-mullite ceramics," *Sci. of Sintering*, vol. 37, pp. 173-80, 2005.
- [180] E. Medvedovski, "Alumina-mullite Ceramics for Structural Applications," *Ceram. Int.*, vol. 32, pp. 369-75, 2006.
- [181] C. Aksel, "The Effect of Mullite on the Mechanical Properties and Thermal Shock Behaviour of Alumina-mullite Refractory Materials," *Ceram. Int.*, vol. 29, pp. 183-88, 2003.
- [182] A. Mendonca, J. Ferreira and I. Salvado, "Mullite-alumina Composites Prepared by Sol-gel," *J. Sol-Gel Sci. Tech.*, vol. 13, pp. 201-05, 1998.
- [183] J. T. Baker, J. Zimba, T. E. Akpan, I. L. Bashir, T. C. Watola and O. W. Soboyejo, "Viscoelastic Toughening of Aluminosilicate Refractory Ceramics," *Acta Mat.*, vol. 54, pp. 2665-75, 2006.
- [184] D. P. H. Hasselman, "Unified Theory of Thermal Shock," *J. Am. Ceram. Soc.*, vol. 52, pp. 600-604, 1969.
- [185] W. D. Kingery, H. K. Bowen and D. R. Uhlmann, *Introduction to Ceramics (2nd edn)*, New York: Wiley, 1976, pp. 1-1056.
- [186] Y. Tang, Y. Lü, A. Li, Y. Li, S. Shi and Z. Ling, "Fabrication of Fine Mullite Powders by Alpha-aluminium trihydroxide-silica Core–shell Structure Precursors," *Applied Surface Sci.*, vol. 202, pp. 211–17, 2002.

- [187] S. Wang, Y. Hsu, T. Yang, C. Chang, Y. Chen, C. Huang and F. Yen, "Silica Coating on Ultrafine Alpha-alumina Particles," *Mat. Sci. Eng.*, vol. 395, pp. 148-52, 2005.
- [188] P. Pena, J. Bartolome, J. Requena and S. J. Moya, "Mullite-alumina Funtional Gradient Ceramics," *J. de Phy. III*, vol. 3, pp. 1261-66, 1993.
- [189] J. I. Root, D. J. Sullivan and R. B. Marple, "Residual Stress in Alumina-mullite Composites," *J. Am. Ceram. Soc.*, vol. 74, no. 31, pp. 579-83, 1991.
- [190] DIN 38406-14, Bestimmung von Natrium mittels Atomabsorptionsspektrometrie (AAS) in der Luft-Acetylen-Flame, 1992.
- [191] J. H. Medlin, N. H. Nsuhr and B. J. Bodkin, "Atomic Absorption Analysis of Silicates Employing Lithium Borate Fusion," *At. Absorpt. Newsletter*, vol. 8, pp. 25-29, 1969.
- [192] F. R. Egerton, *Physical Principles of Electron Microscopy: An Introduction to TEM, SEM and AEM*, New York and NY: Springer, 2008, pp. 1-202.
- [193] W. E. Lorensen and H. Cline, "Marching Cubes: A High Resolution 3D Surface Construction Algorithm," *Computer graphics*, vol. 21, no. 4, pp. 163-69, 1987.
- [194] M. Bengisu, *Engineering Ceramics*, Berlin Heidelberg: Springer, 2001, pp. 30-55.
- [195] S. J. Reed, *Principles of Ceramics Processing*, vol. 2nd, New York: John Wiley & Sons, INC, 1995, pp. 40-80.
- [196] EN 1389, Hochleistungskeramik-Keramische Verbundwerkstoffe-Physikalische eigenschaften-bestimmung der Dichte und scheinbaren Porosität, Deutsche Fassung, 2004.
- [197] I. Langmuir, "The Adsorption of Gases on Plane Surface of Glass, Mica and Platinum," *J. Am. Ceram. Soc.*, vol. 40, no. 9, pp. 1361-403, 1918.
- [198] DIN 66133, Bestimmung der Porenvolumenverteilung und der Spezifischen Oberffläche von Feststoffen durch Quecksilberintrusion, 1993.
- [199] DIN ISO 9277, Bestimmung der spezifischen Oberfläche von Feststoffen durch

Gasadsorption nach dem BET-Verfahren, 2003-05.

[200] DIN EN 820-3, Bestimmung der Thermoschockbeständigkeit mit dem Wasserabschreckversuch. 2004.

[201] DIN EN 820-3:2004-11, Advanced Technical Ceramics-Methods of Testing Monolithic Ceramics-Thermomechanical Properties. Determination of Resistance to Thermal Shock by Water Quenching, 2004.

[202] "Thermal Reactive Aluminas for Ceramics, Almatis Premium Alumina. Global Product Data," [Online]. Available: www.almatis.com. [Accessed 9 10 2009].

Appendices

Appendix 1: Thermal expansion coefficients of mullite

Composition *)	Method	Temperature [°C]	α [$\cdot 10^{-6} \text{ K}^{-1}$]				ref.
			$\alpha_{(a)}$ axis	$\alpha_{(b)}$ axis	$\alpha_{(c)}$ axis	α_A axis	
0.25	XRD	300-1000	4.1	6.0	5.7	5.3	[53]
0.25	ND	1000-1600	6.8	9.3	6.3	7.5	[150]
0.39	DIL	300-1000	4.5	6.1	7.0	5.9	[149]
0.39	DIL	100-1400	6.2	7.3	6.9	6.8	[149]
0.24	XRD	300-900	3.9	7.0	5.8	5.6	[148]

*) The mullite composition is given by $\text{Al}_{4+2x}\text{Si}_{2-2x}\text{O}_{10-x}$, where x is the number of oxygen vacancies per unit cell, XRD: high-temperature x-ray diffraction, ND: high temperature neutron diffraction, DIL: high temperature single crystal dilatometry, α : linear thermal expansion coefficient, average of thermal expansion in the different axis is given by α_A : $(\alpha_{(a)} + \alpha_{(b)} + \alpha_{(c)})/3$

Appendix 2: Corrosion resistance of mullite in comparison to alumina

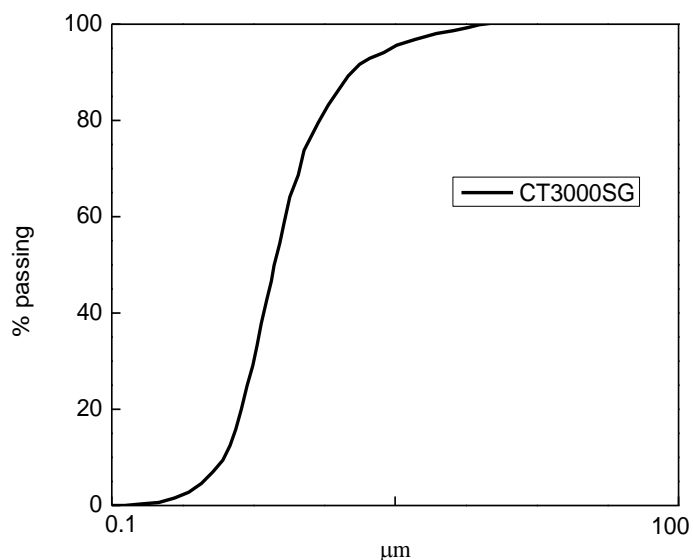
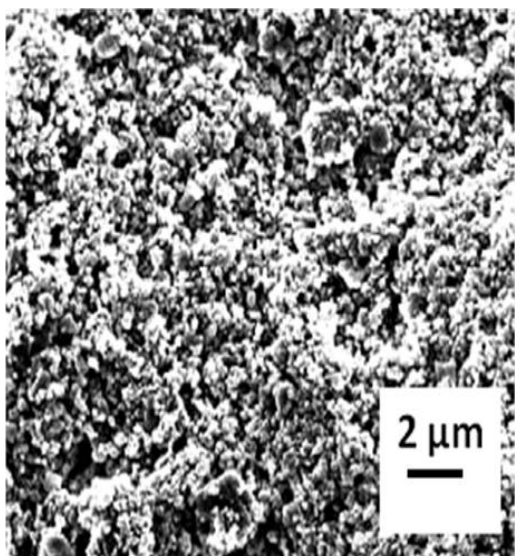
Reactant		Mullite	Al ₂ O ₃
acid	HCL	good	good
	HNO ₃	good	good
	H ₂ SO ₄	good	good
alkali	NaOH	-	fair
	KOH	fair	good
molten salt	NaOH	bad (500)	good (500)
	KOH	bad (500)	fair (500)
	K ₂ CO ₃	good (1000)	good (1000)
	Na ₂ CO ₃	-	good (1000)
slag	acidic	good	good
	neutral	good	good
	basic	fair	fair
molten metal	Al	good	fair
	Fe	bad	fair
gas	vacuum	good (1500)	good (1700)
	O ₂	good (1500)	good (1900)
	Ar	good	good (1700)
	H ₂ O	good	good (1700)
	NH ₃	good	-
	HCl	good	good
	CO	good	good(1700)
	CO ₂	good	good(1200)
	SO ₂	good	good

Temperatures in °C are represented in parentheses; adapted from [1]

Appendix 3: Typical product properties of CT3000SG [202]

Properties	Values
specific surface area [$\text{m}^2 \text{g}^{-1}$]	7.5
particle size, d_{50} Cilas [μm]	0.5
density [g cm^{-3}]	3.90
percentage of Al_2O_3	99.8

Appendix 4: Microstructure of alumina (left) and particle size distribution (right) as provided by the supplier [31]



Appendix 5: Composition of the as-prepared TEOS-23 sample

Parameters	Sol-gel system				
	TEOS	$\text{C}_2\text{H}_5\text{OH}$	H_2O	SiO_2	Al_2O_3
molecular weight [g mol^{-1}]	208.33	46.07	18.01	60.08	101.96
volume [ml]	20	7	3	-	-
mass [g]	18.68	5.67	3.00	5.39	30.62
number of moles	0.0896	0.1230	0.1665	0.0897	0.3003
mole ratio				1	3.4
mol.-%				23	77

Appendix 6: Composition of the as-prepared TEOS-77 sample

Parameters	Sol-gel system				
	TEOS	C ₂ H ₅ OH	H ₂ O	SiO ₂	Al ₂ O ₃
molecular weight [g mol ⁻¹]	208.33	46.07	18.01	60.08	101.96
volume [ml]	67	23	10	-	-
mass [g]	62.58	18.63	10.00	18.05	9.15
number of moles	0.3004	0.4043	0.5500	0.3004	0.0890
mole ratio				3.4	1
mol.-%				77	23

Appendix 7: Characteristics of colloidal silica (CS) as provided by the supplier (Chemiewerk Bad Köstritz GmbH, Bad Köstritz, Germany)

Parameter	Characteristic	Parameter	Characteristic
particle size	~35 nm	pH value	9.6
specific surface area	80 m ² g ⁻¹	density	1.39 g cm ⁻³
Wt.-% Na ₂ O	0.25	viscosity at 25 °C	20 mPa·s

Appendix 8: Characteristics of Lewatit MonoPlus S 108 resin as provided by the supplier (Kurt Obermeier GmbH & Co.KG, Bad Berleburg, Germany)

Property	Characteristic
ionic form as supplied	Na ⁺
functional group	sulfonic acid
matrix	cross linked polystyrene
structure	gel type beads
mean bead size	0.62 mm ± 0.05 mm
stability (pH range)	0-14

Appendix 9: Composition of the as-prepared CS-23 sample

Parameters	Sol-gel system				
	CS	C ₂ H ₅ OH	H ₂ O	SiO ₂	Al ₂ O ₃
molecular weight [g mol ⁻¹]	78.09	46.07	18.01	60.08	101.96
volume [ml]	18.5	9.9	4.9	-	-
mass [g]	25.62	8.02	4.95	19.72	113.58
number of moles	0.328	0.174	0.275	0.328	1.114
mole ratio				1	3.4
mol.-%				23	77

Appendix 10: Composition of the as-prepared CS-40 sample

Parameters	Sol-gel system				
	CS	C ₂ H ₅ OH	H ₂ O	SiO ₂	Al ₂ O ₃
molecular weight [g mol ⁻¹]	78.09	46.07	18.01	60.08	101.96
volume (ml)	33.32	17.88	8.94	-	-
mass (g)	46.14	14.48	8.94	35.50	90.30
number of moles	0.591	0.314	0.496	0.591	0.886
mole ratio				2	3
mol.-%				40	60

Appendix 11: Phase composition of samples sintered in the temperature range from 1100 °C to 1600 °C with a temperature slope of 5 K min⁻¹ with holding times of 12 h

Temp. [°C]	System	Cristobalite [mol.-%]	Corundum [mol.-%]	Mullite [mol.-%]
1100	TEOS-23	0	100	0
	TEOS-77	0.5	99	0
	CS-23	1	99	0
	CS-40	4	96	0
1200	TEOS-23	10	90	0
	TEOS-77	23	77	0
	CS-23	8	92	0
	CS-40	27	73	0
1300	TEOS-23	14	86	0
	TEOS-77	41	59	0
	CS-23	6	94	0
	CS-40	29	71	0
1400	TEOS-23	10	86	4
	TEOS-77	44	56	0.1
	CS-23	2	75	23
	CS-40	26	67	7
1500	TEOS-23	2	63	35
	TEOS-77	39	41	20
	CS-23	0	65	35
	CS-40	0	12	88
1600	TEOS-23	0	56	44
	TEOS-77	24	2	74
	CS-23	0	60	40
	CS-40	0	2	98

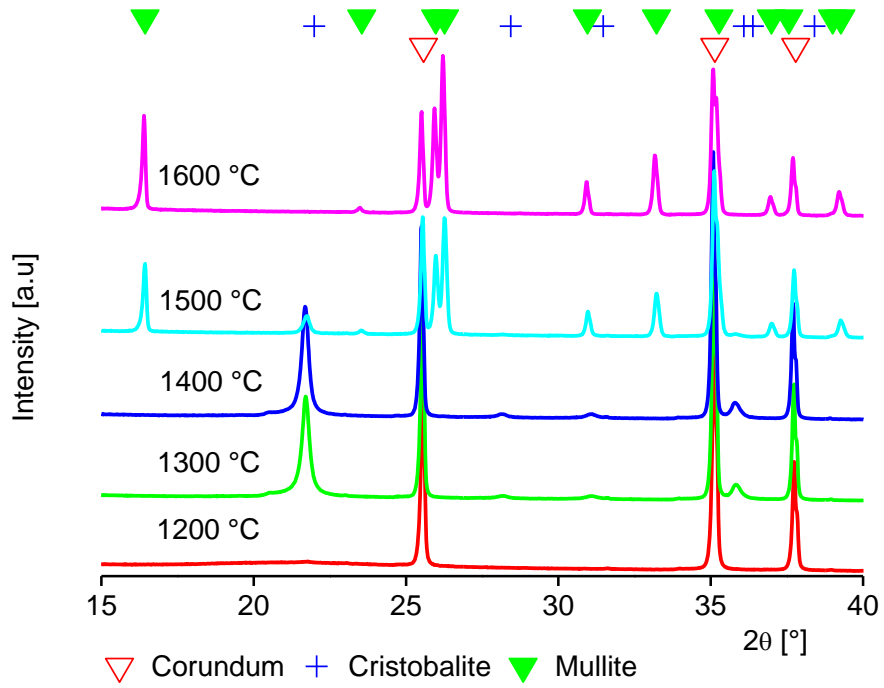


Figure 5.1: XRD patterns of the TEOS-23 samples sintered at different temperatures with holding times of 12 h

Appendix 13

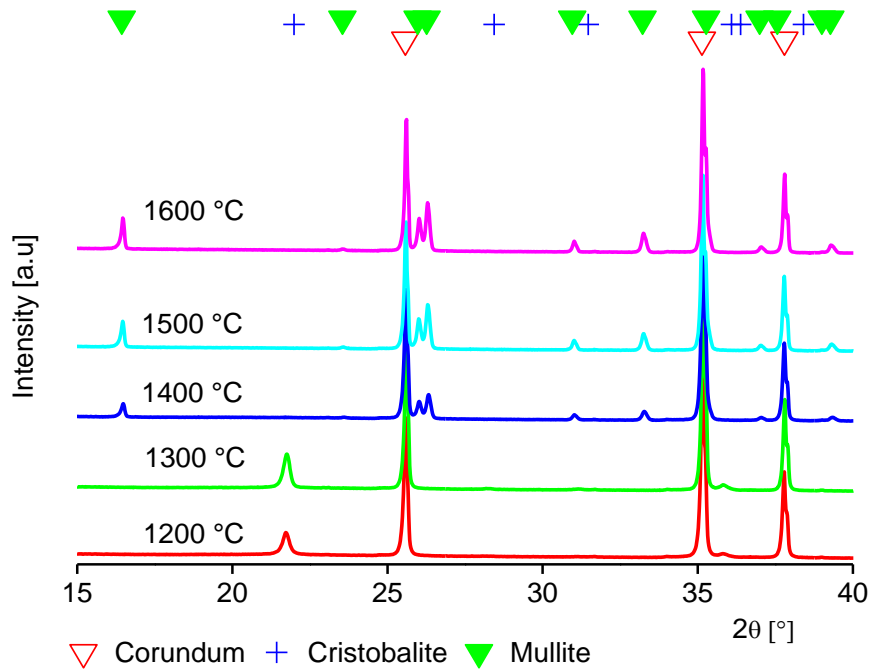


Figure 5.2: XRD patterns of the CS-23 samples sintered at different temperatures with holding times of 12 h

Appendix 14

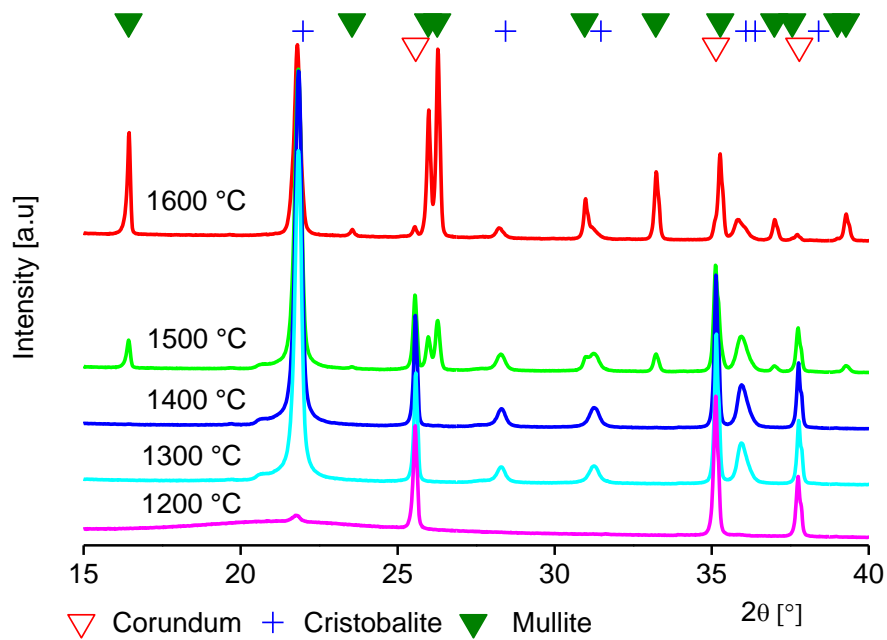


Figure 5.3: XRD patterns of the TEOS-77 samples sintered at different temperatures with holding times of 12 h

Appendix 15: XRD phase composition of samples sintered in a temperature range from 1200 °C to 1600 °C with a holding times of 3 h

Temp. [°C]	TEOS-23			CS-23		
	cristobalite [mol.-%]	corundum [mol.-%]	mullite [mol.-%]	cristobalite [mol.-%]	corundum [mol.-%]	mullite [mol.-%]
1200	1	99	-	2	98	-
1300	3	98	-	3	97	-
1400	8	92	-	10	89	1
1500	5	75	20	4	68	28
1600	3	72	25	2	64	34

Appendix 16: Density and porosity of samples sintered at different temperatures with holding a time of 12 h

Temp. [°C]	Properties	TEOS-23	CS-23	TEOS-77	CS-40
1200	ρ_B [g cm ⁻³]	1.72±0.02	2.61±0.02	1.33±0.02	2.81±0.02
	ρ_S [g cm ⁻³]	3.51±0.02	3.84±0.02	2.98±0.02	3.19±0.02
	porosity [%]	51	32	56	12
1400	ρ_B [g cm ⁻³]	2.12±0.02	2.74±0.02	1.51±0.02	2.84±0.02
	ρ_S [g cm ⁻³]	3.64±0.02	3.75±0.02	2.99±0.02	3.16±0.02
	porosity [%]	42	27	50	10
1600	ρ_B [g cm ⁻³]	2.31±0.02	2.96±0.02	1.71±0.02	2.89±0.02
	ρ_S [g cm ⁻³]	3.52±0.02	3.76±0.02	2.93±0.02	3.15±0.02
	porosity [%]	34	21	42	8
	porosity [%] (μ -CT)	26	11	-	-

where ρ_B = bulk density, ρ_S = skeletal density

Appendix 17: Chemical composition found in EDX spot analysis (see Figure 4.17 (i)), TEOS-23 sample sintered at 1200 °C for 3 h

Position	Mol.-%		
	O	Al	Si
11	20	78	0.2
12	20	30	15

Appendix 18: Chemical composition found in EDX spot analysis (see Figure 4.17 (iii)), TEOS-23 sample sintered at 1600 °C for 3 h

Position	Mol.-%		
	Al	Si	O
a	31	0	63
b	27	1	66
c	3	14	47
d	8	15	58
e	2	15	52

Appendix 19: Chemical composition found in EDX spot analysis (see Figure 4.17 (ii)), TEOS-23 sample sintered at 1600 °C for 3 h

Position	Mol.-%		
	Al	Si	O
a	35	0.1	63
b	10	15	69
c	32	0.9	58
d	22	6	58

Appendix 20: Chemical composition found in EDX spot analysis (see Figure 4.17 (iv)), TEOS-23 sample sintered at 1600 °C for 12 h

Position	Mol.-%		
	Al	Si	O
i	46	0.1	53
j	41	1	50
m	31	7	51
n	2	0.3	27

Appendix 21: Chemical composition found in EDX spot analysis (see Figure 4.18 (i)), TEOS-77 sample sintered at 1600 °C for 12 h

Position	Mol.-%		
	Al	Si	O
a	33	9	58
b	33	8	59
c	3	29	68
d	30	8	61
e	4	27	68
f	29	8	65

Appendix 22: Chemical composition found in EDX spot analysis (see Figure 4.19 (i)), CS-40 sample sintered at 1600 °C for 12 h

Position	Mol.-%		
	Al	Si	O
a	34	8	58
b	34	8	59
c	34	8	58
d	30	7	63
e	30	6	64
f	31	7	62
g	42	0.3	57

Appendix 23: Chemical composition found in EDX spot analysis (see Figure 4.19 (iii)), CS-23 sample sintered at 1600 °C for 12 h

Position	Mol.-%		
	Al	Si	O
a	37	1	62
b	42	0.2	57
c	42	0.2	56
d	17	14	65
f	5	21	62

Appendix 24: Vickers hardness, sample sintered for 5 K min⁻¹ with holding times 12 h

Sample	TEOS-23 [GPa]	CS-23 [GPa]
1200	4±2	6±2
1400	6±2	10±2
1600	5±2	9±2

Appendix 25: Flexural strength vs firing temperature for CS-23 and TEOS-23 samples after a sintering time of 3 h and 12 h

Temp. [°C]	TEOS-23, 3 h	TEOS-23, 12 h	CS-23, 3 h	CS-23, 12 h
1200	12±5 MPa	20±5 MPa	40±14 MPa	50±14 MPa
1400	19±5 MPa	36±5 MPa	112±14 MPa	102±14 MPa
1600	28±5 MPa	32±5 MPa	101±14 MPa	93±14 MPa

Appendix 26: Calculation of the failure probability for TEOS-23 and CS-23 samples sintered at 1600 °C (12 h holding times)

i	TEOS-23, σ_i, [MPa]	Failure probability	CS-23, σ_i, [MPa]	Failure probability
1	26	0.11	72	0.08
2	28	0.23	81	0.19
3	28	0.25	86	0.27
4	29	0.27	88	0.33
5	30	0.32	89	0.35
6	31	0.39	91	0.40
7	32	0.49	93	0.46
8	33	0.64	99	0.62
9	39	0.96	101	0.68
10	41	0.99	127	0.99

where σ_i :flexural strength

Appendix 27: Thermal properties of TEOS-23 ceramic samples after sintering at 1600 °C for 12 h

Temperature [°C]	Thermal conductivity [W m⁻¹ K⁻¹]	Heat capacity [J g⁻¹ K⁻¹]	Thermal diffusivity [mm² s⁻¹]
25	1.16	0.77	1.26
100	0.99	0.87	0.96
200	0.84	0.97	0.72
300	0.78	1.04	0.63
400	0.75	1.09	0.57
500	0.72	1.12	0.54
600	0.69	1.14	0.51
700	0.67	1.15	0.49
800	0.66	1.17	0.48
900	0.65	1.19	0.47
1000	0.65	1.22	0.45

Appendix 28: Thermal properties of CS-23 ceramic sample after sintering at 1600 °C for 12 h

Temperature [°C]	Thermal conductivity [W m⁻¹ K⁻¹]	Heat capacity [J g⁻¹ K⁻¹]	Thermal diffusivity [mm² s⁻¹]
25	5.56	0.75	2.54
100	5.03	0.90	1.92
200	4.51	1.01	1.55
300	4.15	1.07	1.34
400	3.92	1.12	1.21
500	3.75	1.15	1.12
600	3.58	1.18	1.05
700	3.50	1.20	1.02
800	3.35	1.22	0.95
900	3.33	1.23	0.94
1000	3.21	1.24	0.91

Curriculum vitae

Name Valetine Kubong Atanga
Date of birth/place 27.08.1976, Alatening/Cameroon

Work experience

01/2010 - till present PHD student at the Chair of Inorganic Non-metallic Materials (Prof. M. Scheffler), Otto von Guericke University Magdeburg, Germany

06/2008 - 12/2009 PHD student at the Chair of Light Weight Ceramics (Prof. M. Scheffler), Brandenburg Technical University, Cottbus, Germany

09/2002 - 06/2004 Assistant Chemistry teacher, Amasia Bilingual School Complex, Cameroon

Education

09/2004 - 03/2008 Faculty of Environmental Sciences and Process Engineering. Department of Environmental and Resource Management. Brandenburg Technical University Cottbus, Germany
Academic degree: Master of Science (M.Sc.)

09/1998 - 07/2002 Faculty of Science, Department of Chemistry, University of Buea, South West Province, Cameroon. Academic degree: Bachelor of Science (B.Sc.)

09/1994 - 07/1997 Longla Comprehensive College Bamenda (L.C.C Mankon), Cameroon
General Certificate of Education Advance Level (G.C.E A/L)

09/1988 - 07/1994 Longla Comprehensive College Bamenda (L.C.C Mankon), Cameroon
General Certificate of Education Ordinary Level (G.C.E O/L)